

DISCLAIMER

This report was prepared as an account of work sponsored by an agency of the United States Government. Neither the United States Government nor any agency thereof, nor any of their employees, makes any warranty, expressed or implied, or assumes any legal liability or responsibility for the accuracy, completeness, or usefulness of any information, apparatus, product, or process disclosed, or represents that its use would not infringe privately owned rights. Reference herein to any specific commercial product, process, or service by trade name, trademark, manufacturer, or otherwise does not necessarily constitute or imply its endorsement, recommendation, or favoring by the United States Government or any agency thereof. The views and opinions of authors expressed herein do not necessarily state or reflect those of the United States Government.

ABSTRACT

This report describes work performed during the second year of the project, “Using Chemicals to Optimize Conformance Control in Fractured Reservoirs.” This research project has three objectives. The first objective is to develop a capability to predict and optimize the ability of gels to reduce permeability to water more than that to oil or gas. The second objective is to develop procedures for optimizing blocking agent placement in wells where hydraulic fractures cause channeling problems. The third objective is to develop procedures to optimize blocking agent placement in naturally fractured reservoirs.

During extrusion experiments with Cr(III)-acetate-HPAM gels, we found that to maximize gel penetration along fractures, the highest practical injection rate should be used. However, in wide fractures, gel dehydration may be desirable to form rigid gels that are less likely to washout after placement. In these applications, reduced injection rates may be appropriate. In single, wide fractures where short distances of penetration are needed, the gel volume required increases roughly with the distance of penetration. In single fractures with narrow to moderate widths, the required gel volume increases roughly with the distance of penetration raised to the 1.5 power. For conditions examined to date, the pressure gradient during gel extrusion was insensitive to injection rate (for fractures of a given width). With an understanding of the mechanism for gel extrusion and dehydration in fractures, we ultimately hope to predict conditions, compositions, and volumes that provide the optimum gel placement in fractured reservoirs.

Analyses were performed to compare our laboratory gel extrusion results with those from a field application that involved a gel treatment to reduce water production from a near-horizontal production well that was intersected by a fault. Our analyses revealed three important points. First, simple calculations can give at least a rudimentary indication of the width of the fracture that causes the excess water production. For the case of vertical fractures or faults that cross horizontal production wells, these calculations can also give an idea of how far the gel should penetrate to provide a beneficial effect. Using laboratory data coupled with field data collected before, during, and after gel injection, the calculations can also give an indication of how far the gel has actually penetrated into the fracture. Our analyses point out areas where additional laboratory work is needed to aid in the design of field applications—especially at higher temperatures for gels over a range of concentrations. Finally, our analyses reveal critical measurements that should be made during field applications—especially, accurate flowing and static downhole pressures.

Imaging experiments are in progress using high-resolution computed microtomography (CMT) at Brookhaven National Laboratory to understand why some water-based gels reduce permeability to water more than that to oil. Results from our first set of experiments revealed that the method provides outstanding resolution of rock, water, and oil on a micrometer scale. In water-wet Berea sandstone, the water film around trapped residual oil drops was clearly visible. Also, CMT results indicated that a water-based Cr(III)-acetate-HPAM gel increased the residual oil saturation in larger pores during water injection, thus decreasing permeability to water much more than that to oil.

TABLE OF CONTENTS

DISCLAIMER.....	ii
ABSTRACT.....	iii
TABLE OF FIGURES.....	vi
LIST OF TABLES.....	viii
ACKNOWLEDGMENTS.....	ix
EXECUTIVE SUMMARY.....	x
Gel Propagation through Fractures.....	x
Field Application of Gel Propagation Results.....	xi
Disproportionate Permeability Reduction.....	xi
1. INTRODUCTION.....	1
Objectives.....	1
Report Content.....	1
2. GEL PROPAGATION THROUGH FRACTURES.....	2
Previous Experimental Work.....	2
Effect of Injection Rate.....	5
Effect of Fracture Height.....	8
Model 2.....	11
Effect of Fracture Width.....	16
$u_l = 0.05 t^{-0.55}$ versus $u_l = \int 0.05 t^{-0.55} dL / L$	22
Effect of Fracture Length.....	26
Summary of Leakoff Data.....	32
Predictions in Long Fractures.....	34
Physical Basis for Eq. 3.....	36
$1/(w_f)^2$ Dependence for Pressure Gradients.....	40
Relation Between Shear-Thinning and $1/(w_f)^2$ Dependence for Pressure Gradients.....	41
Upper Limit for the Rate of Gel Injection.....	43
Injection at Low Rates.....	44
Effect of Polymer Molecular Weight.....	46
Dual Fracture Floods.....	50
Effect of Temperature—Preliminary Study.....	53
Conclusions.....	55
Future Work.....	55
3. FIELD APPLICATION OF GEL PROPAGATION RESULTS.....	56
Field Example.....	56
Fracture Characterization before the Treatment.....	57
How Far into the Fault Should the Gel Penetrate?.....	58
Was the Injected Material a Gel or a Gelant?.....	58
How Far Did the Gel Penetrate?.....	59
How Effectively Did Gel Seal the Fault?.....	60
Conclusions.....	61
4. DISPROPORTIONATE PERMEABILITY REDUCTION.....	62
Imaging Experiments Using Synchrotron X-Ray Microtomography.....	62
Image analysis Using 3DMA Software.....	71
Modeling Disproportionate Permeability Reduction Using a Capillary-Bundle Model.....	73
Summary.....	80

NOMENCLATURE	81
REFERENCES	83
APPENDIX A: Technology Transfer	85
Presentations	85
Internet Postings on the Project and Software to Download.....	86
Papers and Publications.....	86

TABLE OF FIGURES

Fig. 1—Pressure gradients required for gel extrusion through open fractures.	3
Fig. 2—Degree of gel dehydration versus fracture width.....	3
Fig. 3—Cross-sectional view of core outlet. Separate collection of fracture and matrix effluent. .5	
Fig. 4—Gel propagation in 48×1.5×0.04-in. fractures. Model 1: $k_{gel}=0.00011+1.0(C/C_o)^{-3}$	7
Fig. 5—Fraction of flow produced from the porous rock during gel injection.....	7
Fig. 6—Schematic of experiment in 12×12×0.04-in. fracture.	8
Fig. 7—Fraction of flow produced from matrix during injection into 12x12x0.04-in. fractures....	9
Fig. 8—Wormhole pattern after dyed gel injection at 129 ft/d.	10
Fig. 9—Wormhole pattern after dyed gel injection at 413 ft/d.	11
Fig. 10—Average leakoff rate from seven experiments at different velocities.	12
Fig. 11—Gel propagation in 48×1.5×0.04-in. fractures. Model 2: $u_l = 0.05 t^{-0.55}$	13
Fig. 12—Gel breakthrough versus injection flux for 48x1.5x0.04-in. fractures.....	14
Fig. 13—Peak matrix flow versus injection flux for 48x1.5x0.04-in. fractures.	14
Fig. 14—Final matrix flow versus injection flux for 48x1.5x0.04-in. fractures.....	15
Fig. 15—Final gel concentrations in 48x1.5x0.04-in. fractures.....	15
Fig. 16—Average leakoff rates in 0.08-in.-wide fractures.	17
Fig. 17—Gel breakthrough versus injection flux for 48x1.5x0.08-in. fractures.....	17
Fig. 18—Peak matrix flow versus injection flux for 48x1.5x0.08-in. fractures.	18
Fig. 19—Final matrix flow versus injection flux for 48x1.5x0.08-in. fractures.....	18
Fig. 20—Final gel concentrations in 48x1.5x0.08-in. fractures.....	19
Fig. 21—Average leakoff rates for different fracture widths.....	19
Fig. 22—Gel breakthrough versus fracture width for 48x1.5-in. fractures.	20
Fig. 23—Peak matrix flow versus fracture width for 48x1.5-in. fractures.....	21
Fig. 24—Final matrix flow versus fracture width for 48x1.5-in. fractures.....	21
Fig. 25—Final gel concentrations in 48x1.5-in. fractures.	22
Fig. 26—Comparison of leakoff rates calculated by two methods (at identical times).....	23
Fig. 27—Comparison of gel propagation rates calculated by two methods.	24
Fig. 28—Leakoff rates predicted from Model 3 versus Model 2	24
Fig. 29—Gel propagation in 48×1.5×0.04-in. fractures. Model 3: $u_l = \int 0.05 t^{-0.55} dL / L$	25
Fig. 30—Gel breakthrough versus injection flux for 48x1.5x0.04-in. fractures.....	25
Fig. 31—Final gel concentrations in 48x1.5x0.04-in. fractures.....	26
Fig. 32—Leakoff rates in 16-ft-long fractures.	27
Fig. 33—Leakoff rates in second 16-ft-long fracture: Total versus each section.	28
Fig. 34—Gel propagation at 2,070 ft/d in the first 16-ft-long fracture.....	28
Fig. 35—Gel propagation at 10,330 ft/d in the second 16-ft-long fracture.	29
Fig. 36—Gel composition along a 16-ft-long fracture after gel placement at 2,070 ft/d.	29
Fig. 37—Gel composition along a 16-ft-long fracture after gel placement at 10,330 ft/d.	30
Fig. 38—Leakoff rates in a 32-ft-long fracture: Total versus each section.	31
Fig. 39—Gel propagation at 5,170 ft/d in a 32-ft-long fracture.....	32
Fig. 40—Gel composition along a 32-ft-long fracture after gel placement at 5,170 ft/d.	32
Fig. 41—Summary of leakoff data.	33
Fig. 42—Model predictions in long two-wing fractures at different rates.	34
Fig. 43—Model predictions in long two-wing fractures with different widths.	35
Fig. 44—Predictions of fraction of fracture area contacted by fresh versus concentrated gel.....	38

Fig. 45—Gel concentration versus time	38
Fig. 46—Leakoff rate from concentrated gel.....	39
Fig. 47—Leakoff from fresh gel relative to concentrated gel.....	39
Fig. 48— $1/(w_f)^2$ relations that contain the data scatter.....	40
Fig. 49—Comparison of $1/(w_f)^2$ versus $1/w_f$ relations.....	41
Fig. 50—Gel resistance factors versus superficial velocity.....	42
Fig. 51—Upper rate limit for gel injection.....	43
Fig. 52—Pressure drops during the first experiment at 41.3 ft/d.....	44
Fig. 53—Pressure drops during the second experiment at 41.3 ft/d.....	45
Fig. 54—Water leakoff from gel during the second experiment at 41.3 ft/d.....	45
Fig. 55—Gel composition in fracture after gel placement at 41.3 ft/d.....	46
Fig. 56—Average leakoff rates using gel with high-Mw HPAM.....	48
Fig. 57—Gel composition in fracture after gel placement at 2,070 ft/d.....	49
Fig. 58—Gel composition in fracture after gel placement at 33,100 ft/d.....	49
Fig. 59—Gel compositions in fractures after the first dual fracture flood.....	51
Fig. 60—Leakoff rates from the narrow fracture during the first dual fracture flood.....	51
Fig. 61—Gel compositions in fractures after the second dual fracture flood.....	52
Fig. 62—Leakoff rates from the narrow fracture during the second dual fracture flood.....	53
Fig. 63—Gel propagation at 4,130 ft/d in a 48x1.5x0.04-in. fracture at 60°C.....	54
Fig. 64—Leakoff during gel injection at 4,130 ft/d in a 48x1.5x0.04-in. fracture at 60°C.....	54
Fig. 65—Effect of gel propagation on fault plugging	59
Fig. 66—Schematic of X-ray Synchrotron Microtomography apparatus.....	63
Fig. 67—Berea core plug used in X-ray Synchrotron Microtomography	63
Fig. 68—Dimensions of the cropped image block.....	64
Fig. 69—3-D image of the Berea core plug with an image resolution of 10 μm	65
Fig. 70—Dimensions of image slab.....	66
Fig. 71—X-Y plane view of image slab (slices 460-469) at $S_w=1.0$	66
Fig. 72—X-Y plane view of image slab (slices 460-469) at S_{wr}	67
Fig. 73—X-Y plane view of image slab (slices 460-469) at S_{or}	67
Fig. 74—X-Y plane view of image slab (slices 460-469) at S_{or} after gelant injection.....	68
Fig. 75—X-Y plane view of image slab (slices 460-469) after F_{rro} measurement	69
Fig. 76—X-Y plane view of image slab (slices 460-469) after F_{rrw} measurement.....	69
Fig. 77—Distributions of nodal pore volume and the corresponding effective pore radii	71
Fig. 78—Distributions of throat surface area and the corresponding effective throat radii	72
Fig. 79—Relationship between effective pore radii and effective throat radii.....	72
Fig. 80—Skeletonized image of the Berea sandstone	73
Fig. 81—Fluid distributions at S_{wr} in pores with a uniform size distribution.....	74
Fig. 82—Fluid distributions at S_{or} in pores with a uniform size distribution.....	74
Fig. 83—Fluid distributions after gelant injection in pores with a uniform size distribution.....	75
Fig. 84—Fluid distribution after F_{rro} measurements in pores of a uniform size distribution.....	76
Fig. 85—Fluid distribution after F_{rrw} measurements in pores of a uniform size distribution.....	77
Fig. 86—Fluid distribution for example calculations.....	78

LIST OF TABLES

Table 1—Effect of injection rate on gel propagation in 0.04-in.-wide fractures	6
Table 2—Measurements versus predictions.....	13
Table 3—Effect of injection rate on gel propagation in 0.8-in.-wide fractures	16
Table 4—Effect of fracture width on gel propagation.....	20
Table 5—Effect of gel composition for Percol 338 gels in 48×1.5×0.04-in. fractures	47
Table 6—Production well data before and after gel treatment.....	56
Table 7—Compositions, pressures, and volumes of injected gels	57
Table 8—Summary of residual resistance factors: Water-based gel.....	64
Table 9—Summary of residual resistance factors: Oil-based gel	70

ACKNOWLEDGMENTS

Financial support for this work is gratefully acknowledged from the United States Department of Energy (National Petroleum Technology Office), BP-Amoco, Chevron, Chinese Petroleum Corporation, Chinese National Petroleum Corporation, Halliburton Energy Services, Marathon, Norsk Hydro (Saga), Shell, and Texaco. I greatly appreciate the efforts of those individuals who contributed to this project. Richard Schrader performed most of the experimental work described in Chapter 2, with considerable help from Kathryn Wavrik. The New Mexico Bureau of Mines Chemistry Laboratory determined the chromium concentrations. Dr. Robert Lane (Northstar Technologies International, Houston) participated in the analysis of field data described in Chapter 3. Dr. Jenn-Tai Liang played the major role in conducting the work described in Chapter 4. John Hagstrom helped perform the experiments described in Chapter 4. We also thank Dr. John Dunsmuir of ExxonMobil Research and Engineering Company for his invaluable aid during the X-ray microtomography studies. We also thank the National Synchrotron Light Source (NSLS) at Brookhaven National Laboratory for allowing us to use their facility. Image analyses were performed using a software package called 3DMA by Dr. Brent Lindquist (Department of Applied Mathematics and Statistics of State University of New York at Stony Brook). We appreciate the help of Dr. Ken Sorbie (Heriot-Watt University, Edinburgh), who conceived the mechanistic description of the disproportionate permeability reduction that is described in Chapter 4. We especially appreciate the thorough review of this manuscript by Julie Ruff.

EXECUTIVE SUMMARY

This report describes work performed during the second year of the project, “Using Chemicals to Optimize Conformance Control In Fractured Reservoirs.” This research project has three objectives. The first objective is to develop a capability to predict and optimize the ability of gels to reduce permeability to water more than that to oil or gas. The second objective is to develop procedures for optimizing blocking agent placement in wells where hydraulic fractures cause channeling problems. The third objective is to develop procedures to optimize blocking agent placement in naturally fractured reservoirs. This research project consists of three tasks, each of which addresses one of the above objectives. Our work is directed at both injection wells and production wells and at vertical, horizontal, and highly deviated wells.

Gel Propagation through Fractures

Many conformance control treatments rely on the ability of gels to extrude through fractures during the placement process. Chapter 2 describes an experimental investigation of the mechanism for propagation of a Cr(III)-acetate-HPAM gel through fractures. During gel extrusion, water leaks off from the gel, and the gel concentrates to become immobile in the vicinity where dehydration occurred. The driving force for gel dehydration (and water leakoff) is the pressure difference between the fracture and the adjacent porous rock. Fresh gel (i.e., mobile gel, with the original composition) must wormhole through the concentrated gel in order to advance the gel front. With time at a given position along the fracture, the average gel concentration increases and the fracture area contacted by wormholes (i.e., mobile gel) decreases. Even so, water leakoff from the concentrated, immobile gel is generally small compared with leakoff from the mobile gel.

A minimum pressure gradient is required to extrude a given gel through a fracture. Once this minimum pressure gradient is exceeded, the pressure gradient during gel extrusion is insensitive to the flow rate. The pressure gradient required for gel extrusion varies inversely with the square of fracture width. In contrast, a force balance during gel extrusion predicts that the pressure gradient should vary linearly with fracture width. Although we have not definitively identified the origin of this behavior, we have demonstrated that it is directly linked to the extremely strong apparent shear-thinning behavior during extrusion.

With an understanding of the mechanism for gel extrusion and dehydration in fractures, we ultimately hope to predict conditions, compositions, and volumes that provide the optimum gel placement in fractured reservoirs. In our work with 24-hr-old Cr(III)-acetate-HPAM gels at 41°C, a number of observations have been made to aid us in achieving our goal. First, dehydration reduces the rate of gel propagation through fractures. This dehydration has been quantified for a significant range of conditions. For fracture widths from 0.02 to 0.16 inches, fracture lengths from 0.5 to 32 ft, fracture heights from 1.5 to 12 inches, and injection fluxes from 129 to 66,200 ft/d, the average rate of gel dehydration and leakoff (u_l , in ft/d or ft³/ft²/d) was described reasonably well using: $u_l = 0.05 t^{-0.55}$, where t is time in days. This relation was also found to apply to Cr(III)-acetate-HPAM gels that contained 0.5% Alcoflood 935 or 0.5% Percol 338 HPAM. (Percol 338 has roughly twice the molecular weight of Alcoflood 935. The two polymers have the same degree of hydrolysis.)

For conditions examined to date, the pressure gradient during gel extrusion was insensitive to injection rate (for fractures of a given width). To maximize gel penetration along fractures, the highest practical injection rate should be used. However, in wide fractures, gel dehydration may be desirable to form rigid gels that are less likely to washout after placement. In these applications, reduced injection rates may be appropriate. In single, wide fractures where short distances of penetration are needed, the gel volume required increases roughly with the distance of penetration. In single fractures with narrow to moderate widths, the required gel volume increases roughly with the distance of penetration raised to the 1.5 power.

Field Application of Gel Propagation Results

In Chapter 3, we examine the relation between field and laboratory results. The field application (provided by R.H. Lane) involved a gel treatment to reduce water production from a near-horizontal production well that was intersected by a fault. Our analyses revealed three important points. First, simple calculations can give at least a rudimentary indication of the width of the fracture that causes the excess water production. For the case of vertical fractures or faults that cross horizontal production wells, these calculations can also give an idea of how far the gel should penetrate to provide a beneficial effect. Using laboratory data coupled with field data collected before, during, and after gel injection, the calculations can also give an indication of how far the gel has actually penetrated into the fracture.

Second, this analysis points out areas where additional laboratory work is needed to aid in the design of field applications. In particular, a need exists for determination of gel extrusion properties at higher temperatures—at least up to 100°C. Also, a need exists to determine gel extrusion properties for gels over a range of concentrations, e.g., for polymer concentrations from 0.3% to 1.5%.

Third, our analysis reveals critical measurements that should be made during field applications. In particular, accurate flowing and static downhole pressures should be made at least before and after the gel treatment is applied. Some very useful insights can be gained if downhole pressures are measured during gel injection.

Disproportionate Permeability Reduction

The purpose of water shutoff treatments in production wells is to reduce water production without damaging the oil productivity. Many polymers and gels can reduce the permeability to water more than that to oil or gas. This property is critical to the success of water shutoff treatments in production wells if hydrocarbon-productive zones cannot be protected during placement. However, the mechanism of this disproportionate permeability reduction is not fully understood.

Imaging experiments are in progress using high-resolution computed microtomography (CMT) at Brookhaven National Laboratory to understand why gels reduce permeability to water more than that to oil. The method provides outstanding resolution of rock, water, and oil on a micrometer scale. In water-wet Berea sandstone, the water film around trapped residual oil drops was clearly visible. In our first set of experiments, CMT results indicated that gels increased the residual oil saturation in larger pores during water injection, thus decreasing permeability to water much more than that to oil.

In our second set of experiments, we used CMT to visualize why an oil-based gel reduce the permeability to oil more than that to water. The objective is to compare the results with those from our first set of experiments using a water-based gel to improve our understanding of why the disproportionate permeability reduction occurs. We are now analyzing the data generated during the imaging experiments.

Based on the results from our imaging experiments, we developed a simple capillary-bundle model to predict disproportionate permeability reduction. Using a simple example, we demonstrated that the model could qualitatively predict the disproportionate permeability reduction. However, due to the simplified assumptions made in developing the model, more work is needed using data from our image analyses to improve this model.

1. INTRODUCTION

In the United States, more than 20 billion barrels of water are produced each year during oilfield operations. Today, the cost of water disposal is typically between \$0.25 and \$0.50 per bbl for pipeline transport and \$1.50 per bbl for trucked water. Therefore, a tremendous economic incentive exists to reduce water production if that can be accomplished without significantly sacrificing hydrocarbon production. For each 1% reduction in water production, the cost savings to the oil industry could be between \$50,000,000 and \$100,000,000 per year. Reduced water production would result directly in improved oil recovery (IOR) efficiency in addition to reduced oil-production costs. A substantial positive environmental impact could also be realized if significant reductions are achieved in the amount of water produced during oilfield operations.

In an earlier project, we identified fractures (either naturally or artificially induced) as a major factor that causes excess water production and reduced oil recovery efficiency, especially during waterfloods and IOR projects. We found fractures to be a channeling and water production problem that has a high potential for successful treatment by gels and certain other chemical blocking agents. We also determined that the ability of blocking agents to reduce permeability to water much more than that to oil is critical to the success of these blocking treatments in production wells if zones are not isolated during placement of the blocking agent.

This report describes work performed during the second year of the project, “Using Chemicals to Optimize Conformance Control in Fractured Reservoirs.” Results from the first year were documented in Ref. 1.

Objectives

This research project has three objectives. The first objective is to develop a capability to predict and optimize the ability of gels to reduce permeability to water more than that to oil or gas. The second objective is to develop procedures for optimizing blocking agent placement in wells where hydraulic fractures cause channeling problems. The third objective is to develop procedures to optimize blocking agent placement in naturally fractured reservoirs. This research project consists of three tasks, each of which addresses one of the above objectives. Our work is directed at both injection wells and production wells and at vertical, horizontal, and highly deviated wells.

Report Content

This report describes work performed during the second year of the project. In Chapter 2, we report experimental results from studies of gel properties in fractures. In Chapter 3, we examine the relation between laboratory results and a field application where a gel treatment reduced water production from a near-horizontal production well that was intersected by a fault. Finally, in Chapter 4, we investigate the mechanism responsible for gels reducing the permeability to water more than that to oil.

2. GEL PROPAGATION THROUGH FRACTURES

Gel treatments were often applied to improve conformance and reduce water or gas channeling in reservoirs.²⁻⁶ During conventional gel treatments, a fluid gelant solution typically flowed into a reservoir through porous rock and fractures. After placement, chemical reactions (i.e., gelation) caused an immobile gel to form. However, for the most successful treatments in naturally fractured reservoirs, the time required to inject large volumes (e.g., 10,000 to 37,000 bbls) of gel was typically greater than the gelation time by a factor of 100.³⁻⁵ Thus, in these applications, formed gels extruded through fractures during most of the placement process. A need exists to determine how much gel should be injected in a given application and where that gel distributes in a fractured reservoir. These parameters depend critically on the properties of gels in fractures. Therefore, we have a research program to determine these properties and to characterize gel placement in fractured systems.

In this chapter, we first review previous work concerning gel propagation and dehydration during extrusion through fractures. This review includes a summary of a model (Model 1) that was proposed to describe gel propagation. This chapter also examines the effects of injection rate, fracture width, height, and length, and polymer molecular weight on gel propagation and dehydration. This information is used to develop an improved model of gel propagation (Model 2), which is applied to predict gel placement in long fractures. Finally, several mechanistic features of gel propagation are examined. With an understanding of the mechanism for gel propagation, we hope to increase confidence in predictions for field applications.

Previous Experimental Work

Previous work demonstrated that gels do not flow through porous rock after gelation.⁷ This behavior is advantageous since the gel is confined to the fractures—it does not enter or damage the porous rock (except at the rock face). Thus, after gel placement, water, oil, or gas can flow unimpeded through the rock, but flow through the fracture is reduced substantially. However, extrusion of gels through fractures introduces new issues that are not of concern during placement of fluid gelant solutions. First, the pressure gradients during gel extrusion are greater than those for flow of gelants. For a Cr(III)-acetate-HPAM gel, the pressure gradient required for extrusion varied inversely with the square of fracture width (Fig. 1 and Eq. 1):

$$dp/dl = 0.02 / (w_f)^2, \dots\dots\dots(1)$$

where dp/dl has units of psi/ft and w_f has units of in. In previous work,⁷⁻¹² we demonstrated that a minimum pressure gradient was required to extrude a given gel through a fracture. Once this minimum pressure gradient was exceeded, the pressure gradient during gel extrusion was insensitive to the flow rate.^{7,9,12}

A second concern is that gels can concentrate (dehydrate) during extrusion through fractures.^{1,10} Depending on fracture width (see Fig. 2), this dehydration effect can significantly retard gel propagation (e.g., by factors up to 50). Figs. 1 and 2 apply to a one-day-old Cr(III)-acetate-HPAM gel at 41°C. This same gel was used for most of the experiments described in this report. Specifically, our experiments used an aqueous gel that contained 0.5% Ciba Alcoflood 935 HPAM (molecular weight $\approx 5 \times 10^6$ daltons; degree of hydrolysis 5% to 10%), 0.0417% Cr(III)

acetate, 1% NaCl, and 0.1% CaCl₂ at pH=6. All experiments were performed at 41°C (105°F). The gelant formulations were aged at 41°C for 24 hours (5 times the gelation time) before injection into a fractured core. We designate this gel as our standard Cr(III)-acetate-HPAM gel.

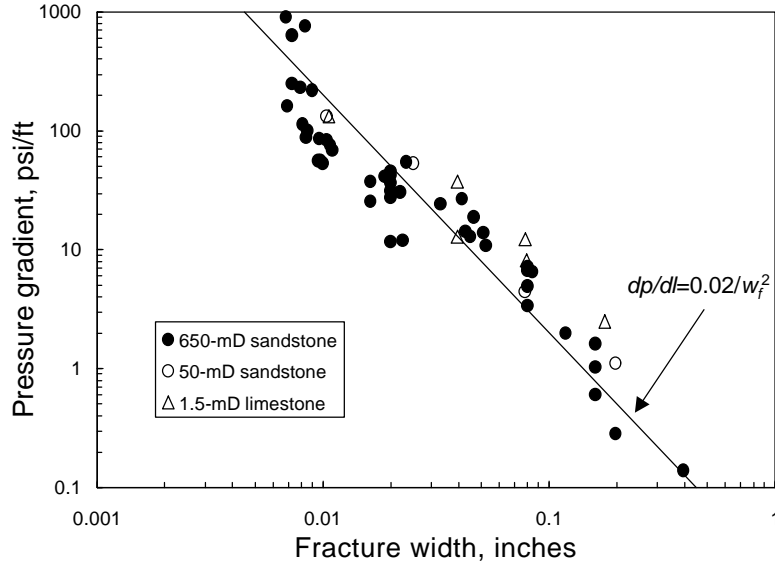


Fig. 1—Pressure gradients required for gel extrusion through open fractures.

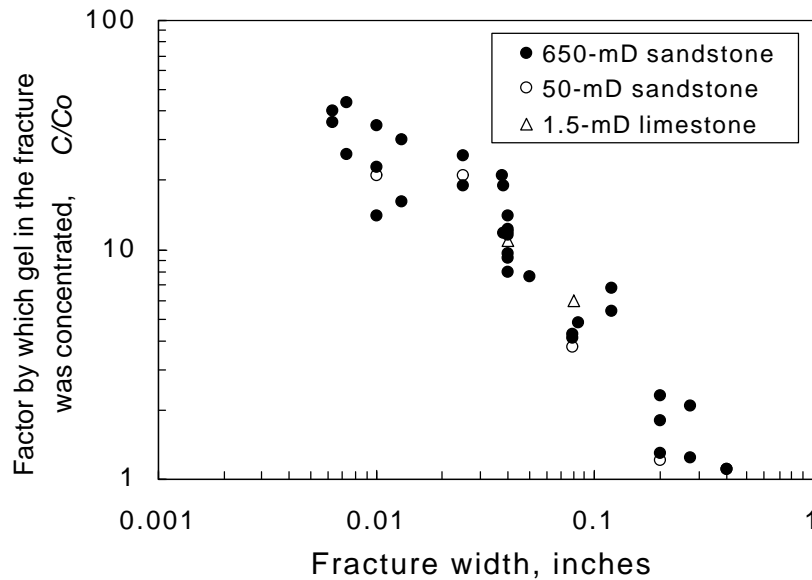


Fig. 2—Degree of gel dehydration versus fracture width (from Ref. 10).

In earlier work,¹⁰ we showed that when large volumes of gel were extruded through a fracture, progressive plugging (i.e., continuously increasing pressure gradients) was not observed. Effluent from the fracture had the same appearance and a similar composition as those for the

injected gel, even though a concentrated, immobile gel formed in the fracture. The concentrated gel formed when water leaked off from the gel along the length of the fracture. The driving force for gel dehydration (and water leakoff) was the pressure difference between the fracture and the adjacent porous rock. During gel extrusion through a fracture of a given width, the pressure gradients along the fracture and the dehydration factors were comparable for fractures in 650-mD sandstone as in 50-mD sandstone and 1.5-mD limestone (Figs. 1 and 2).

Model 1. Previously,¹⁰ a simple model (Model 1) was developed that correctly matched the behavior during gel propagation and dehydration in a fracture with dimensions of 48x1.5x0.04 in. using an injection rate of 12.2 in.³/hr (200 cm³/hr). This model assumed the following:

1. Gel in the fracture existed in one of two forms: (a) flowing gel that had the same composition and properties as the originally injected gel, and (b) concentrated immobile gel. The flowing gel wormholed through the concentrated immobile gel.
2. The Darcy equation applied for water flow through gel, with a gel permeability to water, k_{gel} . The driving force for gel dehydration (and water leakoff) was the pressure difference between the fracture and the adjacent porous rock. The average distance that water traveled through the gel to reach the matrix was half the fracture width, $w_f/2$.
3. For a given length of fracture, the rate of water entering the fracture (in the form of gel) minus the rate of water leaving the fracture (again tied up as gel) equaled the rate of water leakoff through the fracture faces. (Water mass balance.)
4. No crosslinked polymer entered the porous rock. Any gel that concentrated (dehydrated) immediately became immobile. (Crosslinked polymer mass balance.)
5. At any point in the fracture, the gel permeability to water, k_{gel} , was related to the average gel composition by Eq. 2.

$$k_{gel} = 0.00011 + 1.0 (C/C_o)^{-3} \dots\dots\dots (2)$$

In Eq. 2, k_{gel} had units of mD when the gel composition, C/C_o , was expressed relative to the composition of our standard Cr(III)-acetate-HPAM gel (i.e., 0.5% HPAM, 0.0417% Cr(III)-acetate). Originally, Eq. 2 was simply an empirical three-parameter fit that allowed the model to correctly quantify the rate of gel propagation through a 48x1.5x0.04-in. fracture. Since the original development of this model, we found independent support¹ for two of the three parameters in Eq. 2 (i.e., the 1.0-mD coefficient and the -3 exponent for the concentration term). However, no quantitative basis was found for the third parameter, 0.00011 mD.

As a qualitative explanation for Eq. 2, we speculated that the concentration-dependent term accounted for progressive dehydration of the concentrated immobile gel, while the constant term accounted for dehydration of flowing gel in the wormholes. At a given point in the fracture, the flowing gel was continually replenished, so it represented a source of gel with an unchanging concentration. Any flowing gel that dehydrated was added to the reservoir of concentrated gel. In contrast, the concentrated gel did not move and became ever more concentrated with time, so its average permeability to water continually decreased.

With an understanding of the mechanism for gel extrusion and dehydration in fractures, we ultimately hope to predict conditions, gel compositions, and gel volumes that provide the

optimum gel placement in fractured reservoirs. To realize this goal, our model requires further testing. Therefore, in this chapter, results are reported from extrusion experiments that used a range of fracture lengths, widths, and heights and a wide range of gel injection rates. Experiments were also performed using a gel prepared from a polymer with roughly twice the molecular weight of Alcoflood 935.

Effect of Injection Rate

Several experiments were performed to examine the effects of injection rate on gel extrusion and dehydration. Except for injection rate, these tests were identical to that described in Ref. 10. Specifically, in each test (at 41°C), we extruded 80 fracture volumes (226 in.³ or 3,700 cm³) of our standard 24-hr-old Cr(III)-acetate-HPAM gel through a 0.04-in.-wide fracture in a 4-ft-long, 650-mD Berea sandstone core. The cross-sectional area of the core was 2.25 in.² (1.5x1.5 in.), so the fracture height was 1.5 in. (3.8 cm). The total fracture volume was 2.84 in.³ (46.5 cm³), and the total pore volume of the system was about 25 in.³ (400 cm³). The core had five sections of equal length that were delineated by sets of fracture and matrix pressure taps. A fitting at the core outlet separated the effluent from the fracture and matrix (see Fig. 3). (Of course, a new core was used for each test.) To complement the 12.2 in.³/hr (200-cm³/hr) test that was described in Ref. 10, the three new tests were performed using gel injection rates of 30.5, 122, and 976 in.³/hr, respectively. Assuming that the total fracture volume was open to gel flow, the average velocities ranged from 413 to 33,100 ft/d for volumetric injection rates ranging from 12.2 to 976 in.³/hr (see Rows 2 and 3 of Table 1). For comparison, the velocity in a 100-ft-high, 0.04-in.-wide, two-wing fracture is 12,100 ft/d using an injection rate of 1 barrel per minute (BPM).

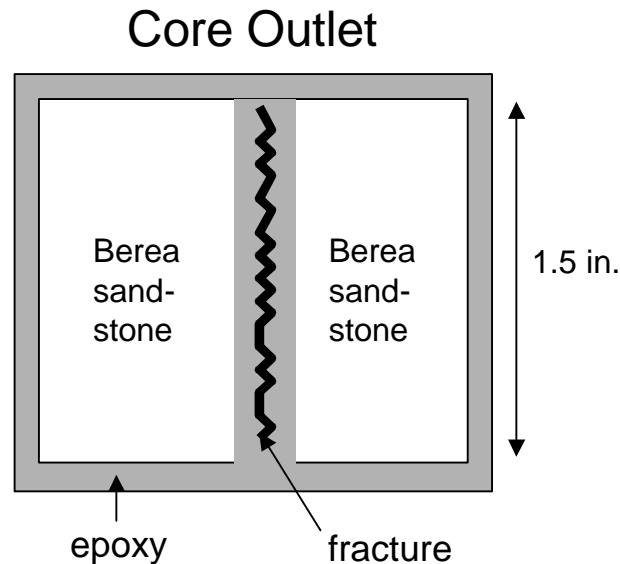


Fig. 3—Cross-sectional view of core outlet. Separate collection of fracture and matrix effluent.

Table 1 summarizes the results from these tests. Consistent with our earlier findings,^{7-9,12} pressure gradients along the fracture were relatively insensitive to injection rate. The average pressure gradients (Row 4 of Table 1) ranged from 18 to 40 psi/ft for estimated gel velocities ranging from 413 to 33,100 ft/d. We suspect the pressure-gradient variations in Table 1 were

caused by differences in the actual fracture width rather than by velocity differences. Mechanical degradation of the gel was fairly small. For gel produced from the fracture at the highest rate, the elastic modulus, G' , was about 20% less than that for the original gel. In all cases, the physical appearance of the gel remained unchanged by passage through the fracture.

Table 1—Effect of injection rate on gel propagation in 0.04-in.-wide fractures

1	Fracture dimensions (L_f - h_f - w_f)	48×1.5×0.04 in.			
2	Injection rate, in. ³ /hr	12.2	30.5	122	976
3	Estimated velocity in the fracture, ft/d	413	1,030	4,130	33,100
4	Average pressure gradient, psi/ft	28	29	40	18
5	Gel front arrival at core end, fracture volumes	15	6.0	4.0	1.7
6	Peak fraction of matrix flow, %	100	93	75	39
7	Final fraction of flow produced from matrix, %	35	26	16	5
8	Average C/C_o in fracture at end of experiment	27	17	11	4

Gel Front Propagation. The rate of gel front propagation increased significantly with increased injection rate (Row 5 of Table 1). For 413 ft/d, gel arrival at the end of a 4-ft-long fracture occurred after 15 fracture volumes of gel injection. Only 1.7 fracture volumes of gel were required when the velocity was 33,100 ft/d. Evidently, the gel had less time to dehydrate as the injection rate increased. With a lower level of gel dehydration (concentration), the gel propagated a greater distance for a given total volume of gel injection. This result has important consequences for field applications. It suggests that gels should be injected at the highest practical rate in order to maximize penetration into the fracture system.

During gel injection, pressures along the fracture indicated the rate of propagation of the gel front. For three of the experiments (413 ft/d, 1,030 and 4,130 ft/d, respectively), Fig. 4 shows the volume of gel required to reach a given distance along a 4-ft-long fracture. The solid symbols show the actual data points, while the open symbols with the dashed lines show predictions from our model (Model 1). As mentioned earlier, the three-parameters in Eq. 2 were originally fitted to describe the 413-ft/d experimental results. Thus, the match between the experiment and the predictions were expected for this case. However, for the other two velocities, the model predictions were typically 50% to 70% greater than the actual values. This finding indicates that our model needs refinement.

Gel Dehydration. For each experiment, a special outlet fitting (Fig. 3) segregated the effluent from the fracture and the rock. Fig. 5 plots the fraction of the effluent from the porous rock. Rows 6 and 7 of Table 1 summarize these results. In each case, the peak in flow from the porous rock was observed when gel arrived at the end of the fracture. Expressed as a fraction of the total flow, the magnitude of this peak decreased with increased injection rate—from 100% at 413 ft/d to 39% at 33,100 ft/d (Row 6 of Table 1). After gel breakthrough, the fraction of flow from the porous rock decreased in an exponential fashion. After 75-80 fracture volumes of gel injection, this fraction varied from 35% at 413 ft/d to 5% at 33,100 ft/d (Row 7 of Table 1). Of course, at any given time, the fraction of flow from the fracture plus that from the porous rock summed to unity. As a reminder, the total injection rate was constant during a given experiment.

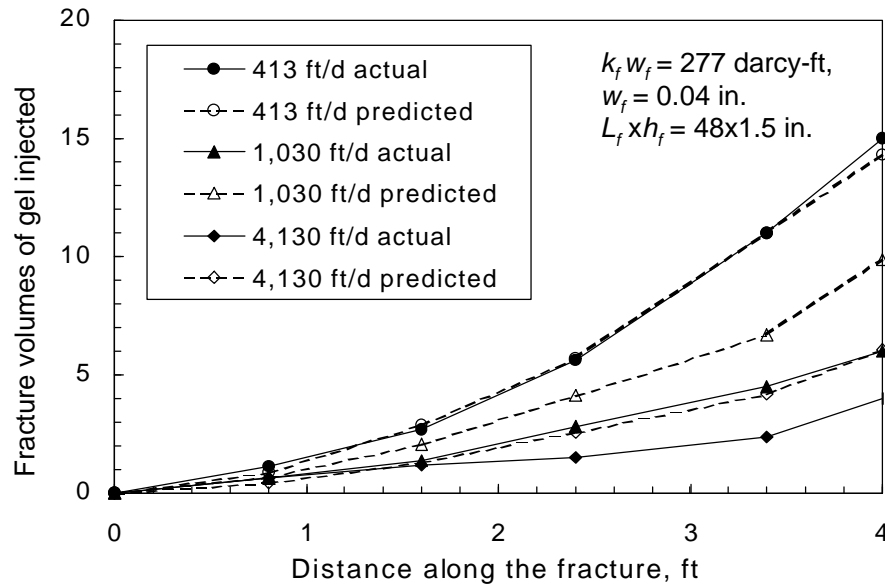


Fig. 4—Gel propagation in 48×1.5×0.04-in. fractures. Model 1: $k_{gel}=0.00011+1.0(C/C_o)^{-3}$.

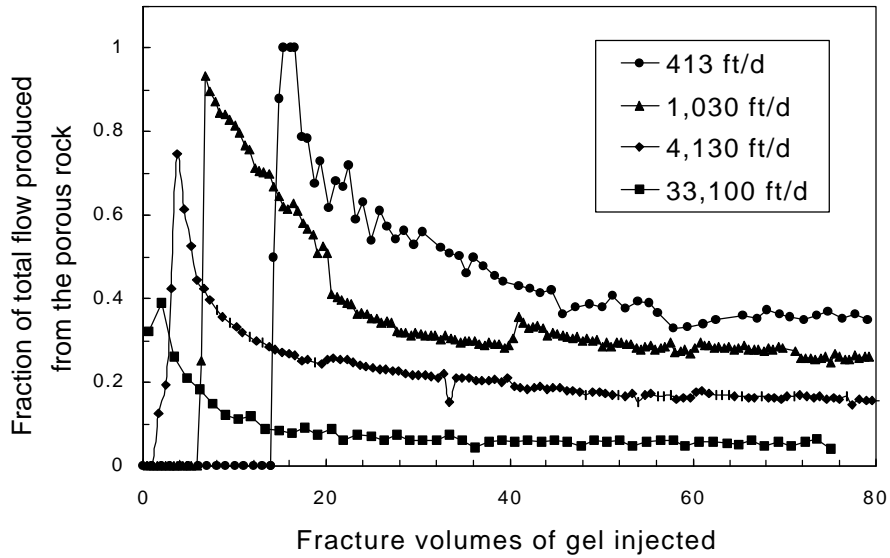


Fig. 5—Fraction of flow produced from the porous rock during gel injection.

The chromium and HPAM concentrations were determined for the effluent from both the fracture and the rock. In all cases, no significant chromium or HPAM were produced from the porous rock. Thus, only water (brine) flowed through the porous rock. Of course, the source of this flow was water that left the gel in the fracture—i.e., water from the gel dehydration process. Our findings confirm that crosslinked polymer (gel) does not enter or flow through porous rock.

Before gel arrival at the end of the fracture, virtually all fluid was produced from the fracture, and this fluid consisted of brine with no chromium or HPAM. This result was expected. Before gel injection, the calculated flow capacity of the fracture was 3,400 times greater than the flow capacity of the porous rock. After gel breakthrough, the composition and physical appearance of gel produced from the fracture were very similar to those of the injected gel.

After 80 fracture volumes of gel injection, the fracture was opened to reveal a rubbery gel that completely filled the fracture. These gels were analyzed for chromium and HPAM as a function of length along the fracture. Row 8 of Table 1 reports the average factor by which gel in the fracture was concentrated for each experiment. Expressed relative to the concentration of the injected gel (C/C_o), gel was concentrated by an average factor of 27 at 413 ft/d and by 4 at 33,100 ft/d. Of course, since fixed volumes of gel were injected, the duration of gel injection varied inversely with injection rate. Since gel in the fracture was under pressure for a shorter time in the faster experiments, the gel had less time to dehydrate. Consequently, the degree of dehydration decreased with increased injection rate. These results further support our conclusion that in field applications, gels should be injected at the highest practical rate to maximize penetration into the fracture system.

Effect of Fracture Height

To this point, our fracture heights were 1.5 in. (3.8 cm). Will gel extrusion and dehydration be affected by fracture height? To address this question, two experiments were performed with fracture heights of 12 in. Fig. 6 illustrates the fractured cores that were used. The cores were formed by stacking two 12×12×3-in. 650-mD Berea sandstone slabs. Spacers were used to separate the two slabs by 0.04 in. (0.1 cm) to form a 12×12×0.04-in. fracture. Because of the method of construction, the faces of the fracture were fairly smooth. (In contrast, the fractures described in the previous section were formed by cracking the core open using a special method that was described earlier.⁷ In our experience, the roughness of the fracture surfaces did not affect the performance during gel extrusion.) The total fracture volume was 5.67 in.³ (92.9 cm³) and the total pore volume of the system was 173 in.³ (2,831 cm³). The fractures were actually oriented horizontally, but for consistency, we identify the fracture “height” as the dimension perpendicular to the fracture length and width dimensions. A manifold distributed the injected gel evenly over the 12-in. height of the fracture. A similar manifold collected the effluent from the fracture. Two production ports allowed collection of effluent from each of the matrix slabs.

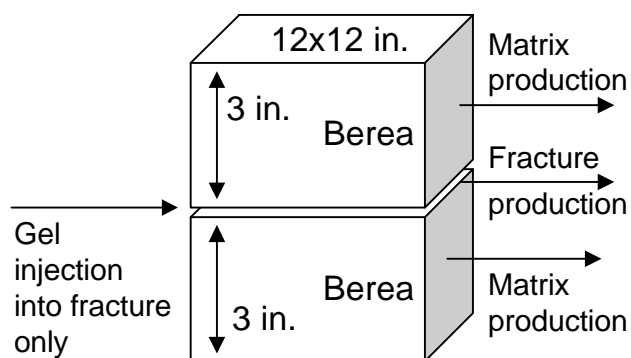


Fig. 6—Schematic of experiment in 12×12×0.04-in. fracture.

In the first experiment, 30 fracture volumes ($\sim 170 \text{ in.}^3$ or $2,800 \text{ cm}^3$) of our standard 24-hr-old Cr(III)-acetate-HPAM gel were injected at a fixed rate of $30.5 \text{ in.}^3/\text{hr}$ ($500 \text{ cm}^3/\text{hr}$). Considering the cross-sectional flow area of the fracture ($12 \times 0.04 \text{ in.}$), the injection flux or velocity was 129 ft/d (164 cm/hr). This value compares with a flux of $1,030 \text{ ft/d}$ when injecting gel at a rate of $30.5 \text{ in.}^3/\text{hr}$ into our earlier $48 \times 1.5 \times 0.04\text{-in.}$ fractured cores.

In the second experiment, 61 fracture volumes ($\sim 350 \text{ in.}^3$ or $5,700 \text{ cm}^3$) of gel were injected at a fixed rate of $98 \text{ in.}^3/\text{hr}$ ($1,600 \text{ cm}^3/\text{hr}$). The injection flux in this experiment was 413 ft/d . For both experiments, the pressure gradient during gel injection averaged 29 psi/ft . This value was very similar to those observed earlier during extrusion through fractures of the same width, but with heights of 1.5 in. (Table 1).

Consistent with our earlier results, no significant HPAM or chromium was produced from the matrix during these experiments. For the 129-ft/d and 413-ft/d experiments, gel breakthrough was noted after injecting 6 and 2.6 fracture volumes of gel, respectively. After gel breakthrough, the gel produced from the fractures was similar in composition to that for the injected gel. No significant fluid was produced from the matrix until gel breakthrough. At gel breakthrough, the fraction of fluid from the matrix jumped to 97% of the total flow for the 129-ft/d experiment and to 91% of the total flow for the 413-ft/d experiment (Fig. 7). With further gel injection in the 129-ft/d experiment, this fraction gradually declined to 55% of the total after injection of 30 fracture volumes. During the 413-ft/d experiment, the matrix fractional flow declined to 33% after 30 fracture volumes and 17% after 61 fracture volumes. (The data jumps in Fig. 7 occurred when switching injection pumps.)

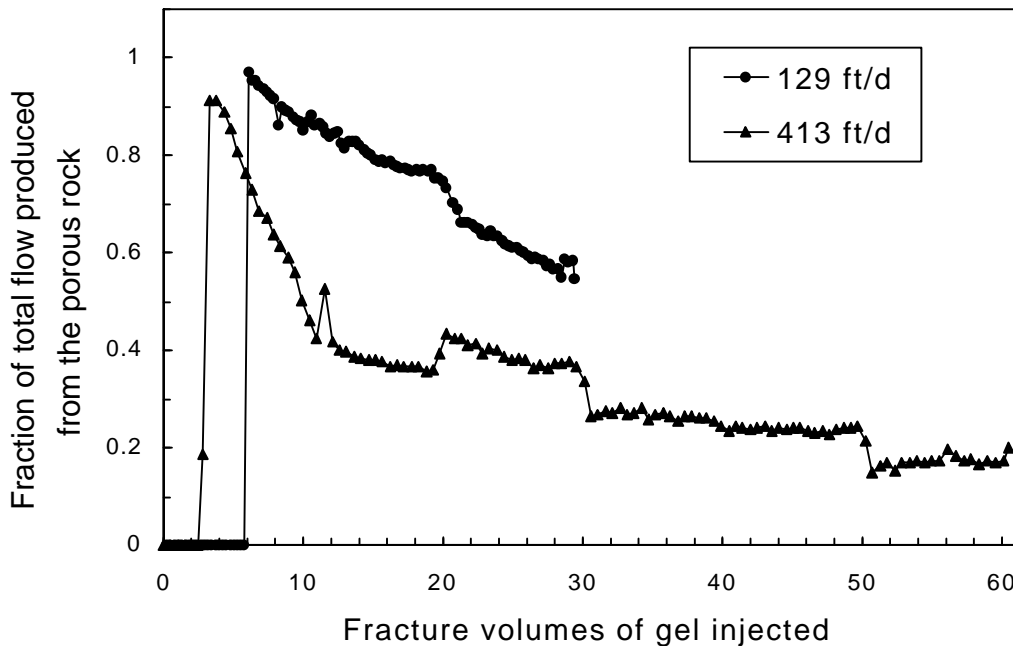


Fig. 7—Fraction of flow produced from matrix during injection into $12 \times 12 \times 0.04\text{-in.}$ fractures.

Wormholes. For both experiments, near the end of gel injection, dyed gel of the same composition was injected. For the 129- and 413-ft/d experiments, dye breakthrough occurred after 0.55 in.³ (9 cm³ or 0.097 fracture volumes) and 0.49 in.³ (8 cm³ or 0.086 fracture volumes), respectively. At the time of dyed-gel breakthrough, the average gel dehydration factors for newly injected gel were 55% and 17%, respectively (because these were the fractions of total flow produced as water from the end of the matrix). Thus, the estimated volumes of the pathways for the dyed gel were 0.25 in.³ [i.e., 0.55x(1-0.55)] or 0.044 fracture volumes (4 cm³) for the 129-ft/d experiment and 0.4 in.³ [i.e., 0.49x(1-0.17)] or 0.071 fracture volumes (6.6 cm³) for the 413-ft/d experiment. These results suggest that the injected gel formed small-volume wormholes through concentrated gel.

Consistent with this suggestion, wormhole pathways were noted (highlighted by the dye) through the concentrated gel in the fracture after opening the fracture at the end of the experiments (Fig. 8). The largest of these wormholes were 0.1 to 0.2 in. in height, compared to the total fracture height of 12 in. In the 129-ft/d experiment, one wormhole in the center of the pattern appeared dominant, while six other significant wormholes were present in various locations. A limited amount of branching was noted on these wormholes. In contrast, for the 413-ft/d experiment, highly branched wormhole patterns were found after dye injection. For both experiments, after removing the gel from the fractures, streaks of dyed rock were noted under the wormholes—revealing the leakoff pathways for water that dehydrated from the gel (Fig. 9).

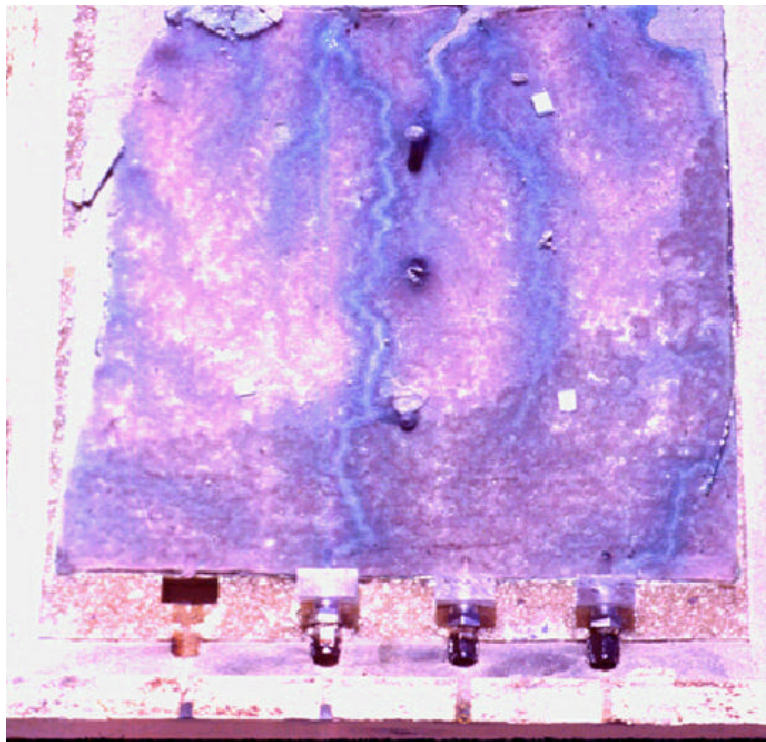


Fig. 8—Wormhole pattern after dyed gel injection at 129 ft/d. Total gel=30 fracture volumes. Concentrated gel in place. Flow was top to bottom.

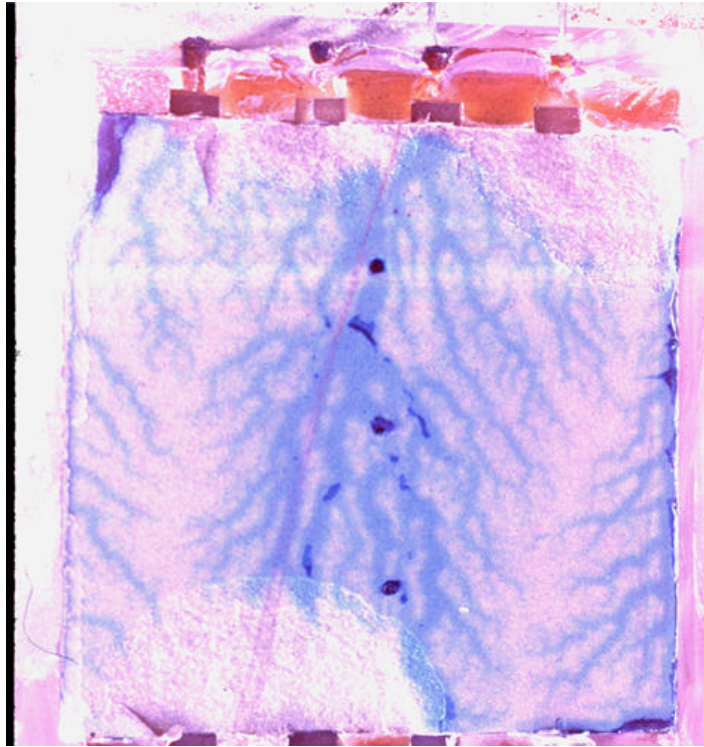


Fig. 9—Wormhole pattern after dyed gel injection at 413 ft/d.
 Total gel=61 fracture volumes. Concentrated gel removed to reveal dye leakoff pattern.
 Flow was top to bottom.

Dyed-gels were also injected near the end of the 1,030-ft/d and 4,130-ft/d experiments in the 48x1.5x0.04-in. fractures. Results indicated that the wormhole volumes were 0.10 and 0.14 fracture volumes, respectively. Since the wormhole volumes were 4% to 14% of the fracture volume, actual velocities for the flowing gel in the wormholes were 7 to 22 times faster than indicated by our flux values (i.e., calculated assuming that the entire fracture cross-section was open to flow).

Model 2

In view of the deficiencies of our first model, a second model was developed to account for our new results. Model 2 was inspired by a re-plot of the data in Figs. 5 and 7. Specifically, Fig. 10 plots the average leakoff rate (u_l , in $\text{ft}^3/\text{ft}^2/\text{d}$ or ft/d) versus time (t , in days) for the six experiments. Results are also included from a seventh experiment where the gel was forced through a 6x1.5x0.04-in. fracture at an average flux of 413 ft/d. (Details of this experiment can be found in Ref. 11.) At any given time, the average leakoff rate was simply the total flow rate from the matrix (at the end of the core) divided by the total fracture area in the core. For a given experiment, Fig. 10 included only the data after the peak in flow from the porous rock. Eq. 3 provided an excellent fit of the data.

$$u_l = 0.05 t^{-0.55} \dots\dots\dots(3)$$

Eq. 3 provides leakoff rates that are averaged over the length of the fracture (more specifically, over the gel-contacted length of the fracture). Eq. 4 relates the average leakoff rate to the local leakoff rate, u_i , at a given distance, L , along the fracture. This point will be discussed on page 22.

$$u_l = \int u_i dL / L \dots\dots\dots(4)$$

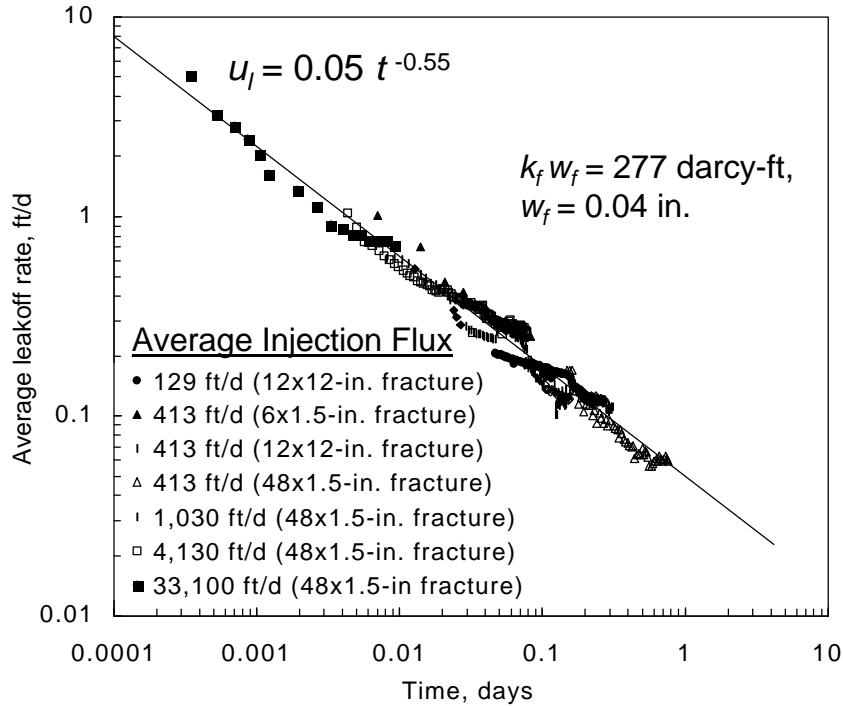


Fig. 10—Average leakoff rate from seven experiments at different velocities.

The rate of gel front propagation, dL/dt , in a 0.04-in.-wide fracture can be found from a mass balance (Eq. 5).

$$h_f w_f dL/dt = q_t - 2 h_f L u_l \dots\dots\dots(5)$$

In Eq. 5, h_f is fracture height, w_f is fracture width, and q_t is total volumetric injection rate. Combined with Eq. 3, Eq. 5 can easily be applied to predict rates of gel front propagation and gel dehydration. These equations form the basis for Model 2. In Fig. 11, the open symbols with the dashed lines show gel front positions predicted for three injection rates in 48x1.5x0.04-in. fractures. The solid symbols show the experimental values. A comparison of Figs. 4 and 11 reveals that except for the 413-ft/d case, the experimental data were matched better by Model 2 than Model 1. Model 2 provides an excellent match for the experimental leakoff rates (Fig. 10).

Additional comparisons of experimental results and predictions from Models 1 and 2 are included in Table 2. This table lists results from experiments in the 12x12x0.04-in. fractures as well as those in the 48x1.5x0.04-in. fractures. Regarding the rate of gel propagation, Model 2

gave more accurate predictions than Model 1 when rates were high. The success of Model 1 at 413 ft/d was not surprising since this model was based on a curve fit of low-rate data. Nevertheless, Model 2 provided reasonable predictions at low rates.

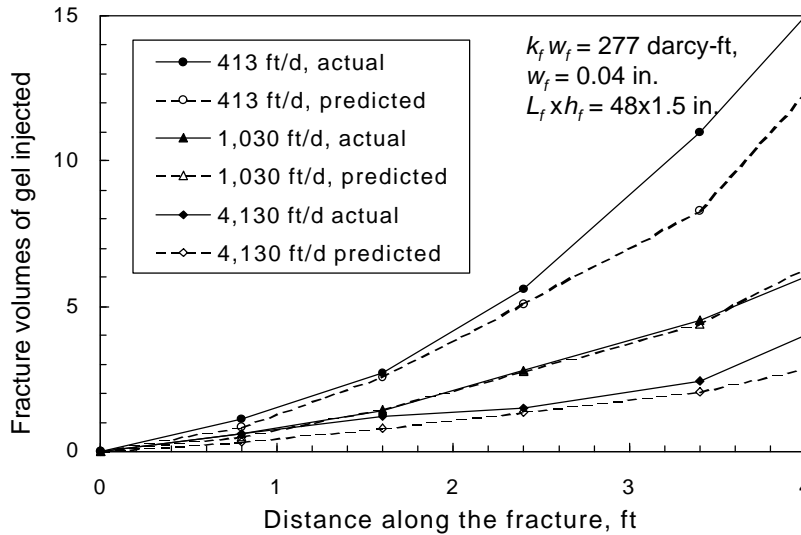


Fig. 11—Gel propagation in 48×1.5×0.04-in. fractures. Model 2: $u_l = 0.05 t^{-0.55}$.

Table 2—Measurements versus predictions:
Model 1 [$k_{gel}=0.00011+1.0(C/C_o)^{-3}$] and Model 2 [$u_l = 0.05 t^{-0.55}$]

Fracture dimensions ($L_f \times h_f \times w_f$)	48×1.5×0.04 in.				12×12×0.04 in.	
Injection rate, in. ³ /hr	12.2	30.5	122	976	30.5	98
Estimated velocity in the fracture, ft/d	413	1,030	4,130	33,100	129	413
Total fracture volumes of gel injected	80	80	80	80	30	61
GEL ARRIVAL AT CORE END, FRACTURE VOLUMES						
Actual	15	6.0	4.0	1.7	6.0	2.6
Predicted by Model 1	14.3	9.9	6.0	3.0	7.7	5.2
Predicted by Model 2	12.3	6.4	2.8	1.5	10.4	4.7
PEAK FRACTION OF MATRIX FLOW, %						
Actual	100	93	75	39	97	91
Predicted by Model 1	96	94	90	80	92	88
Predicted by Model 2	95	91	76	42	95	87
FRACTION OF FLOW PRODUCED FROM END OF MATRIX, %						
Actual	35	26	16	5	55	17
Predicted by Model 1	35	13	6	3	16	6
Predicted by Model 2	34	23	12	5	53	21
AVERAGE C/C_o IN FRACTURE AT END OF EXPERIMENT						
Actual	27	17	11	4	12	14
Predicted by Model 1	31	21	14	8	12	11
Predicted by Model 2	44	32	19	8	22	23

Figs. 12-15 illustrate the data in Table 2 in graphical form.

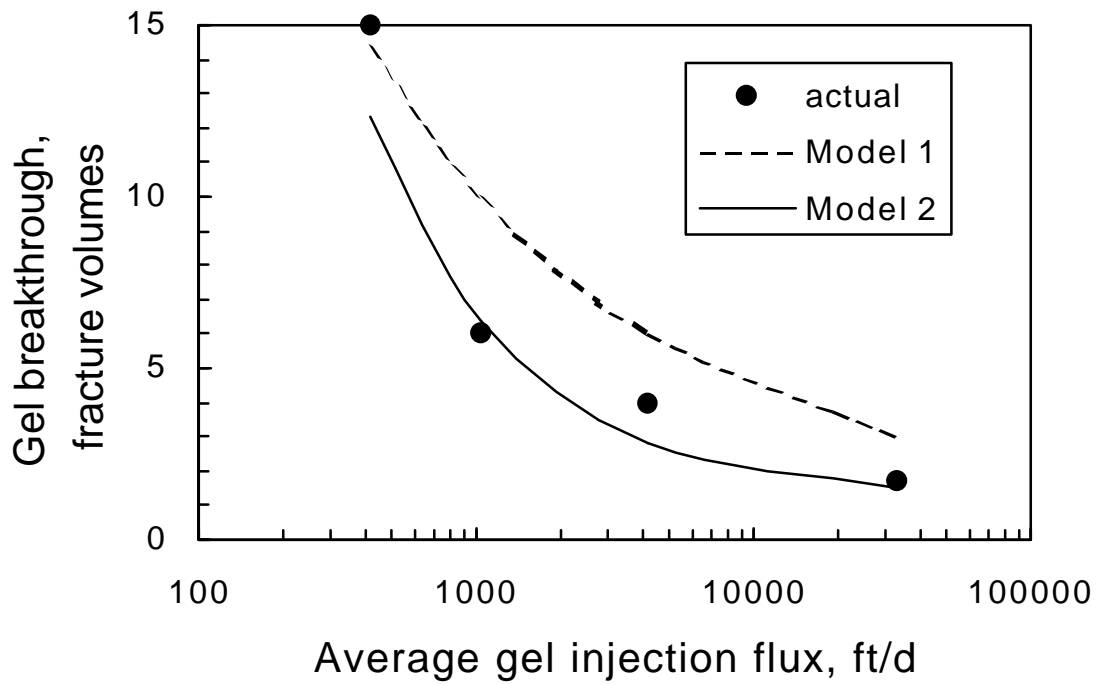


Fig. 12—Gel breakthrough versus injection flux for 48x1.5x0.04-in. fractures.

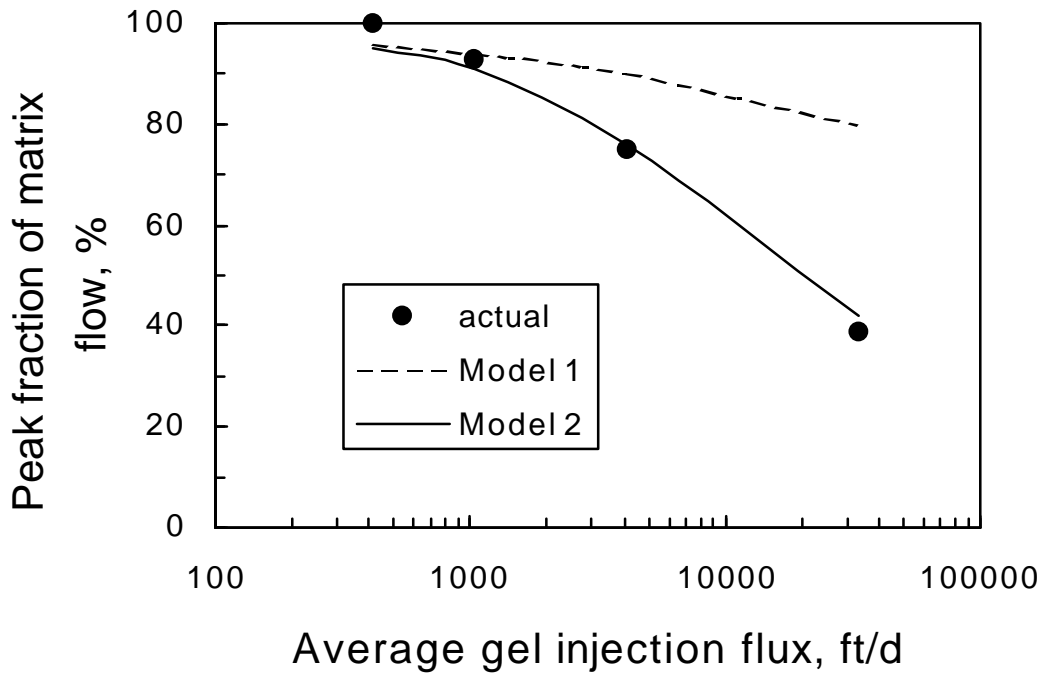


Fig. 13—Peak matrix flow versus injection flux for 48x1.5x0.04-in. fractures.

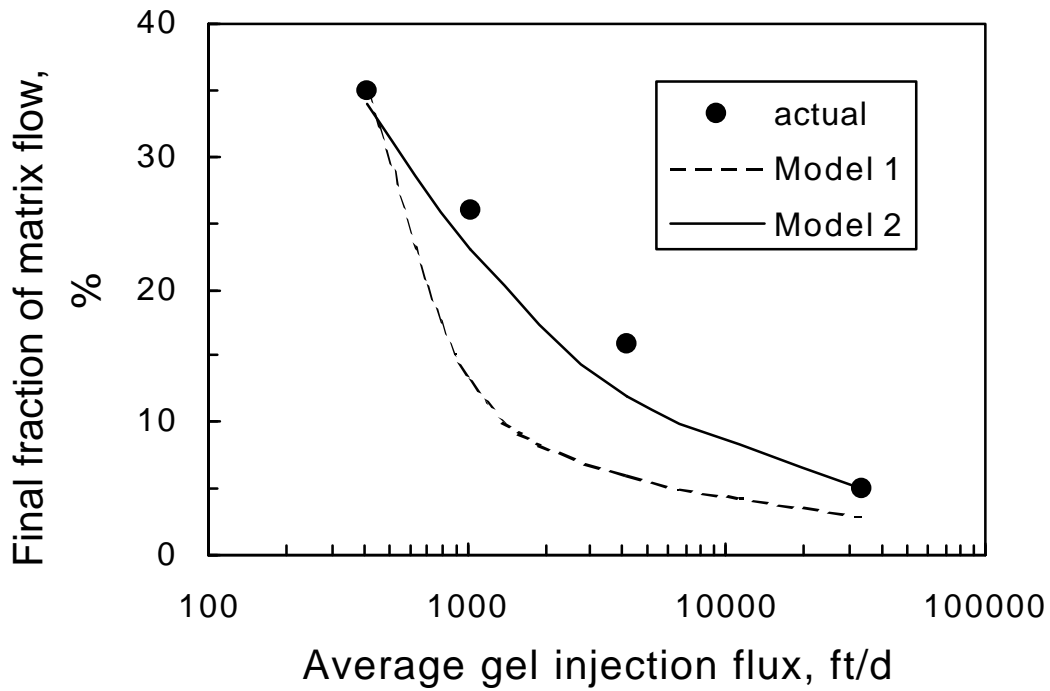


Fig. 14—Final matrix flow versus injection flux for 48x1.5x0.04-in. fractures.

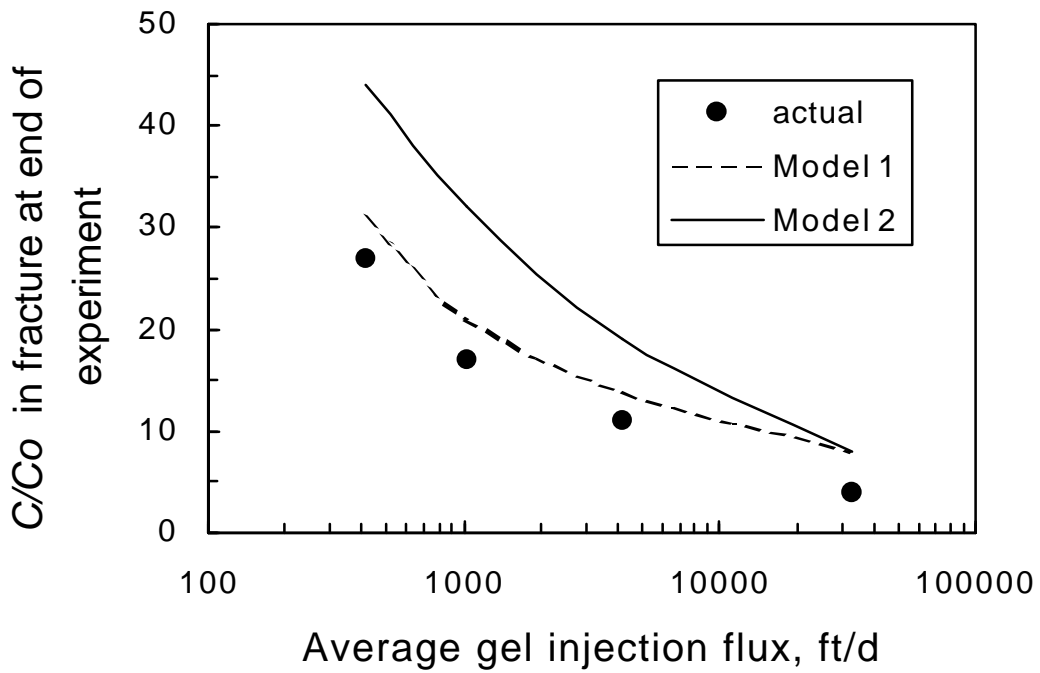


Fig. 15—Final gel concentrations in 48x1.5x0.04-in. fractures.

Regarding the leakoff data (i.e., flow from the matrix), Model 2 generally provided significantly better predictions than Model 1, although Model 1 performed acceptably at low rates in the 4-ft-long fractures. Model 1 consistently out-performed Model 2 in predicting the final average gel composition in the fractures. Except at the highest rate, concentration predictions from Model 2 were typically 60% to 90% too high. However, some experimental error was associated with our concentration determinations. Also, evidence exists that some free chromium and uncrosslinked HPAM leaked off into the porous rock during gel dehydration.¹¹ Furthermore, the flowing gel may be slightly more concentrated than the originally injected gel.^{1,11} These phenomena could decrease the mass of gel that accumulated at a given point in the fracture—thus, mitigating the concentration over-predictions for Model 2.

Effect of Fracture Width

48x1.5x0.08-in. Fractures. Model 2 worked well in describing the rate of gel propagation and the rate of water leakoff in fractures with widths of 0.04 in. Will the model require substantial modification if the fracture width is some other value? To answer this question, four experiments were performed in 48x1.5x0.08-in. fractures at four injection rates, ranging from 12.2 to 976 in.³/hr (200 to 16,000 cm³/hr). These experiments were identical to those described on page 5, except that the fracture widths were 0.08 in. instead of 0.04 in. Table 3 summarizes the results from the new experiments.

Table 3—Effect of injection rate on gel propagation in 0.8-in.-wide fractures

1	Fracture dimensions (L_f \times h_f \times w_f)	48x1.5x0.08 in.			
2	Injection rate, in. ³ /hr	12.2	30.5	122	976
3	Estimated velocity in the fracture, ft/d	207	517	2,070	16,500
4	Average pressure gradient, psi/ft	3.4	6.6	4.9	7.2
5	Gel front arrival at core end, fracture volumes	8.4	4.3	1.3	1.2
6	Peak fraction of matrix flow, %	100	98	90	27
7	Final fraction of flow produced from matrix, %	53	50	31	5
8	Average C/C_o in fracture at end of experiment	23.8	16.6	4.9	2.5

Qualitatively, the data in Table 3 followed the same trends noted for Table 1. Row 4 of Table 3 reveals that the pressure gradient for gel extrusion was insensitive to injection rate—averaging 5.5 psi/ft for fluxes ranging from 207 to 16,500 ft/d. This pressure gradient follows the trend shown in Fig. 1.

Fig. 16 shows leakoff results from the four experiments where our standard 24-hr-old Cr(III)-acetate-HPAM gel was extruded through the 0.08-in.-wide fractures. These experimental results generally followed the trend described by Eq. 3 (the solid line in Fig. 16); however, the fit was less impressive than that shown in Fig. 10. Additional work will be required to understand the deviations.

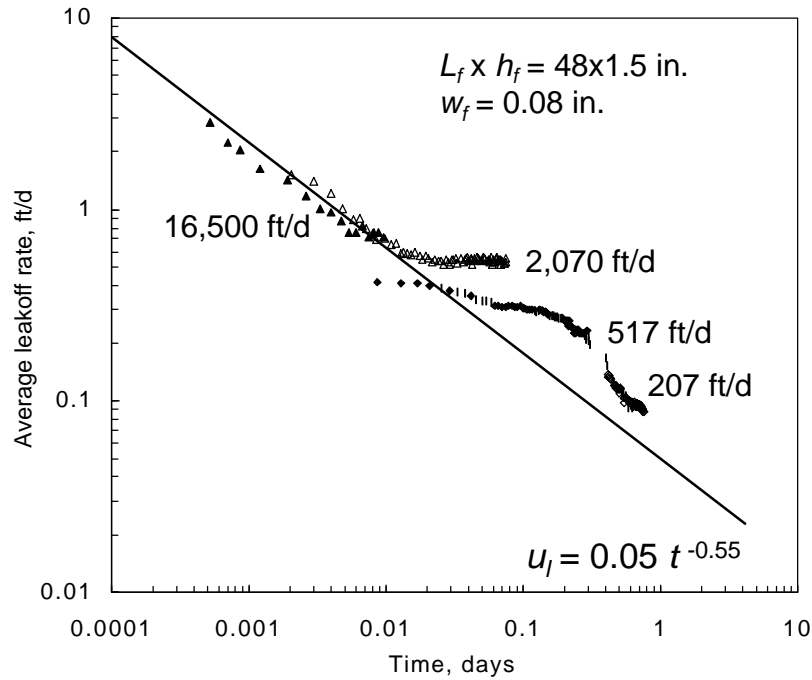


Fig. 16—Average leakoff rates in 0.08-in.-wide fractures.

Figs. 17-20 compare the results from Table 3 with predictions made using Model 1 and Model 2. Both models provide reasonable predictions of gel breakthrough for injection fluxes above 500 ft/d (Fig. 17). At 207 ft/d, both models under-predicted gel breakthrough, although Model 2 outperformed Model 1.

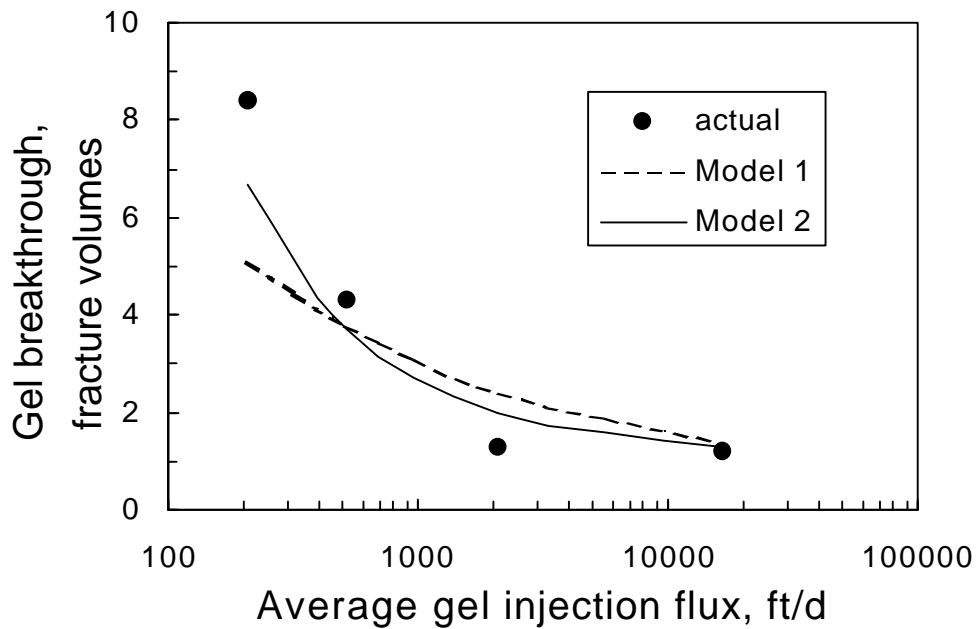


Fig. 17—Gel breakthrough versus injection flux for 48x1.5x0.08-in. fractures.

At 16,500 ft/d, Model 2 correctly predicted the peak and final fractions of water produced from the matrix (Figs. 18 and 19). However, the model under-predicted these values (by 9-27%) at lower fluxes. Predictions from Model 1 deviated significantly from the experimental values at all rates.

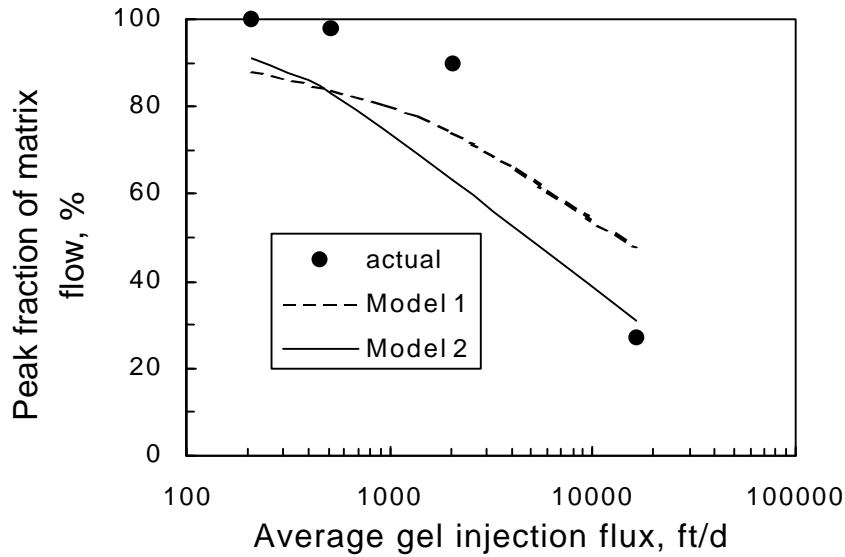


Fig. 18—Peak matrix flow versus injection flux for 48x1.5x0.08-in. fractures.

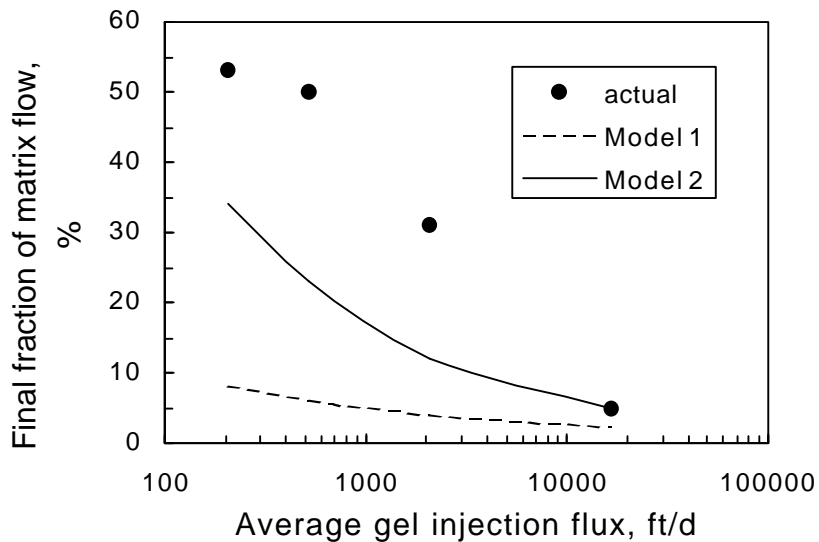


Fig. 19—Final matrix flow versus injection flux for 48x1.5x0.08-in. fractures.

The final average gel compositions in the fracture (relative to the composition of the original gel) are shown in Fig. 20. The experimental results were matched fairly well by Model 1 at the two highest rates and by Model 2 at the two lowest rates. More work is needed to understand the gel concentration behavior.

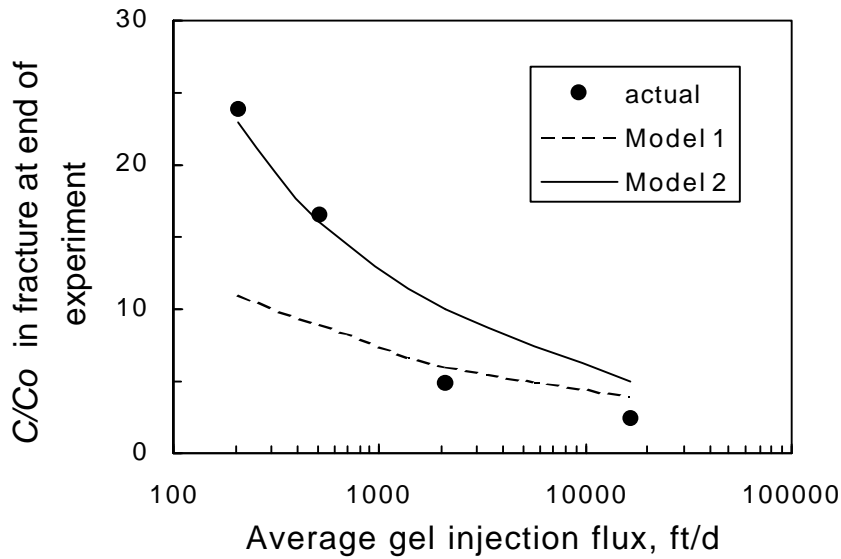


Fig. 20—Final gel concentrations in 48x1.5x0.08-in. fractures.

High Rates in 48x1.5-in. Fractures with Various Widths. We also performed high-rate (16,000 cm³/hr) extrusion experiments in fractures with widths of 0.02, 0.04, 0.08, and 0.16-in. (The length and height of the fractures were 48 in. and 1.5 in., respectively, and 3.7 liters of our standard 24-hr-old Cr(III)-acetate-HPAM gel were injected.) Fig. 21 shows that Eq. 3 described the leakoff results reasonably well. Eq. 3 provided the best match for fracture widths of 0.04 in. and 0.08 in. For 0.02-in.-wide and 0.16-in.-wide fractures, the leakoff data commonly fell below the predictions from Eq. 3.

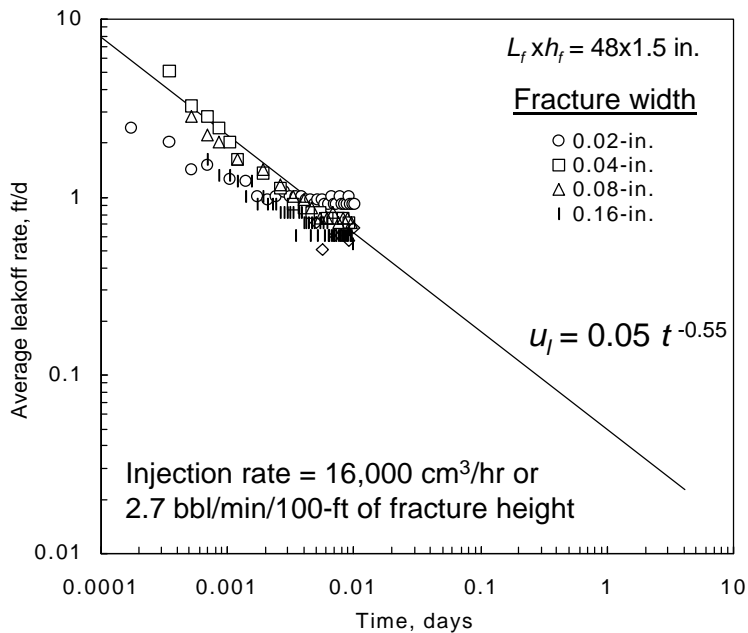


Fig. 21—Average leakoff rates for different fracture widths.

Many of the results from these experiments are summarized in Table 4. Row 4 in this table lists the average pressure gradients in the center 60% of the fracture (the middle three segments). As expected, these gradients decreased with increased fracture width. Row 5 in Table 4 lists the pressure gradients predicted from Eq. 1. The predictions are reasonably close to the actual values, considering the data scatter associated with the trend shown in Fig. 1.

Table 4—Effect of fracture width on gel propagation during injection of 3.7 liters of gel at 16,000 cm³/hr

1	Fracture dimensions ($L_f \times h_f$)	48×1.5 in.			
2	Fracture width, in.	0.02	0.04	0.08	0.16
3	Estimated velocity in the fracture, ft/d	66,100	33,100	16,500	8,260
4	Average pressure gradient, psi/ft	37	18	7.2	1.1
5	Predicted pressure gradient (Eq. 1), psi/ft	50	13	3.1	0.8
6	Gel front arrival at core end, fracture volumes	2.5	1.7	1.2	1.05
7	Peak fraction of matrix flow, %	26	39	27	21
8	Final fraction of flow produced from matrix, %	6.8	5	5	4.6
9	Average C/C_o in fracture at end of experiment	2.6	4	2.5	1.3

Figs. 22-25 compare the results from Table 4 with predictions made using Model 1 and Model 2. Both models provided rough estimates of gel breakthrough for fracture widths of 0.04 in. and above (Fig. 22). For the 0.02-in.-wide fracture, the prediction from Model 2 was much better than that from Model 1.

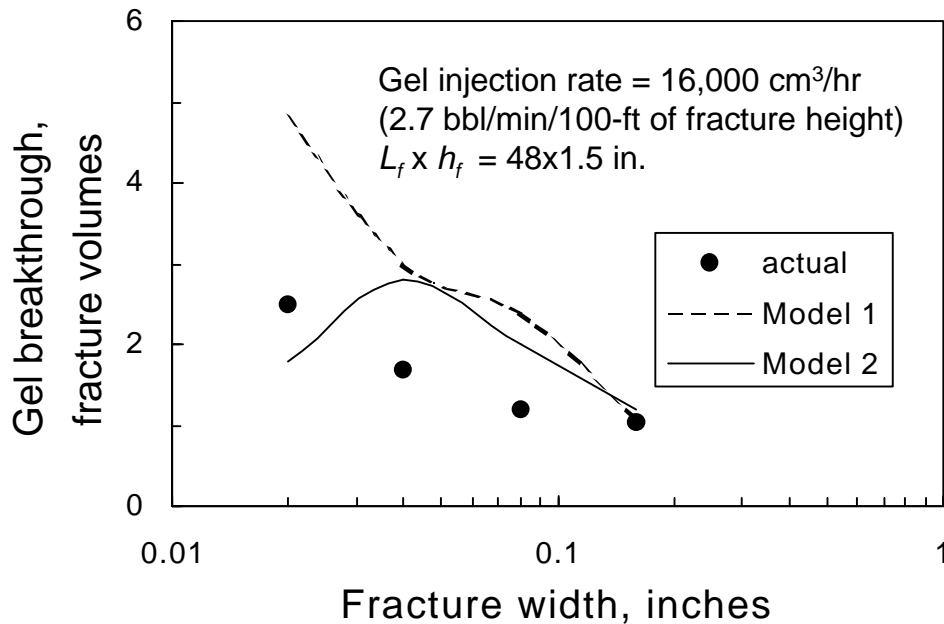


Fig. 22—Gel breakthrough versus fracture width for 48x1.5-in. fractures.

The peak and final fractions of flow from the matrix are shown in Figs. 23 and 24. Predictions from Model 2 matched the experimental values very well for the three widest fractures. For the narrowest fracture, Model 2 significantly over-predicted the peak fraction of matrix flow and under-predicted the final fraction of matrix flow. Predictions from Model 1 were poor in most cases.

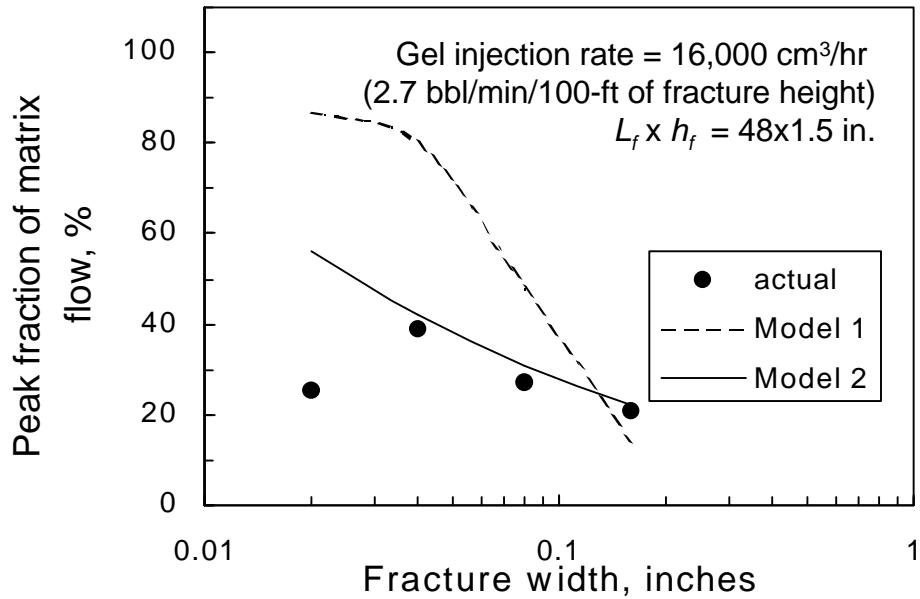


Fig. 23—Peak matrix flow versus fracture width for 48x1.5-in. fractures.

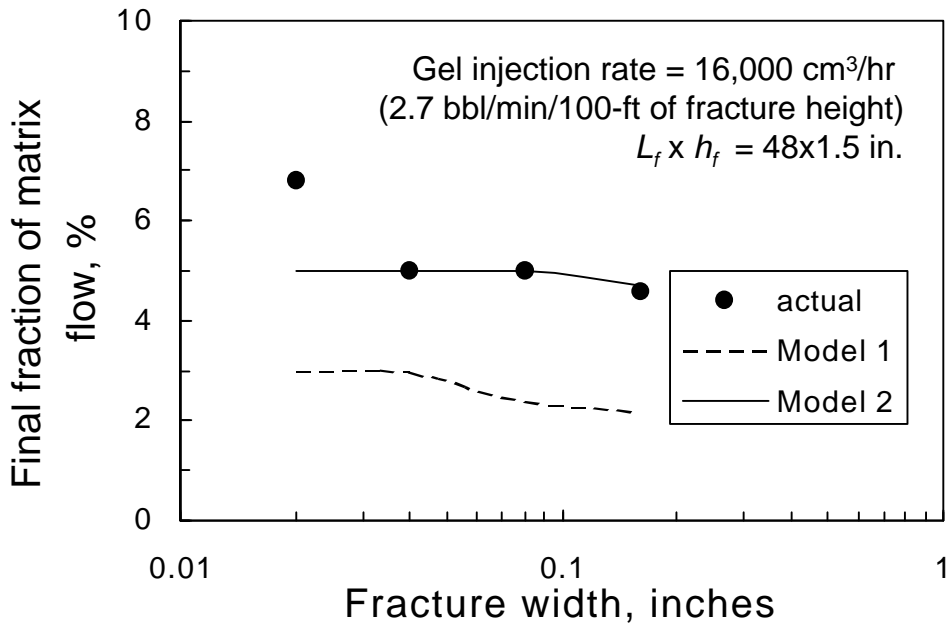


Fig. 24—Final matrix flow versus fracture width for 48x1.5-in. fractures.

The final gel compositions in the fractures are shown in Fig. 25. At this high injection rate, Models 1 and 2 gave very similar predictions for all fracture widths. The predictions matched the experimental values most closely for the widest fractures. The deviations from the actual results were quite dramatic for the narrowest fracture. We wondered whether concentrated gel was displaced from the fracture for the 0.02-in.-wide fracture.

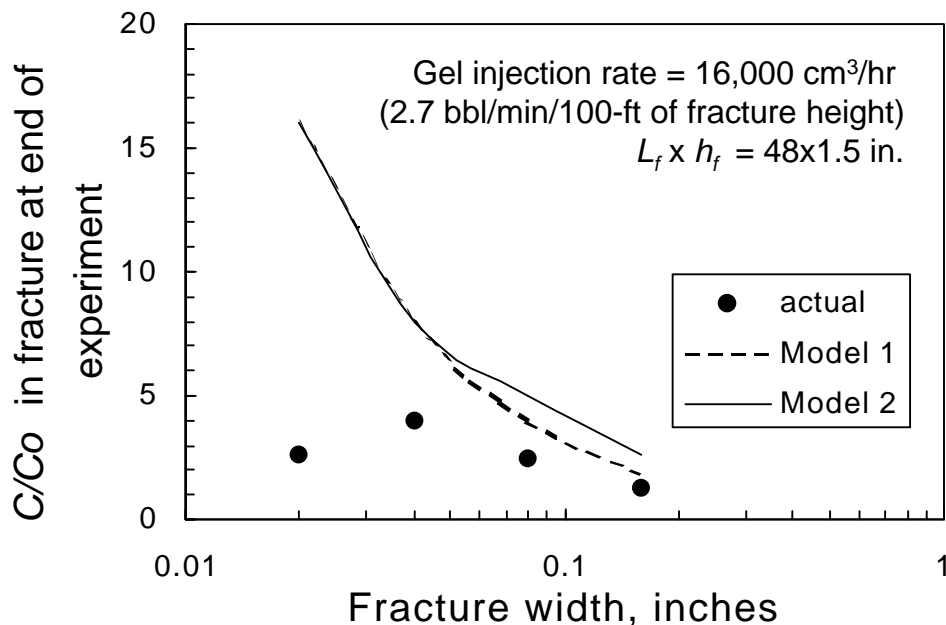


Fig. 25—Final gel concentrations in 48x1.5-in. fractures.

$$u_l = 0.05 t^{-0.55} \text{ versus } u_l = \int 0.05 t^{-0.55} dL / L$$

For the projections of gel propagation in Model 2, the average leakoff rate (for the entire gel-contacted length of the fracture) was given by Eq. 3 for all times and all frontal positions. Using Eq. 3 with Eq. 5, predictions of gel propagation through fractures are fairly easy to make. However, some uncertainty exists about the validity of this treatment. To explain, consider a gel bank that has reached 100 feet along a fracture after 4 hours of gel injection. In Model 2, we assume that the average leakoff rate along the 100-ft gel-contacted interval is given by inputting 4 hours (0.167 days) into Eq. 3—giving a leakoff rate of 0.134 ft³/ft²/d.

However, the average leakoff rate can be determined another way. In particular, Eq. 6 could be used to sum the leakoff contributions from the gel-contacted parts of the fracture.

$$u_l = \int 0.05 t^{-0.55} dL / L \dots\dots\dots(6)$$

In this method, the time of gel contact decreases with increasing position away from the wellbore. After four hours of gel injection, the local leakoff rate near the wellbore is estimated simply by inputting 4 hours into Eq. 3. In contrast, near the gel front (i.e., ~100 ft into the fracture), the gel contact time is very short and the local leakoff rate from Eq. 3 is quite high. For

any given total injection time, Eq. 6 averages the leakoff contributions from the entire length of the gel contacted-fracture. We will call this method, “Model 3”.

How do the predictions from Eqs. 3 (Model 2) and 6 (Model 3) compare? Fig. 26 provides this comparison for a 0.04-in.-wide, 100-ft-high fracture with a gel injection rate of 1 barrel per minute (BPM). The y-axis plots the leakoff rate (averaged over the entire gel-contacted portion of the fracture) for a given position of the gel front (shown on the x-axis). This plot assumes that the gel front moves at exactly the same rate for both sets of predictions. (Of course, this assumption is not valid, but it allows a direct comparison of leakoff calculations from the two methods.) Fig. 26 reveals that for a given frontal position (at the same time), leakoff rates from Eq. 6 were from 10% to 50% greater than those from Eq. 3.

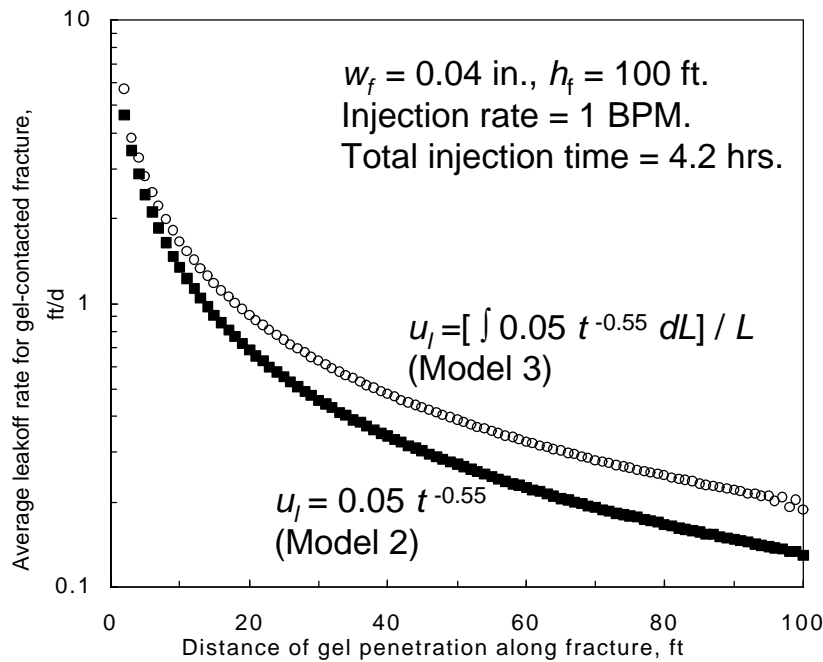


Fig. 26—Comparison of leakoff rates calculated by two methods (at identical times).

Do these differences significantly affect the rate of gel propagation through a fracture? In Fig. 27, the two methods are compared by plotting the time required (shown on the y-axis) for gel to reach a given distance along a fracture (x-axis). This figure reveals substantial differences in the predicted rates of gel propagation. To reach 100 ft along the fracture, Eq. 6 predicts that gel must be injected for twice the period predicted using Eq. 3. Since both cases used a fixed injection rate (1 BPM), twice the gel volume is required using Eq. 6 compared with Eq. 3. Thus, the two methods do predict significantly different rates of propagation.

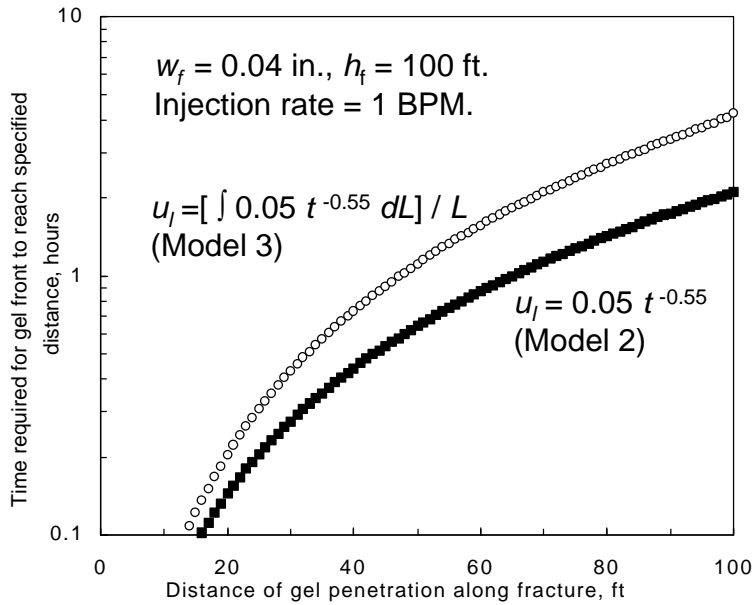


Fig. 27—Comparison of gel propagation rates calculated by two methods.

Which method is correct? At present, our only means to address this question is to compare predictions from the two models with the experimental results from our relatively short (4-ft-long) fractured cores. Fig. 28 compares the leakoff predictions from Models 2 and 3. The solid line was taken directly from Fig. 10 (Eq. 3), while the data points in Fig. 28 show the predictions from Model 3 for extrusion experiments at four different rates (corresponding to the four 48x1.5x0.04-in. fractures from Fig. 10). A comparison of Figs. 10 and 28 does not establish which model is superior. Both models fit the experimental data very well.

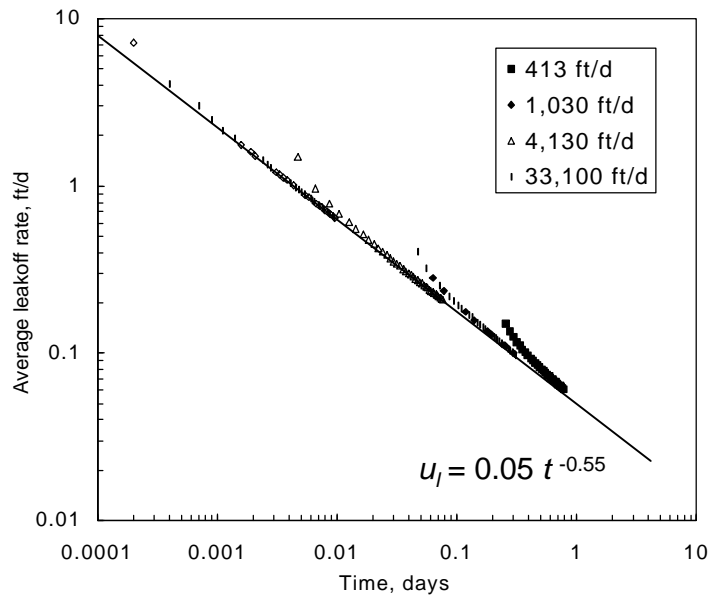


Fig. 28—Leakoff rates predicted from Model 3 (data points) versus Model 2 (line).

Model 3 was applied to predict gel propagation through our 4-ft-long fractures at three rates ranging from 413 to 4,130 ft/d. These predictions are compared with experimental results in Fig. 29, which is analogous to Figs. 4 and 11. A comparison of Figs. 11 and 29 reveals that Model 2 matches the experimental results significantly better than Model 3.

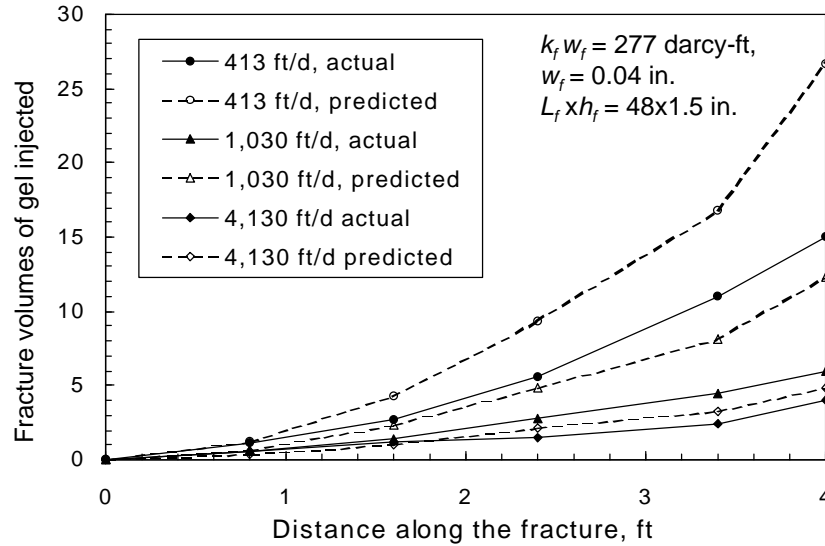


Fig. 29—Gel propagation in 48×1.5×0.04-in. fractures. Model 3: $u_l = \int 0.05 t^{-0.55} dL / L$.

Gel breakthrough values are shown in Fig. 30 for four gel extrusion experiments in 48x1.5x0.04-in. fractures where gel was injected at fluxes ranging from 413 to 33,100 ft/d. Predictions made using Models 1, 2, and 3 are also shown. Models 2 and 3 provided similar breakthrough predictions for the two highest rates. However, Model 2 significantly out-performed Model 3 at the two lower rates.

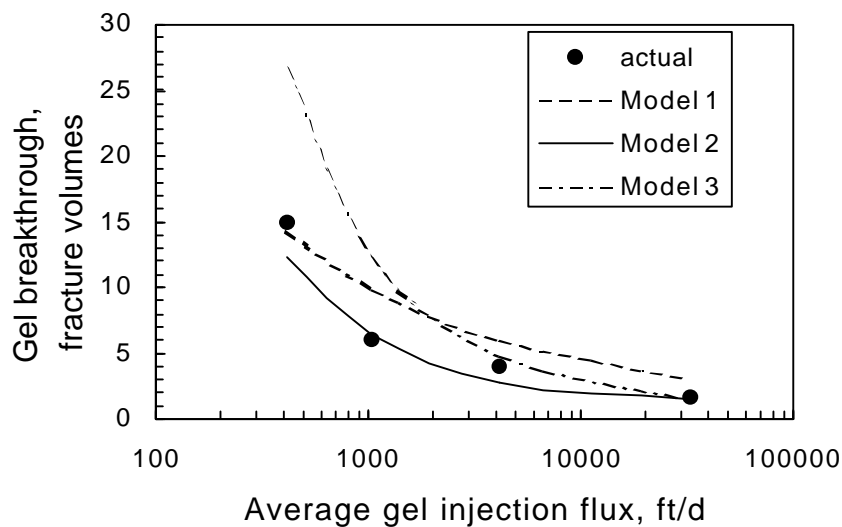


Fig. 30—Gel breakthrough versus injection flux for 48x1.5x0.04-in. fractures.

After extruding 80 fracture volumes of gel, the final gel concentrations in the fractures are shown in Fig. 31. The experimental data points are the same as those shown in Fig. 15. This figure also shows predictions from Models 1, 2, and 3. As mentioned during the discussion of Fig. 15, for reasons that we don't yet understand, Model 1 provided the best match with the experimental data. (As a reminder, Model 2 out-performed Model 1 with most other predictions.) The main point from Fig. 31 is that Model 3 did not match the experimental data any better than Model 2.

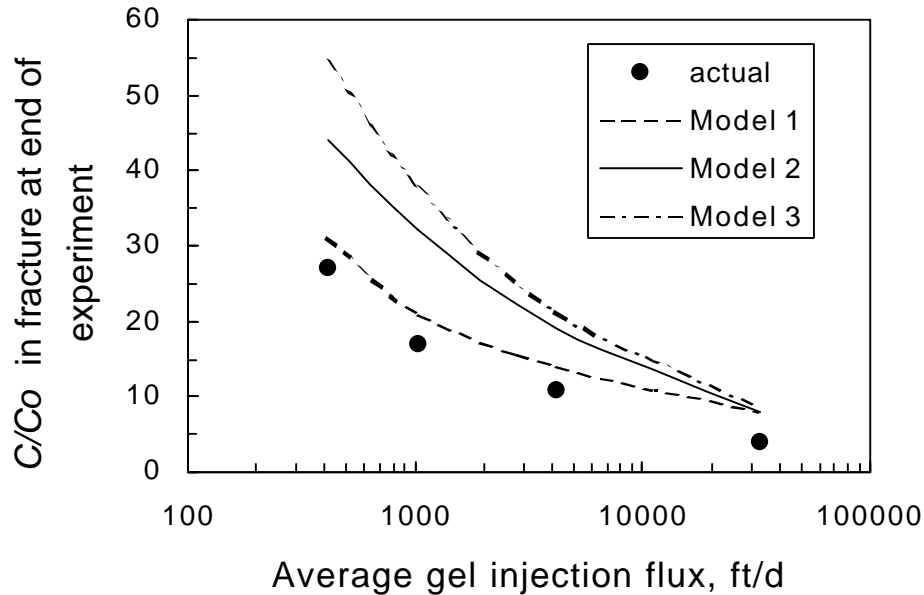


Fig. 31—Final gel concentrations in 48x1.5x0.04-in. fractures.

More work is needed to establish the best model for gel propagation and dehydration. However, based on our work to date, Model 3 does not appear superior to Model 2. This observation will be reinforced in the next section, where we consider the effects of fracture length. Model 2 is easier to apply than Model 3. Therefore, until contrary evidence is obtained, we recommend using Model 2 to predict gel propagation and dehydration in fractures.

Effect of Fracture Length

To this point, we described extrusion experiments in fractures with lengths ranging from 0.5 to 4 ft. Of course, we are interested in whether our models for gel propagation are valid in longer fractures. Consequently, we performed two experiments in 16-ft-long fractured cores (i.e., fracture dimensions were 192x1.5x0.04 in.) and one experiment in a 32-ft-long fracture (fracture dimensions were 384x1.5x0.08 in.). To make a 16-ft-long fracture, we connected four of our 4-ft-long fractures in series, while eight 4-ft-long fractures were connected to make the 32-ft-long fracture. (Each core was prepared from 650-mD Berea sandstone and had dimensions of 48x1.5x1.5 in.) In each core, the effluent from the fracture was isolated from the effluent from the matrix. For each core, the effluent from the matrix was collected (separately), measured, and analyzed. The effluent from the fracture was piped directly (via 4-in.-long, 0.25-in.-ID tubes) to the inlet of the fracture for the next core in the series. Other aspects of these floods were performed the same way as in our normal 4-ft-long fractured cores.

16-ft-Long Fractures. In the first experiment in a 16-ft-long fracture, 3.7 liters of gel were injected at a flux of 2,070 ft/d (volumetric injection rate of 1,000 cm³/hr). The gel front did not reach the end of the fracture during this experiment. In fact, pressure gradients indicated that the gel did not enter the final 4-ft-long fracture section. Near the end of gel injection, the pressure gradients averaged 20.3 psi/ft in the first 4-ft-long fracture section and 39.2 psi/ft in the second 4-ft-long section. These values were higher than predicted by Eq. 1, but they still fall on the trend shown in Fig. 1 (i.e., for a 0.04-in.-wide fracture).

In the second experiment in a 16-ft-long fracture, 3.7 liters of gel were injected at a flux of 10,330 ft/d (volumetric injection rate of 5,000 cm³/hr). The gel front reached the end of the 16-ft-long fracture after injecting 10.7 fracture volumes. After gel breakthrough, pressure gradients along the fracture averaged 14.3 psi/ft and were reasonably constant in all four fracture sections. This value is very close to that predicted by Eq. 1.

Effluent collected from the matrix taps from these two experiments were used to generate the leakoff plot shown in Fig. 32. Eq. 3 (Model 2) described the leakoff data very well in both experiments. In Fig. 33, for the experiment at 10,330 ft/d, the individual leakoff rates for each of the four 4-ft-long fracture sections are plotted (open symbols) and compared with the leakoff rates for the entire gel-contacted part of the 16-ft-long fracture (solid circles). The leakoff rates from the individual core segments cluster fairly consistently with the composite average values.

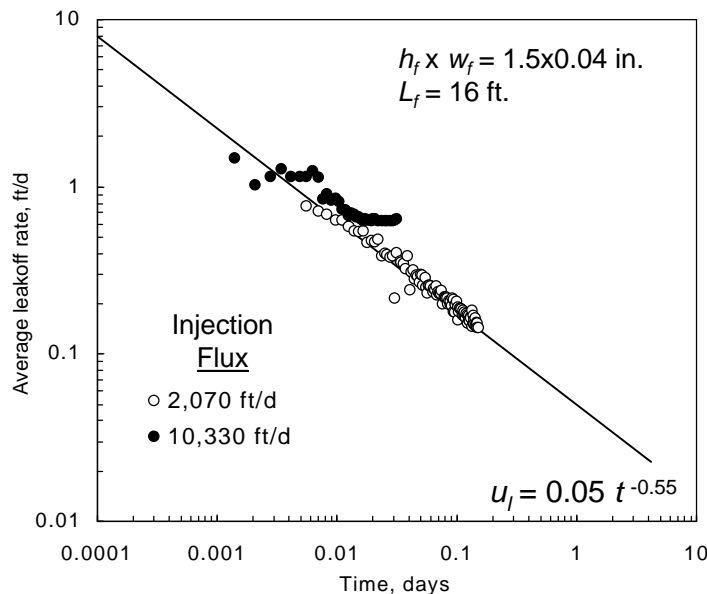


Fig. 32—Leakoff rates in 16-ft-long fractures.

For the first 16-ft-long fracture, pressure gradients along the fracture were used to determine gel-front arrival times for the first two 4-ft-long sections. The final gel-front position was determined by opening the fracture at the end of gel injection and analyzing gel composition along the fracture. After 3.7 hours and 3.7 liters of gel injection (20 fracture volumes), the gel reached 10.3 ft along the 16-ft-long fracture. The times required for gel to reach various distances along the fracture are plotted in Fig. 34. These values are compared with predictions from the three models

that we presented earlier. Interestingly, for the 8-ft and 10.3-ft positions, the actual propagation times exceeded the times predicted by all three models.

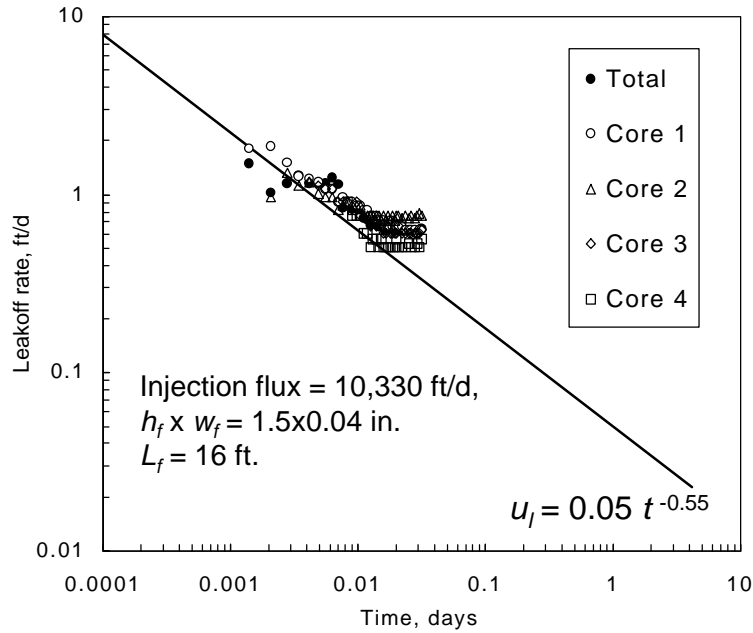


Fig. 33—Leakoff rates in second 16-ft-long fracture: Total versus each section.

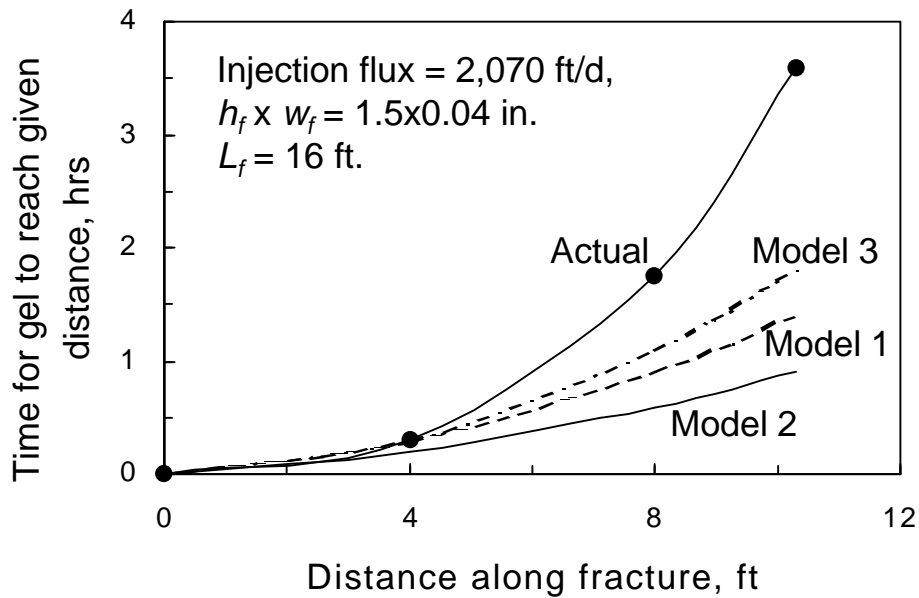


Fig. 34—Gel propagation at 2,070 ft/d in the first 16-ft-long fracture.

A similar analysis was performed for propagation rates in the second 16-ft-long fracture. These results are shown in Fig. 35. As in the first experiment, the actual propagation times exceeded the times predicted by all three models

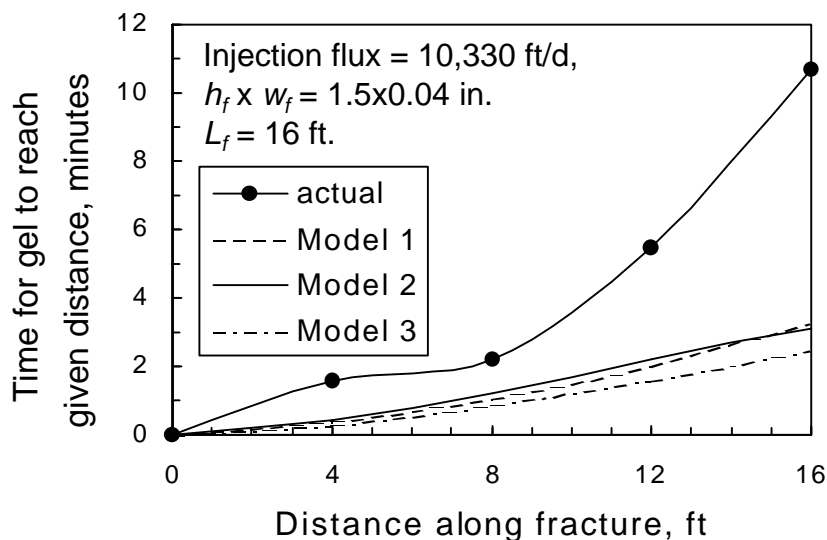


Fig. 35—Gel propagation at 10,330 ft/d in the second 16-ft-long fracture.

For the first 16-ft-long fracture, gel compositions along the fracture (at the end of the experiment) are shown in Fig. 36. In the gel-contacted portion of the fracture, the average HPAM concentration was 20 times greater than that for the injected gel. The concentrations were notably lower at the beginning and end of each fracture segment (i.e., at 0, 4, and 8 ft). We believe that this was an artifact of our method of collecting gel samples after gel injection. Neglecting these core-interface effects, polymer concentrations generally decreased through the fracture—from 30-45X in the first 4 ft to 10-15X in the last 2 ft of the gel-contacted fracture. These results are qualitatively in agreement with our earlier findings.¹⁰

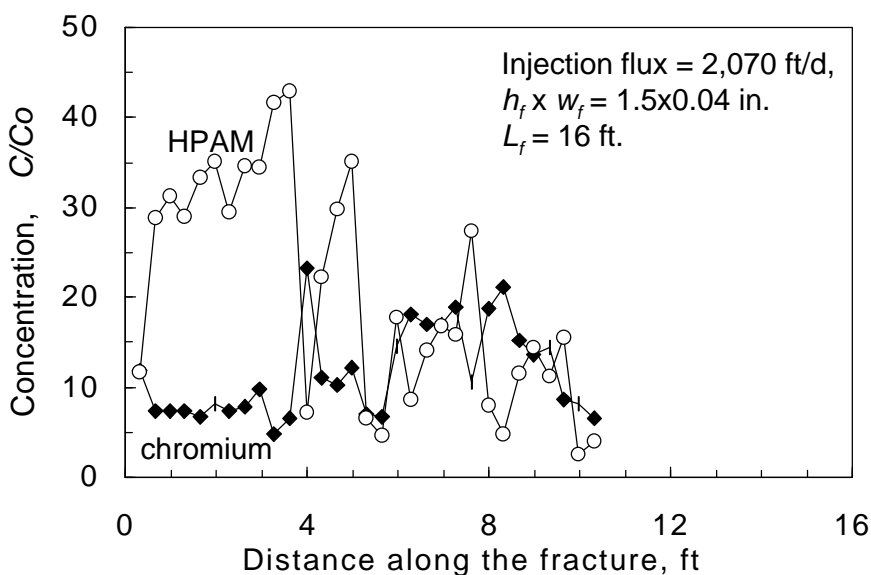


Fig. 36—Gel composition along a 16-ft-long fracture after gel placement at 2,070 ft/d.

For the second 16-ft-long fracture, gel compositions along the fracture (at the end of the experiment) are shown in Fig. 37. Compared with the composition of the injected gel, gel in the fracture averaged 3.0 times greater HPAM concentration and 4.3 times greater chromium concentration. Consistent with our earlier findings,¹² a comparison of Figs. 36 and 37 reveals that injection at higher rates leads to less gel dehydration. (Recall that 3.7 liters of gel were injected in both experiments.) In Fig. 37, two concentration peaks were noted at 2-4 ft and at 11-12 ft. We presume that these accumulations of concentrated gel occurred because of constrictions in the fracture flow path at these points. However, no obvious constrictions were evident when the fractured cores were assembled or when they were disassembled after the experiment.

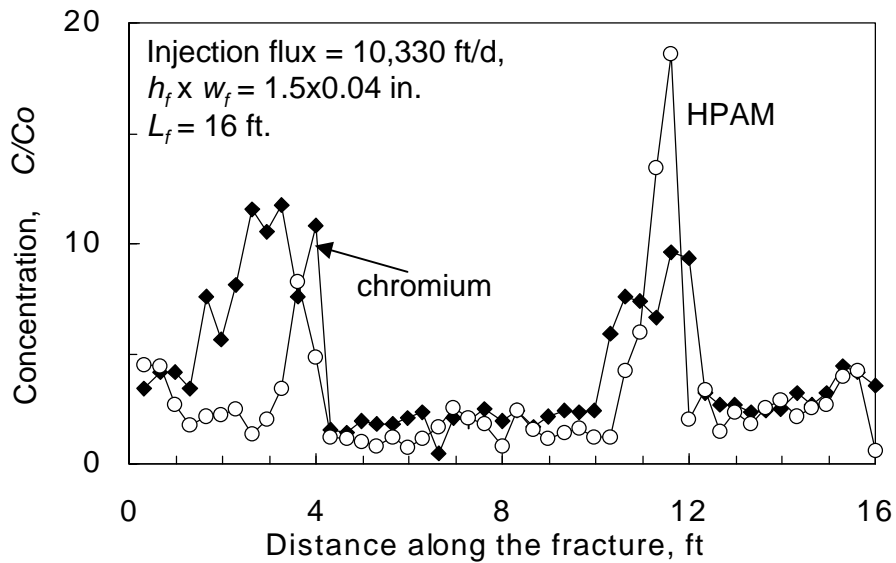


Fig. 37—Gel composition along a 16-ft-long fracture after gel placement at 10,330 ft/d.

32-ft-Long Fracture. An extrusion experiment was performed in a 32-ft-long fracture. The fracture width was 0.08 in. A greater width was used because with a 32-ft-long, 0.04-in.-wide fracture, high pressures would have burst the epoxy-cast cores during gel extrusion. Using a flux of 5,170 ft/d, 3.7 liters of gel were injected (volumetric injection rate of 5,000 cm³/hr). This rate corresponds to a field injection rate (into a two-wing fracture) of 0.84 barrels per minute per 100 ft of fracture height.

The gel front reached the end of the 32-ft-long fracture after injecting 3.3 fracture volumes. In fact, gel reached the fracture outlet shortly before the end of gel injection (3.7 liters). Pressure gradients along the fracture averaged 5.3 psi/ft and were reasonably constant in all eight fracture sections. This value is reasonably close to that predicted by Eq. 1.

Effluent collected from the matrix taps from these two experiments were used to generate the leakoff plot shown in Fig. 38. The individual leakoff rates for seven of the eight 4-ft-long fracture sections are plotted (various symbols) and compared with the leakoff rates for the entire gel-contacted part of the 32-ft-long fracture (solid circles). The leakoff rates from the individual

core segments cluster fairly consistently with the composite average values. A significant amount of scatter exists in the data, but Eq. 3 still describes the trend reasonably well. (Incidentally, no leakoff water was produced from Core 8, the last 4-ft-long fractured core in this series. This result was expected because the gel front arrived at the end of the fracture just at the end of the experiment. Previously,¹⁰ we demonstrated that downstream from the gel front, virtually all water flowed in the fracture. Significant water leakoff was only observed upstream from the gel front.)

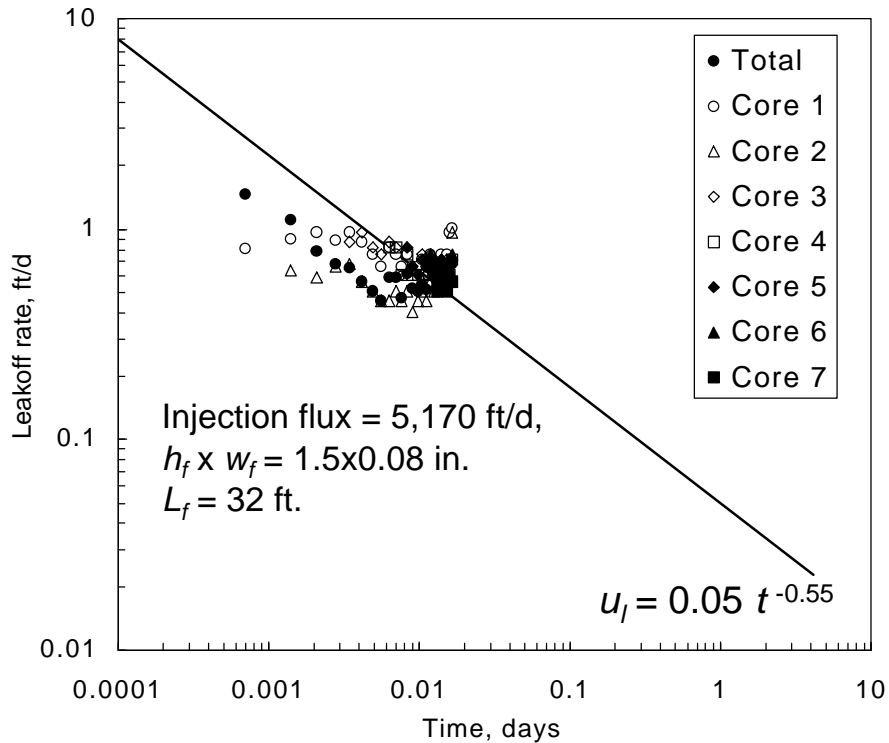


Fig. 38—Leakoff rates in a 32-ft-long fracture: Total versus each section.

The times required for gel to reach various distances along the fracture are plotted in Fig. 39. (This data was mostly determined from monitoring pressure gradients along the fracture.) These values are compared with predictions from the three models that we presented earlier. Model 2 provided the best fit to the experimental data. The actual breakthrough time matched the prediction from Model 2 perfectly. This result increases our confidence for use of Model 2 in field applications—at least in 0.08-in.-wide-fractures.

Interestingly, for most of the intermediate distances in Fig. 39, gel propagation was more rapid than predicted by the three models. In contrast, for the 16-ft-long, 0.04-in.-wide fractures, the actual propagation times exceeded the times predicted by all three models (see Figs. 34 and 35).

Fig. 40 plots gel composition along the fracture at the end of the experiment. On average, HPAM was concentrated by a factor of 1.8.

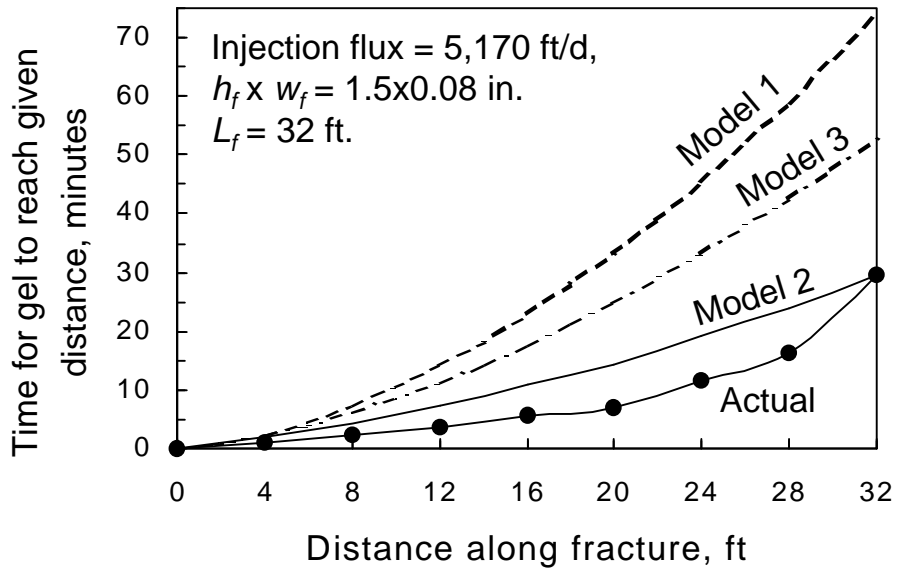


Fig. 39—Gel propagation at 5,170 ft/d in a 32-ft-long fracture.

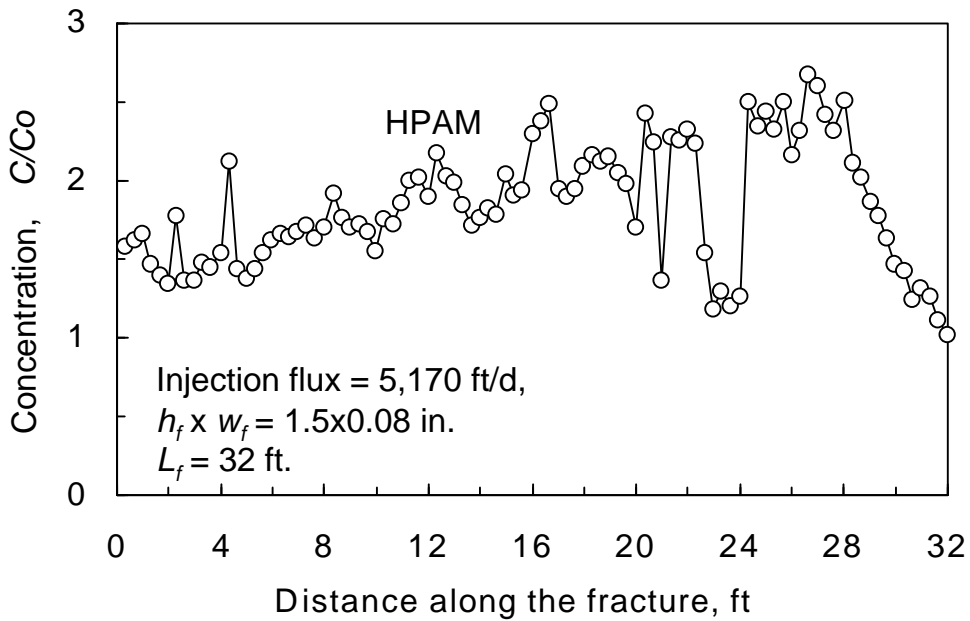


Fig. 40—Gel composition along a 32-ft-long fracture after gel placement at 5,170 ft/d.

Summary of Leakoff Data

At present, Model 2 (Eq. 3) appears the best choice for describing gel propagation and leakoff during extrusion through fractures. Fig. 41 provides a summary of all leakoff data presented to this point.

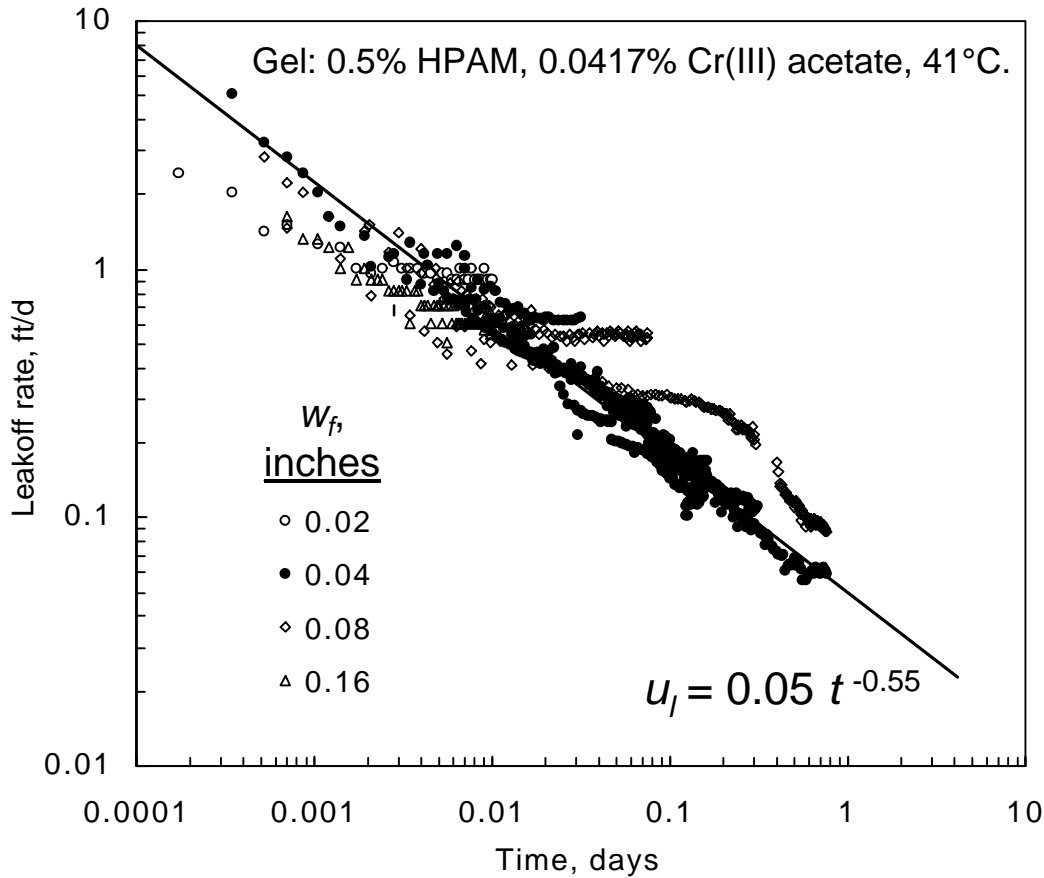


Fig. 41—Summary of leakoff data.

Fig. 41 plots the leakoff rate (u_l , in $\text{ft}^3/\text{ft}^2/\text{d}$ or ft/d) versus time (t , in days) for 16 separate experiments. The solid circles in Fig. 41 show results from 9 experiments in cores with 0.04-in.-wide fractures. In these experiments, fracture lengths ranged from 0.5 to 16 ft, fracture heights ranged from 1.5 to 12 in., and average gel injection fluxes ranged from 129 to 33,100 ft/d . Eq. 3 provided an excellent fit of the data from the 0.04-in.-wide fractures.

Five experiments were performed in fractures with widths of 0.08 in. and heights of 1.5 in. Four of these experiments were performed in 4-ft-long fractures using injection fluxes ranging from 207 to 16,500 ft/d . One experiment was performed in a 32-ft-long fracture using a flux of 5,170 ft/d . The open diamonds in Fig. 41 show the leakoff results.

One experiment was performed at a flux of 8,300 ft/d in a 0.16-in.-wide fracture. A final experiment was performed at a flux of 66,200 ft/d in a 0.02-in.-wide fracture. For these latter two experiments, fracture lengths were 4 ft and fracture heights were 1.5 in. The leakoff data from these experiments and the 0.08-in.-wide fractures do not fit Eq. 3 as well as the results from the 0.04-in.-wide fractures. Nevertheless, Eq. 3 provides a reasonable estimate of the leakoff data.

Predictions in Long Fractures

A key motivation for this work is a need to quantify how gels propagate through fractures in field applications. Of course, these fractures are much longer and higher than those examined experimentally in our research. To accurately predict behavior in field applications, a satisfactory model is required for gel propagation and dehydration during extrusion. Further testing is needed to establish whether we have the correct model. Nevertheless, the experimental results above provide hope that Model 2 can be applied to make reasonable predictions for field applications. Fig. 42 presents these predictions for three injection rates (0.1 to 10 barrels per minute, BPM) in 0.04-in.-wide, two-wing fractures using our standard Cr(III)-acetate-HPAM gel. At a given rate, Fig. 42 shows the gel volume that must be injected to achieve a given distance of penetration along the fracture. This volume increased with distance of penetration raised approximately to the 1.5 power. For a given distance of penetration, the required gel volume decreased substantially with increased injection rate. For example, to penetrate 200 ft, the required gel volume was 5 times less at 10 BPM than at 1 BPM. Therefore, to maximize gel penetration, the highest practical injection rate should be used.

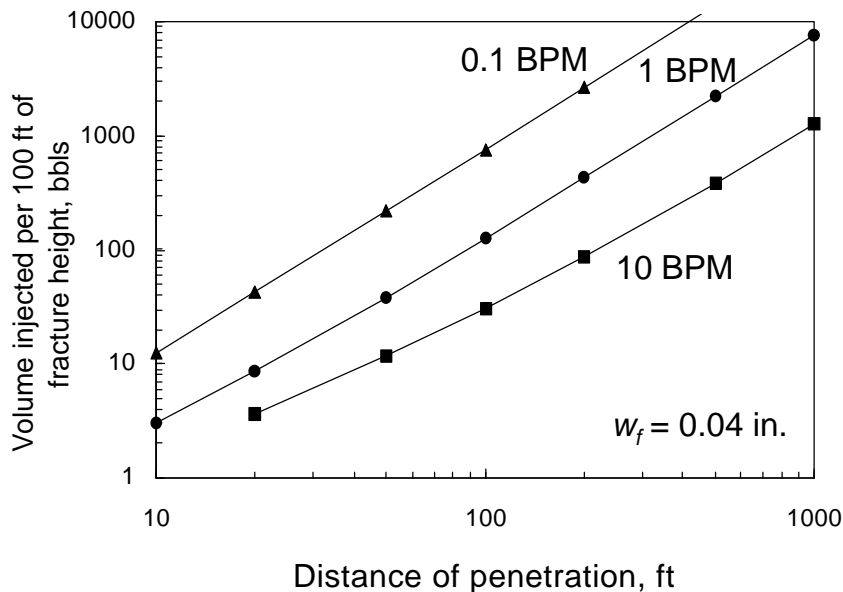


Fig. 42—Model predictions in long two-wing fractures at different rates.

At this point, it may be overly optimistic to expect Eq. 3 to be generally valid for all fracture widths. Nevertheless, out of curiosity, we applied the model assuming that it was valid for fracture widths ranging from 0.01 to 1 in. Fig. 43 plots the predicted distances of gel penetration versus the volume of gel injected for three fracture widths during gel injection at 1 barrel per minute. Interestingly, the curves came together at high distances of penetration and low fracture widths. This result occurred because the rate of gel propagation was governed increasingly by the rate of gel dehydration (i.e., water leakoff given by Eq. 3) as fracture width decreased or as the desired distance of gel penetration increased. In contrast, for a fixed injection rate, gel propagation was governed simply by the fracture width (or volume) for large fracture widths or small distances of gel penetration.

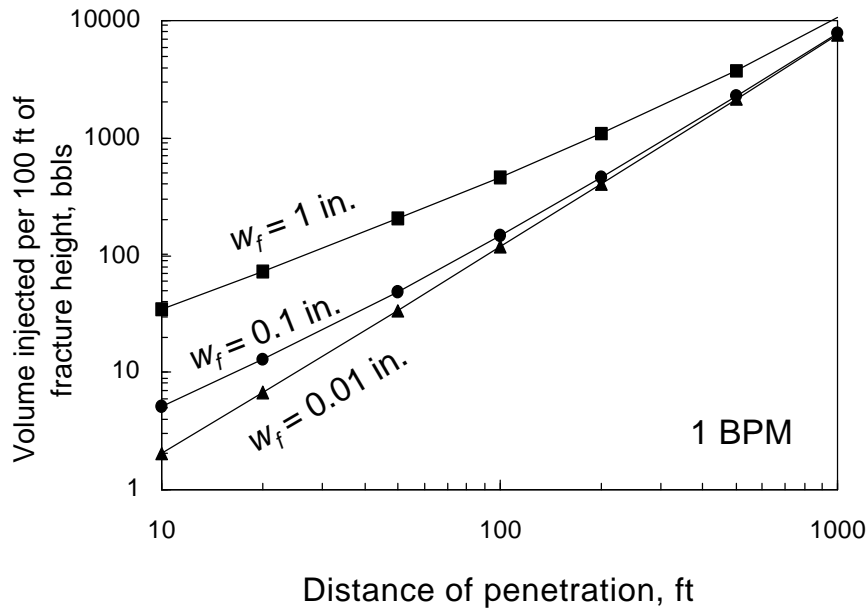


Fig. 43—Model predictions in long two-wing fractures with different widths.

A useful rule of thumb can be realized from the 1.5-power dependence of volume on distance of penetration in Figs. 42 and 43 (i.e., at moderate to large distances of penetration). Specifically, if the volume of gel needed to reach a certain distance of penetration is known, then reaching twice that distance requires injecting roughly three times the gel volume. In contrast, for “normal” behavior (i.e., if dehydration did not occur), doubling the distance of penetration only requires a doubling of gel volume. This “normal” behavior is approached for small distances of penetration and wide fractures. For example, in Fig. 43, the 1-in.-wide fracture approaches normal behavior for small distances of penetration (i.e., the slope approaches 1).

Model 1. Gel propagation rates were also predicted using Model 1. These predictions were documented in Ref. 10. This model suggested that the maximum distance of gel penetration into a fracture is inversely proportional to the square root of gel permeability and directly proportional to the 1.5 power of fracture width. Model 1 also predicted that the maximum distance of gel penetration is proportional to the square root of injection rate. Consistent with Model 2, Model 1 indicated that to maximize gel penetration along a fracture, the highest practical injection rate should be used. However, Model 1 was generally much more pessimistic than Model 2 concerning the distance that gel can propagate into a fracture. This result occurred because Model 1 allowed greater leakoff rates than Model 2 at intermediate and long times. Since we believe that Model 2 more correctly accounts for leakoff (Fig. 41), we currently have more confidence in Model 2.

Rapid versus Slow Injection. Our experimental results and calculations indicate that to maximize gel penetration along a fracture, the gel should be injected as rapidly as practical. However, in wide fractures, gel dehydration may be desirable to form rigid gels that are less likely to washout after placement. In these applications, reduced injection rates may be appropriate. Our models may be useful in estimating final gel concentrations as a function of injection rate.

Physical Basis for Eq. 3

What is the physical basis for Eq. 3? Because leakoff varies approximately with the square root of time, one might guess that the relation is analogous to the formation of a filter cake during hydraulic fracturing.¹³ However, important differences exist. For normal (incompressible) filter cake formation, a cake forms with permeability, k , and uniform thickness, L . For a given pressure difference, Δp , and solvent viscosity, \mathbf{m} the solvent flux (leakoff rate), u , through the filter cake is given by the Darcy equation.

$$u = k\Delta p/(\mathbf{m}L) \dots\dots\dots (7)$$

The filter cake thickness increases with solvent throughput according to Eq. 8.

$$L = c_c \int u dt \dots\dots\dots (8)$$

Combining Eqs. 7 and 8, the leakoff rate is easily shown to vary with the square root of time.¹³

However, in our problem, where water leakoff occurs during gel extrusion through a fracture, a filter cake of uniform thickness does not form. In particular, we have not observed a gel concentration variation (i.e., a filter cake) in the width direction of the fracture. In contrast, we have noted gel concentration variations along the length and height directions. These latter variations were caused by mobile gel (with a composition of the originally injected gel) that wormholed through immobile, concentrated (dehydrated) gel.^{10,12}

Our current picture of the gel propagation and dehydration process is as follows: When the gel front first contacts a new element of fracture area, the gel in this vicinity basically has the same composition as that for the originally injected gel.^{10,12} The permeability of this gel to water is relatively high—around 1 mD.¹ Consistent with these observations, the rate of water leakoff (i.e., leakoff flux) from the gel (and fracture) is greatest just upstream of the gel front.¹⁰ As water leaks off from the gel, the gel concentrates and becomes immobile in the vicinity where dehydration occurred. The next element of fresh (mobile) gel must find its way around or through (i.e., wormhole through) the concentrated gel in order to advance the gel front. With time at a given position along the fracture, our experiments reveal that the average gel concentration increases and the fracture area contacted by wormholes (i.e., mobile gel) decreases.^{10,12}

At any given distance along the length of a fracture, a fraction of the fracture area will be contacted by immobile, concentrated gel, while the remaining area will be contacted by mobile gel (where the wormholes exist). Thus, two separate sources contribute to leakoff—(1) concentrated, immobile gel that was formed from the dehydration process and (2) mobile gel. Thus, the leakoff rate (u_l) at any position along a fracture is the sum of leakoff from the mobile gel and the immobile gel. In turn, each of these contributions is proportional to the fracture area contacted by mobile (fresh) gel (a_f) and immobile (concentrated) gel (a_c) and the local leakoff rates from the mobile gel (u_f) and the immobile gel (u_c).

$$u_l = a_f u_f + a_c u_c \dots\dots\dots (9)$$

The immobile gel continually concentrates during the extrusion process.¹⁰ We believe that this contribution is minor for the vast majority of the extrusion process because gel permeability to water varies inversely with the third power of gel concentration.¹

$$u_c = u_f (C/C_o)^{-3} \dots\dots\dots(10)$$

As the immobile gel in the fracture becomes more concentrated, its ability to squeeze out additional water rapidly decreases. Furthermore, experimental studies (using leakoff of dyed water) demonstrated that the dominant source of leakoff was from the mobile gel in the wormholes.^{1,12} When an element of mobile gel dehydrates, presumably a thin filter cake of concentrated gel forms on the fracture wall. However, because we have never physically observed this thin layer, we assume that it must be quickly torn and swept to the side (by water trying to reach the fracture face) to merge with the concentrated immobile gel.

Given that the second term in Eq. 9 is negligible, the rate of leakoff is determined mainly by leakoff from fresh (mobile) gel in the wormholes.

$$u_l \approx a_f u_f \dots\dots\dots(11)$$

Since the gel in the wormholes is continually replenished, the local leakoff rate, u_f , remains relatively constant during the extrusion process. This fact (along with Eqs. 3 and 11) implies that the fracture area contacted by wormholes must vary with $t^{-0.55}$. Fig. 41 indicates that the leakoff rate should be 8 ft/d at 0.0001 days. Somewhat arbitrarily, we choose a_f to have a value of one at this time. Thus, Eq. 12 provides a credible relation for a_f at times greater than 0.0001 days (~9 seconds).

$$a_f = (0.05/8) t^{-0.55} \dots\dots\dots(12)$$

This equation is plotted on the left side of Fig. 44. The right side of Fig. 44 plots the fraction of the fracture area that was contacted by concentrated gel (a_c) versus time. These plots indicate that after 0.0004 days (35 seconds) of gel contact, most of the fracture face is covered by concentrated gel rather than fresh gel.

Given that gel becomes immobile after it dehydrates, a mass balance can be used to determine the average concentration as a function of time. (w_f is expressed in ft in these equations.)

$$C/C_o = 2 \int u_l dt / w_f \dots\dots\dots(13)$$

Combining Eqs. 3 and 13 leads to Eq. 14.

$$C/C_o = 0.22 t^{0.45} / w_f \dots\dots\dots(14)$$

This equation is plotted in Fig. 45. In a 0.04-in.-wide fracture, the average gel concentration is predicted to be 3, 10, and 30 after 1.5 minutes, 22 minutes, and 4.2 hours, respectively.

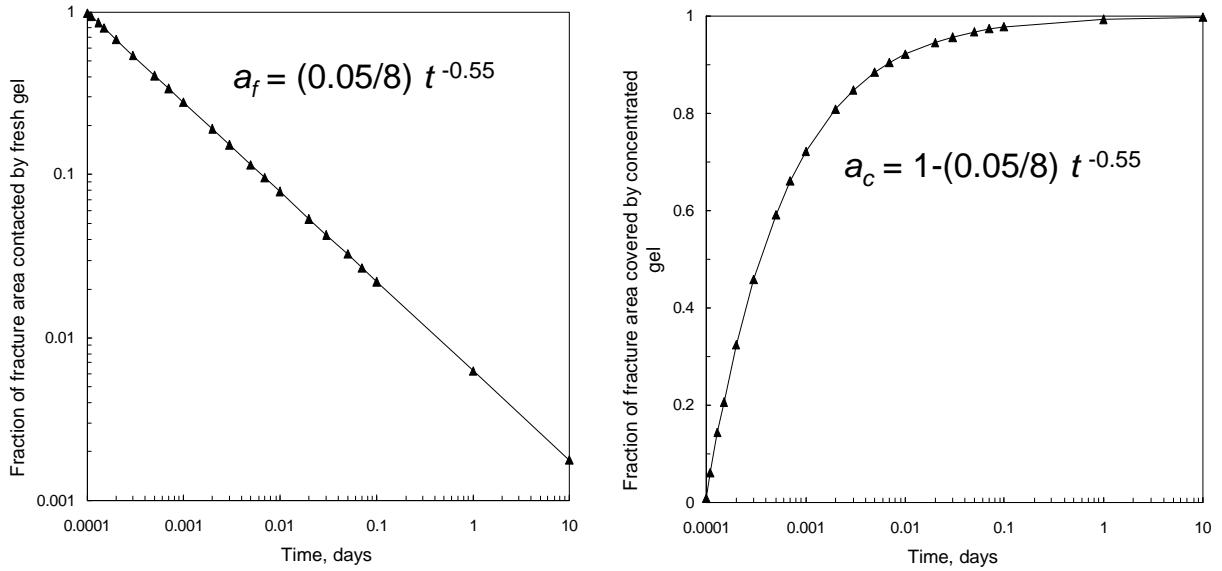


Fig. 44—Predictions of fraction of fracture area contacted by fresh versus concentrated gel.

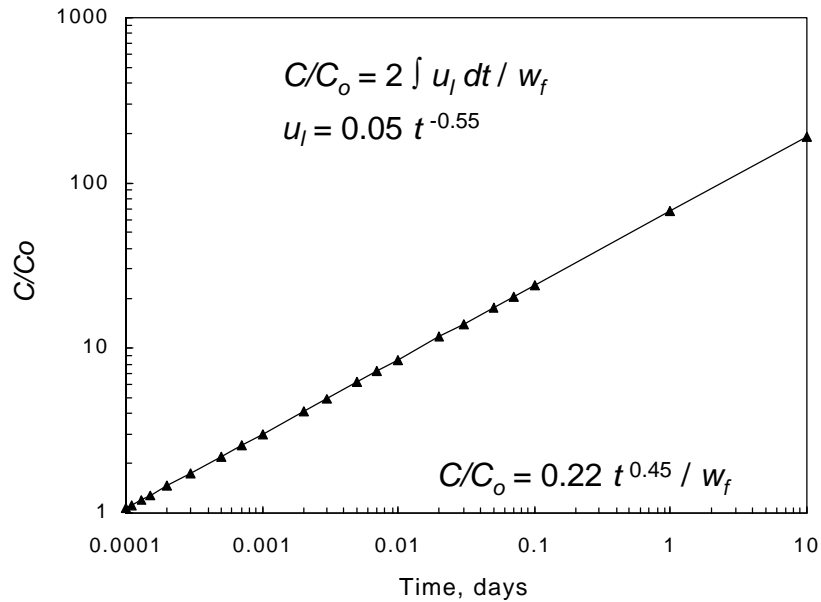


Fig. 45—Gel concentration versus time ($w_f = 0.04$ in.).

Earlier, we suggested that the leakoff contribution from immobile gel is negligible. To test this assumption, Eq. 10 was combined with Eq. 14 to generate Eq. 15 and Fig. 46.

$$u_c = 751 t^{-1.35} (w_f)^3 \dots\dots\dots(15)$$

For $w_f = 0.04$ in., Fig. 46 demonstrates how rapidly leakoff diminishes from concentrated gel.

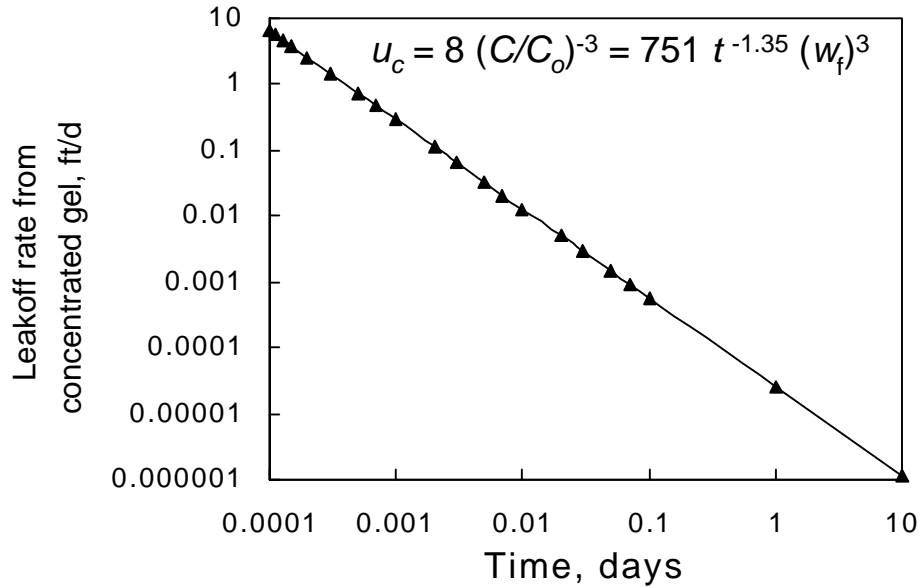


Fig. 46—Leakoff rate from concentrated gel ($w_f = 0.04$ in.).

Consideration of Figs. 44 and 46 raises the question, at a given point in a fracture, how does the overall leakoff contribution from fresh gel compare with that from concentrated gel? This point is addressed by plotting the ratio, $a_f u_f / a_c u_c$. This ratio can be determined by combining Eqs. 12 and 15. Eq. 16 was used to generate Fig. 47.

$$a_f u_f / a_c u_c = (0.05/8) t^{-0.55} (8) / \{ [1 - (0.05/8) t^{-0.55}] [751 t^{-1.35} (w_f)^3] \} \dots\dots\dots(16)$$

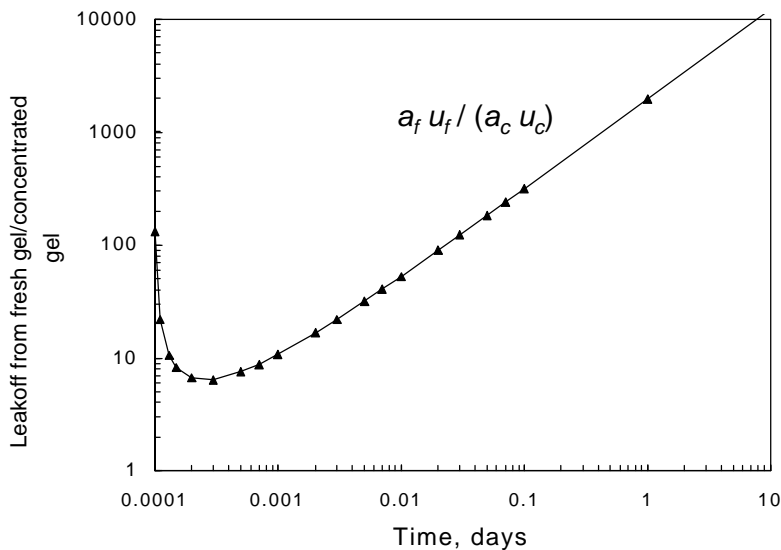


Fig. 47—Leakoff from fresh gel relative to concentrated gel ($w_f = 0.04$ in.).

The above figure shows that at any given point and time along a fracture, the total leakoff from fresh gel is significantly greater than that from the concentrated gel. For a contact time of 0.0003 days (26 seconds), the ratio, $a_f u_f / a_c u_c$, reached a minimum value of 6.5. Thereafter, the ratio rose continuously—confirming that leakoff from the concentrated gel became progressively less significant.

$1/(w_f)^2$ Dependence for Pressure Gradients

The pressure gradient required for gel extrusion varies roughly inversely with the square of fracture width (Eq. 1 and Fig. 1):

$$dp/dl = 0.02 / (w_f)^2, \dots\dots\dots(1)$$

where dp/dl has units of psi/ft and w_f has units of in. A significant amount of data scatter exists in Fig. 1. However, this scatter can be contained between the two relations described by Eqs. 17 and 18 (see Fig. 48).

$$dp/dl = 0.005 / (w_f)^2 \dots\dots\dots(17)$$

$$dp/dl = 0.08 / (w_f)^2 \dots\dots\dots(18)$$

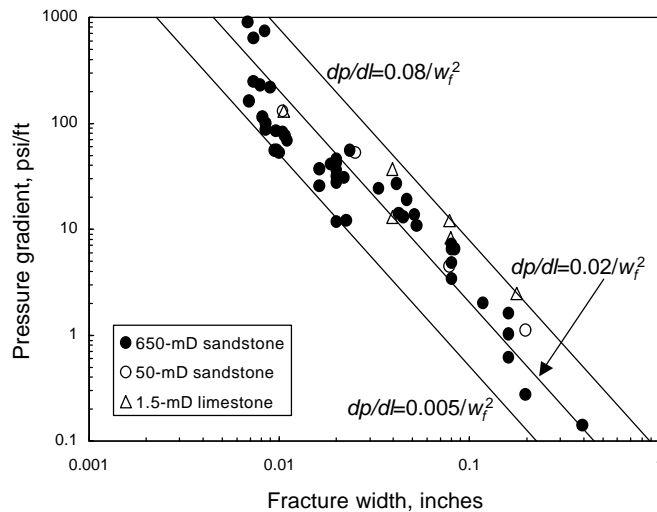


Fig. 48— $1/(w_f)^2$ relations that contain the data scatter.

Thus, for a given fracture width, Eq. 1 estimates the pressure gradient within an order of magnitude. Consideration of Fig. 48 suggests that the uncertainty for an estimate could be reduced if the data were fit to an S-shaped curve instead of using Eq. 1.

Eq. 1 fits the data much better than relations based on standard yield-stress analysis. For a material with a yield stress, t_y , a simple force balance¹⁴ predicts that the pressure gradient required for extrusion should be given by Eq. 19.

$$dp/dl=2t_y/w_f \dots\dots\dots(19)$$

Fig. 49 compares the data fit for relations using $1/w_f$ versus using $1/(w_f)^2$. In particular for Eq. 19, $2t_y$ was assigned a value of 0.5 psi-in./ft. Obviously, the $1/(w_f)^2$ relation provided a much better fit than the $1/w_f$ relation.

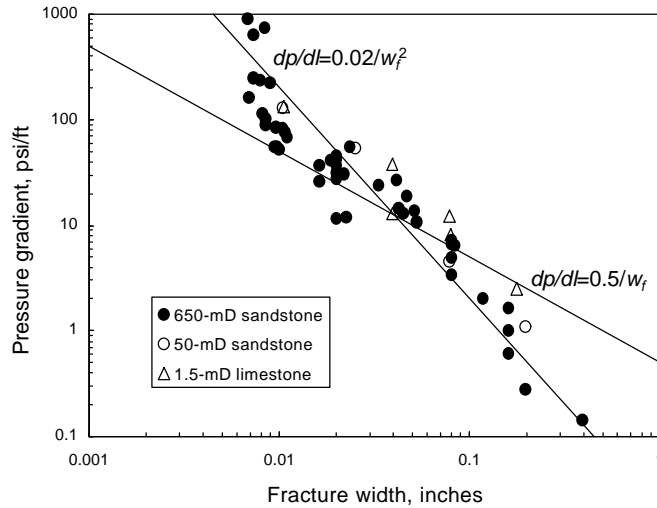


Fig. 49—Comparison of $1/(w_f)^2$ versus $1/w_f$ relations.

Relation Between Shear-Thinning and $1/(w_f)^2$ Dependence for Pressure Gradients

Although a relation is not yet evident between the pressure gradient for gel extrusion through a fracture and yield stress in a viscometer,¹⁴ a relation does exist between pressure gradient for gel extrusion and shear-thinning behavior observed in fractures and tubes. In earlier work,⁸ we found that gels show an extremely strong apparent shear-thinning behavior when extruding through fractures and tubes. In particular, Fig. 50 shows that the gel resistance factor, F_r , (apparent viscosity relative to water) in the fracture decreases substantially with increased superficial velocity, u , (i.e., fluid flux in the fracture). The slope of the data plotted in Fig. 50 is in the range from -0.83 to -0.95 . In other words, the data in Fig. 50 can be approximated using Eq. 20.

$$F_r = c_a u^n \dots\dots\dots(20)$$

where c_a is a constant (with a value of $\sim 2 \times 10^6$ days/ft for much of the fracture data in Fig. 50), and n is the flux exponent (i.e., -0.83 to -0.95).

The steep slopes of the curves in Fig. 50 indicate that the pressure gradient is fairly insensitive to fluid velocity over much of the flux range. This fact was demonstrated explicitly in Fig. 4 of Ref. 8. It can be understood simply by combining Eq. 20 with the Darcy equation.

$$dp/dl = u m k_f = u m_w F_r / k_f = u^{(n+1)} c_a m_w / k_f \dots\dots\dots(21)$$

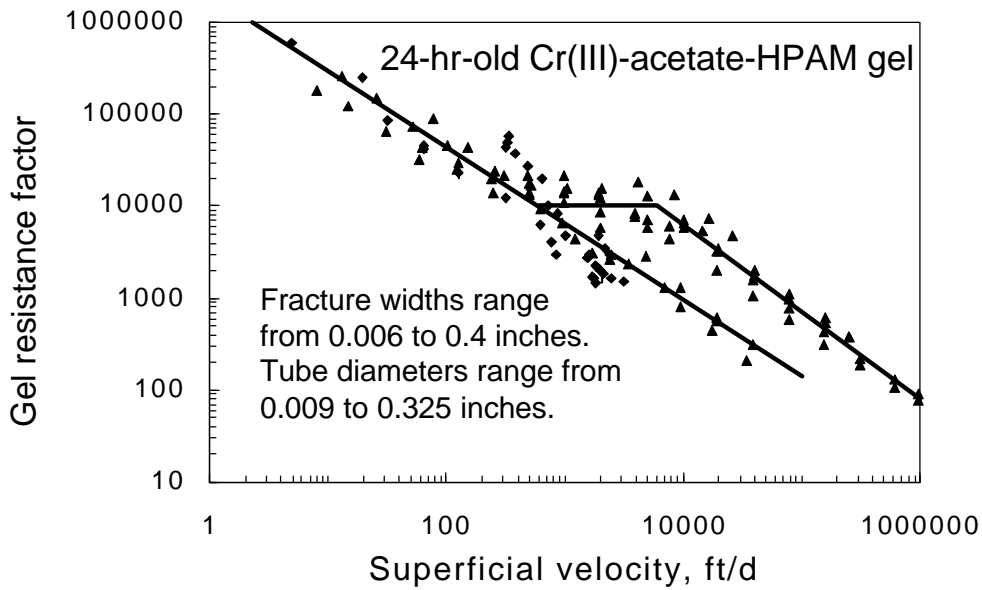


Fig. 50—Gel resistance factors versus superficial velocity.⁸

Since the flux exponent, n , is nearly -1 , Eq. 21 reduces to Eq. 22.

$$dp/dl \approx c_a \mathbf{m}_w / k_f \dots \dots \dots (22)$$

This equation indicates that the pressure gradient is basically independent of flow rate. For gel to flow in a given fracture, Eqs. 21 and 22 predict that about the same pressure gradient is required for a near-zero flow rate as that when high flow rates are used. This suggestion is consistent with our observations that gel will not enter a fracture if the pressure gradient is not sufficiently high.⁹

Since fracture permeability is proportional to the square of fracture width,⁹ Eq. 22 can be transformed to Eq. 23.

$$dp/dl \approx c_a c_b \mathbf{m}_w / (w_f)^2, \dots \dots \dots (23)$$

where c_b is a constant. Note the similarity of Eqs. 1 and 23. Eq. 1 was based on experiments where injection rates were held constant, but fracture widths varied widely (Fig. 1). In contrast, Eq. 23 was derived from experiments where fluxes (superficial velocities) varied over a wide range (Fig. 50). The success of Eqs. 1, 20, and 23 in describing the experimental results follows directly from our observation that for a given fracture width and conductivity, a minimum pressure gradient is required for gel extrusion. Given values of 2×10^6 days/ft for c_a , 1.82×10^{-8} darcy/in.² for c_b , and 0.67 cp for \mathbf{m}_w , Eq. 23 reduces to Eq. 24—which also describes Eq. 1.

$$dp/dl \approx 0.02 / (w_f)^2 \dots \dots \dots (24)$$

Upper Limit for the Rate of Gel Injection

Tables 1 and 3 revealed that the pressure gradients during gel extrusion were insensitive to injection rate. This finding was important to our conclusion that gel should be injected as rapidly as possible to maximize penetration. Does an upper rate limit exist for this generalization? Intuitively, the pressure gradient during gel extrusion should not be less than that during water injection at the same rate. For water injection during laminar flow, Eq. 25 describes the pressure gradient in a fracture.

$$dp/dl = 12 q\mu_w / [h_f (w_f)^3] = q\mu_w / [h_f k_f w_f] \dots\dots\dots(25)$$

Eqs. 1 and 25 can be combined to estimate the upper rate limit (q/h_f) during gel injection.

$$q/h_f \approx 3 \times 10^7 w_f \dots\dots\dots(26)$$

In Eq. 26, q/h_f has units of barrels per day per 100 ft of fracture height, while w_f has units of inches. Again, this equation assumes that during gel injection, the pressure gradient can never be lower than that during water injection.

This equation is plotted in Fig. 51 (using y-axis units of bbl/min). The upper rate limit increases linearly with increasing fracture width. Also note that the upper limits are larger than any rate that would practically be encountered in a field application. For fracture widths of 0.001, 0.01, 0.1, and 1 in., the upper rate limits are 21, 210, 2,100, and 21,000 BPM per 100 ft of fracture height, respectively. Even the lowest of these rates are only used during hydraulic fracturing applications. In practical situations, the injection rates are unlikely to approach the limits shown in Fig. 51. Therefore, there appears to be no practical upper rate limit for our generalization that gels should be injected as rapidly as possible to maximize gel penetration along a fracture.

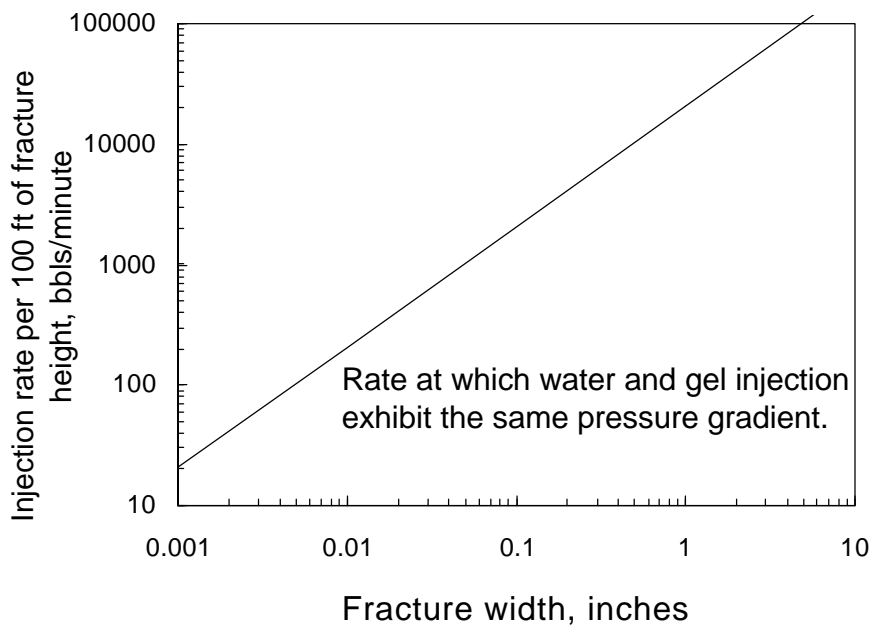


Fig. 51—Upper rate limit for gel injection.

Injection at Low Rates

Two extrusion experiments were performed at the low injection flux of 41.3 ft/d (volumetric rate of 20 cm³/hr). Both experiments used our standard 24-hr-old gel in 48x1.5x0.04-in. fractures (in 48x1.5x1.5-in. 650-mD Berea cores). In the first experiment, gel was injected at 41.3 ft/d into a water-saturated fracture. The pressure drop in the first fracture section (~10 in. long) increased linearly with time to 450 psi during two days of gel injection (Fig. 52). The gel front reached the second fracture section after 1.25 days (13 fracture volumes) of gel injection. Thereafter, the pressure drop in the second fracture section rose to 105 psi. After two days of gel injection, the flood was stopped, and the fracture was opened. Gel had penetrated 1.6 ft along the 4-ft-long fracture. For this gel, the average HPAM and chromium concentrations in the fracture were 47 and 11.5 times more concentrated, respectively, than those in the original gel.

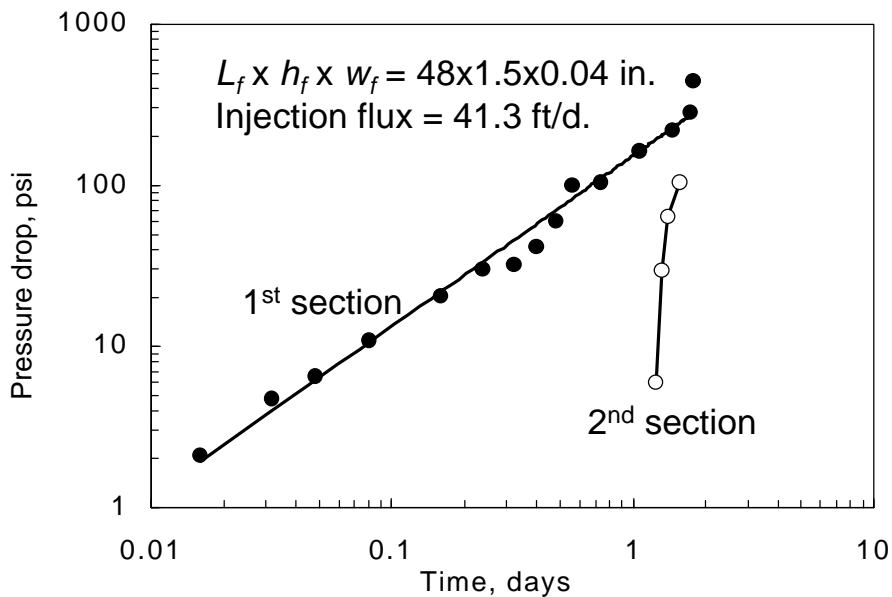


Fig. 52—Pressure drops during the first experiment at 41.3 ft/d.

The second experiment was very similar to the first, except that the fracture was first filled with gel at an injection flux of 4,130 ft/d. Two fracture volumes of gel were required to achieve gel breakthrough. Breakthrough occurred in about three minutes. At this time, the pressure gradient was near 8 psi/ft in all five sections of the 4-ft-long fracture.

Immediately after gel breakthrough, the injection flux was reduced to 41.3 ft/d. The pressure drops across the first two fracture sections are shown in Fig. 53 for the next 15 hours of gel injection. In the first section, the pressure drop steadily increased to 430 psi. In contrast, in the second and subsequent fracture sections, pressure drops decreased to low values—indicating cessation of flow in the fracture. Water leakoff data from this experiment (Fig. 54) were substantially below the values predicted by Eq. 3 (the solid line in Fig. 54). Coupled with the pressure data (Fig. 53), the leakoff data suggest that at 41.3 ft/d, all gel is dehydrated and flow in the fracture comes to a stop within the first fracture section.

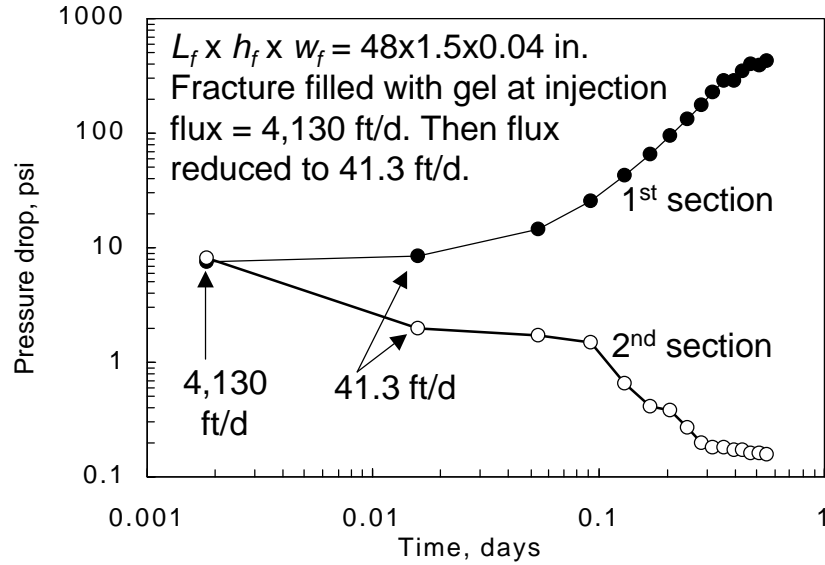


Fig. 53—Pressure drops during the second experiment at 41.3 ft/d.

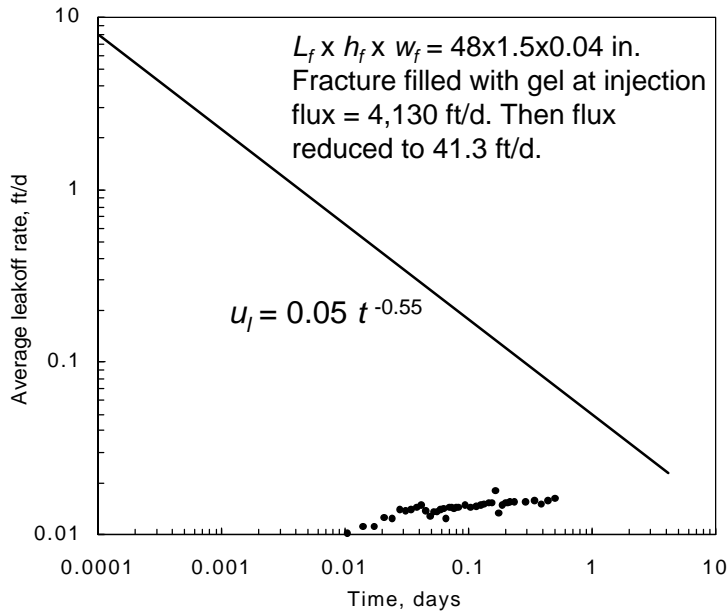


Fig. 54—Water leakoff from gel during the second experiment at 41.3 ft/d.

At the end of the experiment, the fracture was opened, and gel in the fracture was analyzed. Fig. 55 shows the results. Gel concentrations within the first 4 in. averaged 15 times greater than for the original gel. Gel in the subsequent sections was significantly less concentrated (averaging ~2X). This result confirms our suggestion that at 41.3 ft/d, all of the injected gel dehydrated and flow stopped within the first fracture section. This finding implies that in field applications, a concentrated, rigid gel plug can be placed at the beginning of a fracture by simply reducing the injection rate near the end of gel injection.

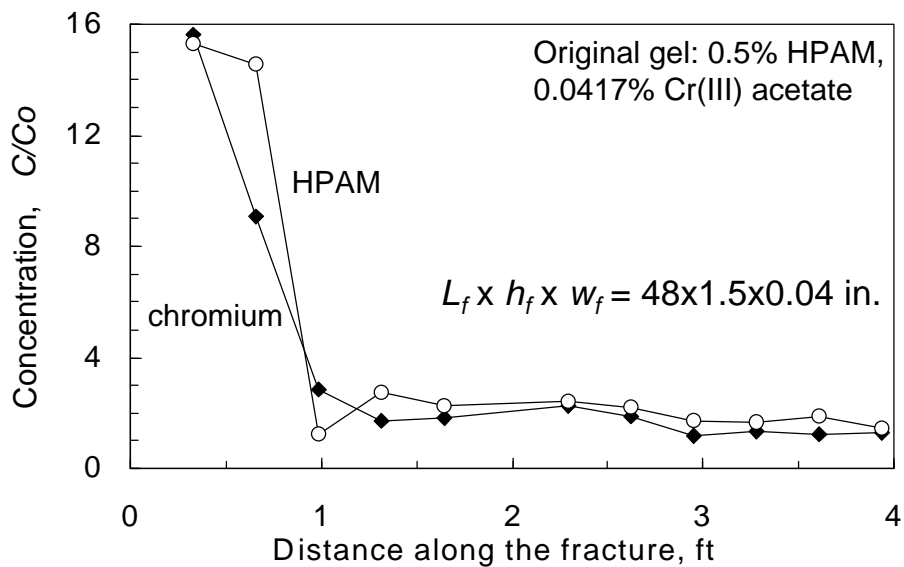


Fig. 55—Gel composition in fracture after gel placement at 41.3 ft/d.

Effect of Polymer Molecular Weight

In the work discussed to this point, the only polymer used was Alcoflood 935 HPAM. The manufacturer (Ciba) stated that this polyacrylamide had a molecular weight between 7 and 9 $\times 10^6$ daltons and a 10% degree of hydrolysis. For comparison, Marathon determined that this polymer had a molecular weight of 5 $\times 10^6$ daltons and a degree of hydrolysis between 5% and 10% (personal communication with R.D. Sydansk).

We wondered whether a gel made with a higher molecular weight polymer could be more cost-effective and/or exhibit more desirable extrusion properties in fractures. To answer this question, we studied a second HPAM polymer, Ciba Percol 338, which Ciba stated had a molecular weight between 12 and 14 $\times 10^6$ daltons and a 10% degree of hydrolysis. A range of formulations was prepared to identify a gel composition that provided behavior similar to that for a gel with 0.5% Alcoflood 935 and 0.0417% Cr(III)-acetate. In all formulations, the ratio of HPAM to Cr(III)-acetate was fixed (at 12:1), the brine used for gelant preparation contained 1% NaCl and 0.1% CaCl₂, and the gel was aged for 24 hours at 41°C. Similarity of behavior was judged by tonguing from a bottle. The most similar gel contained 0.2% Percol 338 HPAM and 0.0167% Cr(III)-acetate.

Five extrusion experiments were performed using gels prepared from Percol 338. Two gels had the composition listed above (i.e., 0.2% HPAM, 0.0167% Cr(III) acetate). Two other gels contained 0.3% HPAM and 0.025% Cr(III) acetate. The fifth gel contained the same concentrations of HPAM and chromium as in our standard gel (i.e., 0.5% HPAM and 0.0417% Cr(III) acetate). All five gels contained 1% NaCl, 0.1% CaCl₂ and were aged 24 hours at 41°C before being extruded through 4-ft-long fractures (48x1.5x0.04 in.) in cores (48x1.5x1.5-in. 650-mD Berea sandstone). For each of the three gel compositions, one experiment was

performed using an injection flux of 33,100 ft/d (volumetric rate was 16,000 cm³/hr) and a gel injection volume of 3.7 liters (~80 fracture volumes). In a fourth experiment, using a gel that contained 0.2% Percol 338, the injection flux was 826 ft/d (volumetric rate of 400 cm³/hr) and ~40 fracture volumes of gel were injected. In the fifth experiment, using a gel that contained 0.3% HPAM, the injection flux was 2,070 ft/d and 80 fracture volumes of gel were injected.

Gel Breakthrough. As expected, gel breakthrough (Table 5) occurred very quickly for the three high-rate floods—between 1 and 2 fracture volumes or between 10 and 20 seconds after the start of the experiment. For the 826-ft/d, 0.2%-HPAM-gel flood, chromium and HPAM were first detected in the fracture effluent after injecting 4 fracture volumes of gel. However, the chromium and HPAM concentrations did not approach the injected concentration until about 13 fracture volumes of gel. Thus, some ambiguity exists about the time at which gel arrived at the end of the fracture in this case. For the 2,070-ft/d, 0.3%-HPAM-gel flood, chromium and HPAM were first detected in the fracture effluent after injecting 1.4 fracture volumes of gel. Overall, the breakthrough trends for the Percol 338 gels were consistent with our observations of the Alcoflood 935 gels. In particular, gel propagation increased and gel dehydration decreased with increased injection rate.

Table 5—Effect of gel composition for Percol 338 gels in 48×1.5×0.04-in. fractures

Polymer used to make gel	Percol 338					Alcoflood 935
	0.2	0.2	0.3	0.3	0.5	
HPAM in gel, %	0.2	0.2	0.3	0.3	0.5	0.5
Chromium in gel, %	0.0167	0.0167	0.025	0.025	0.0417	0.0417
Estimated velocity in the fracture, ft/d	826	33,100	2,070	33,100	33,100	33,100
Fracture volumes of gel injected	40	80	80	80	80	80
Average pressure gradient, psi/ft	4.1	1	1.3	2.7	12	28
Gel front arrival at core end, fracture volumes	4-13	~1	1.4	~1	~1	~1
Average C/C_o in fracture at end of experiment	15	~1	1.5	1.5	4	4

Pressure Gradients. The pressure gradients (Row 6 of Table 5) were significantly less for the gels with Percol 338 than for those with Alcoflood 935. For the gel with 0.5% Percol 338, the pressure gradient in the fracture averaged 12 psi/ft. This value was lower than the average pressure gradient (typically ~28 psi/ft) observed during injection of the low-Mw gel (with 0.5% Alcoflood 935) into a similar fractured core. These results suggest that gels made from polymers with higher molecular weights may be more likely to extrude deep into a fracture system without exceeding wellbore pressure constraints.

Gel Dehydration. Leakoff data from the five experiments are plotted in Fig. 56. For comparison, the solid line in Fig. 56 shows the curve fit for the low-Mw gels from Fig. 10 (or Eq. 3). Leakoff data from two of the five new experiments are described very well using Eq. 3. For these cases,

the similarity of leakoff for low-Mw and high-Mw gels suggests that the two gels may dehydrate and propagate in similar ways.

In contrast, the leakoff data for the three other experiments fell significantly below the trend described by Eq. 3. Additional work is needed to understand these differences. For the high-rate experiment with the 0.2% Percol 338, perhaps the gel was not formed sufficiently well in this case. The composition of this gel is known to be near the edge of the sol-gel transition. In other words, compositions with less HPAM and chromium do not form extended gel structures. Instead, they remain as solutions or suspensions with small gel particles. In support of this idea, we noted that the pressure gradient for gel extrusion was four times less than that for the other 0.2% Percol 338 extrusion experiment (i.e., at 826 ft/d). For the gels with 0.3% Percol 338, the leakoff data also fell below the trend described by Eq. 3. With some imagination, these 0.3%-HPAM data may show a transition from the trend for the 33,100-ft/d, 0.2%-HPAM gel to that for the 0.5%-HPAM gels.

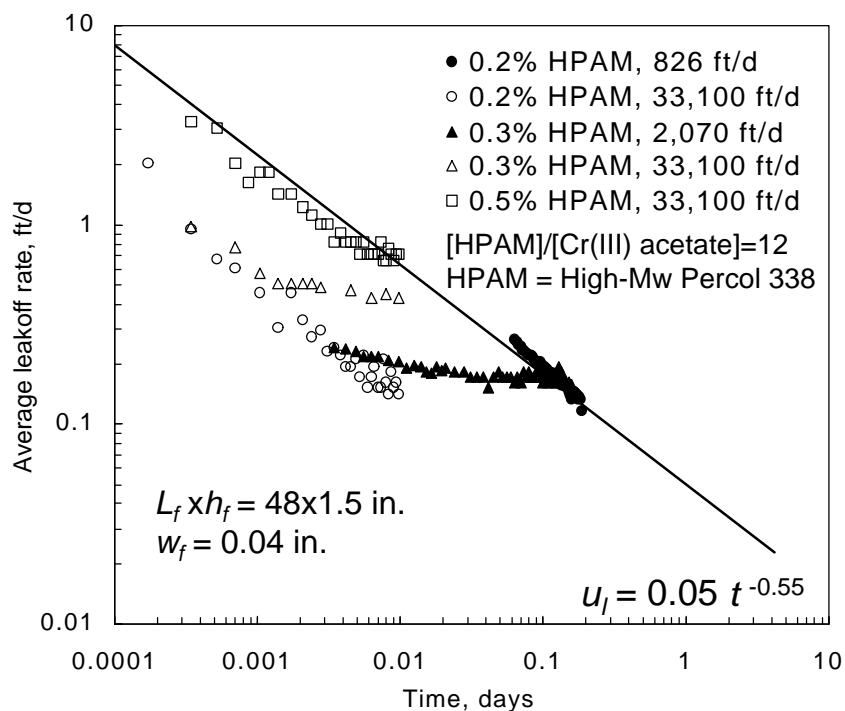


Fig. 56—Average leakoff rates using gel with high-Mw HPAM.

Final Gel Concentrations. At the end of each experiment, the fractures were opened, and the gel in the fracture was analyzed. For the high-rate experiment with 0.2% Percol 338, no concentrated gel was evident in the fracture. This observation supports our suggestion that this gel was not formed satisfactorily for this experiment. For the low-rate experiment with 0.2% Percol 338, the final gel in the fracture was 10-20 times (~15) greater than that for the original gel. For comparison, in previous experiments with the low-Mw (Alcoflood 935) gel, the gel in the fracture after injecting ~40 fracture volumes at similar rates was also from 10 to 20 times more concentrated than the injected gel.

For the gel with 0.5% Percol 338 that was injected at 33,100 ft/d, the chromium and HPAM concentrations for gel in the fracture averaged 3.7 and 4.5 times higher, respectively, than the values in the original gel. For comparison, in a similar experiment with the low-Mw gel, the final gel in the fracture (after 80 fracture volumes) was also 4 times more concentrated than the injected gel (see the last row in Table 5). This similarity in degree of concentration for the low-Mw and high-Mw gels suggests that the two gels dehydrate at roughly the same rate.

For the two experiments with 0.3% Percol 338, analyses of gel in the fracture are shown in Figs. 57 and 58. On average, the gel was concentrated by a factor of 1.5 for both experiments.

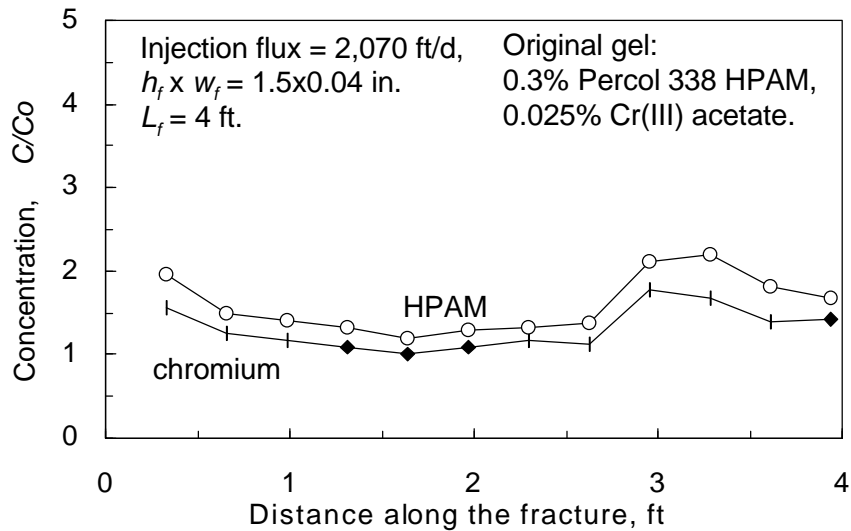


Fig. 57—Gel composition in fracture after gel placement at 2,070 ft/d.

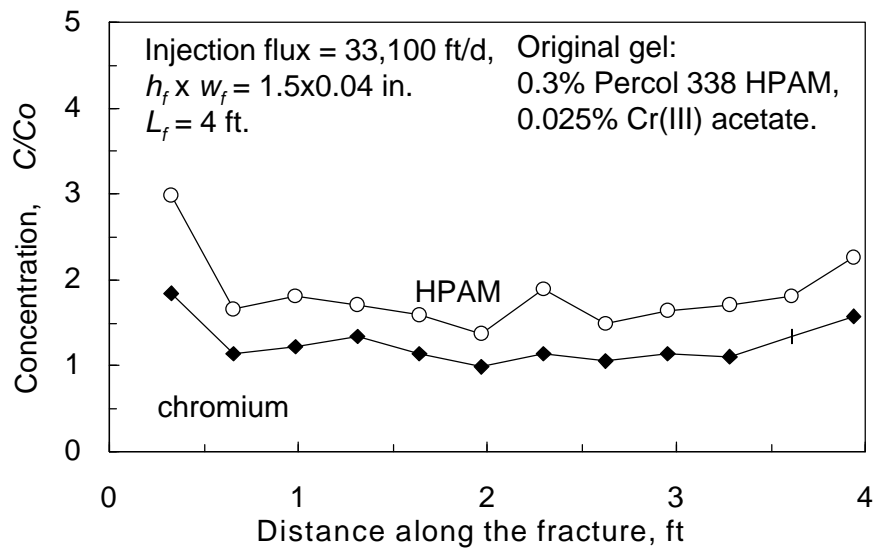


Fig. 58—Gel composition in fracture after gel placement at 33,100 ft/d.

As mentioned previously, the pressure gradients needed to extrude the high-Mw gels through fractures were significantly less than those for low-Mw gels. Thus, gels made from polymers with higher molecular weights may be more likely to extrude deep into a fracture system without exceeding wellbore pressure constraints. This observation may be valuable when treating reservoirs with relatively narrow fractures.

Dual Fracture Floods

In naturally fractured reservoirs, multiple fracture pathways are present. Presumably, the widest fractures are responsible for any severe channeling that may be present. In contrast, the narrower, secondary fractures can benefit hydrocarbon recovery—by distributing injected water in the reservoir to increase oil contact and sweep efficiency and by allowing oil to drain efficiently to the production wells. Ideally, a gel treatment will propagate much farther into the widest, most-conductive fracture(s) than into the narrower fractures. However, the gel will enter the narrower fractures to some extent.

Our laboratory data and analyses can predict how gels distribute between fractures of different widths.¹⁵ To test these predictions, we performed two sets of experiments, with each set containing two fractures that were flooded in parallel. In all cases, the cores were 48x1.5x1.5-in. 650-mD Berea sandstone. In one set, widths of 0.04 in. and 0.08 in. were used for the two fractures, while in the second set, the fracture widths were 0.02 in. and 0.04 in. All “fractures” were made with smooth cuts (i.e., with a rock saw) to insure uniformity of fracture widths. Each core had four internal taps to measure pressures along the fracture during gel injection. In each two-core set, a short (4-in.-long, 0.25-in.-diameter) inlet manifold connected the fracture inlets to the gel source. This manifold and the inlet lines (leading to the fractures) were completely filled with gel before gel injection. Then, 3.7 liters of our standard 24-hr-old Cr(III)-acetate-HPAM gel were injected at a volumetric rate of 2,000 cm³/hr.

First Experiment. In the first experiment, with fracture widths of 0.04 and 0.08 in., gel arrived at the outlet of the 0.08-in.-wide fracture after injecting 120 cm³ (1.3 fracture volumes) of gel. After gel breakthrough, the pressure gradient in the 0.08-in.-wide fracture averaged 4.7 psi/ft. This value was consistent with the trends shown by Fig. 1 and Eq. 1.

Our model of gel propagation predicts that gel propagation along the 0.04-in.-wide fracture should stop when gel breakthrough occurs in the 0.08-in.-wide fracture. This prediction was confirmed by both pressure measurements along the fractures during gel injection and by gel concentrations in the fractures after the experiment. The latter results are shown in Fig. 59. The open symbols in this figure show that the gel only propagated 23 in. into the 0.04-in.-wide fracture. The gel showed a significant concentration gradient—averaging 9X near the fracture inlet and 3X half way through the fracture. In contrast, in the 0.08-in.-wide fracture, the gel was concentrated by a factor around 2.7 throughout the fracture.

After gel breakthrough in the 0.08-in.-wide fracture, the average pressure drop across this core was 18.8 psi (i.e., 4.7 psi/ft x 4 ft). This same pressure drop occurred across the 23-in.-long gel bank in the 0.04-in.-wide fracture. Eq. 1 predicts that the pressure gradient for gel extrusion should be around 12.5 psi/ft in a 0.04-in.-wide fracture. Thus, the predicted distance of

penetration was (18.8 psi)/(12.5 psi/ft) or 1.5 ft. The actual distance of penetration was 1.9 ft (23 in.). Considering the data scatter in Fig. 1, the predicted and actual values matched fairly well.

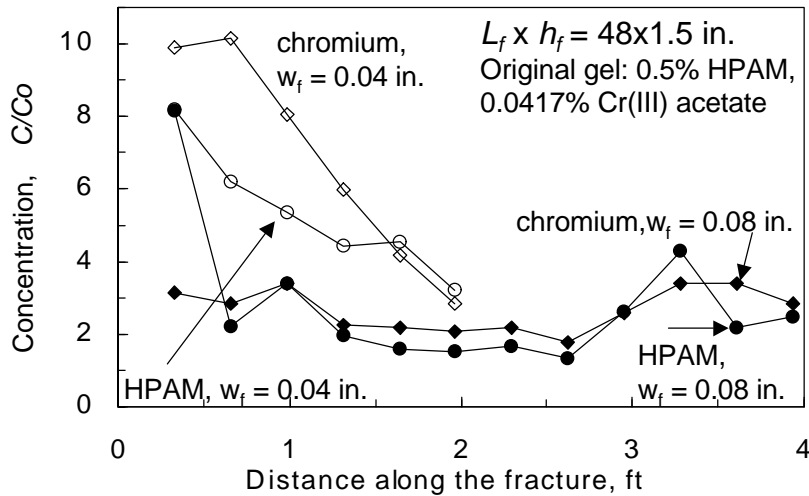


Fig. 59—Gel compositions in fractures after the first dual fracture flood.

The solid circles in Fig. 60 show leakoff data for the 0.04-in.-wide fracture during the experiment. For comparison, the solid line illustrates predictions from Model 2 (Eq. 3). The data points fell below the values predicted by Model 2, and the deviations appeared to increase with time. Our results suggest that after the gel front stopped moving, fresh gel could still wormhole into the gel bank for some time because water leakoff (i.e., gel dehydration) created room within the gel bank in the fracture. However, as time passed and the gel concentrated, fresh gel became less able to penetrate (wormhole) very deeply into the gel bank. Thus, the region of significant leakoff moved increasingly upstream in the gel bank, gel concentrations in the upstream parts of the bank increased, and the overall leakoff rate (averaged over the entire gel bank) decreased.

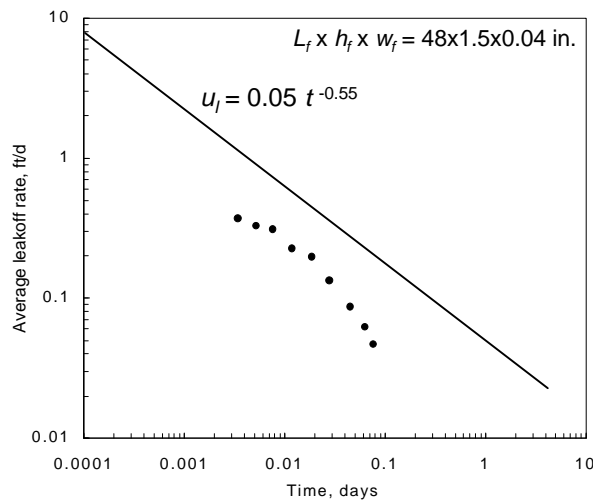


Fig. 60—Leakoff rates from the narrow fracture during the first dual fracture flood.

Second Experiment. In the second experiment, with fracture widths of 0.02 and 0.04 in., gel arrived at the outlet of the 0.04-in.-wide fracture after injecting 74 cm^3 (1.6 fracture volumes) of gel. After gel breakthrough, the pressure gradient in the 0.04-in.-wide fracture averaged 13.1 psi/ft. This value was very close to the value predicted from Eq. 1 (12.5 psi/ft).

As in our first experiment, gel propagation along the narrow fracture stopped when gel broke through in the wider fracture. Gel concentrations in the fractures after the experiment are shown in Fig. 61. The open symbols in this figure show that the gel only propagated 8 in. into the 0.02-in.-wide fracture. Again, the gel in the narrow fracture showed a significant concentration gradient—averaging 14X near the fracture inlet and 9X at 8 in. into the fracture. For comparison, in the 0.04-in.-wide fracture, the gel was concentrated by an average factor of 4.6 and did not vary greatly through the fracture.

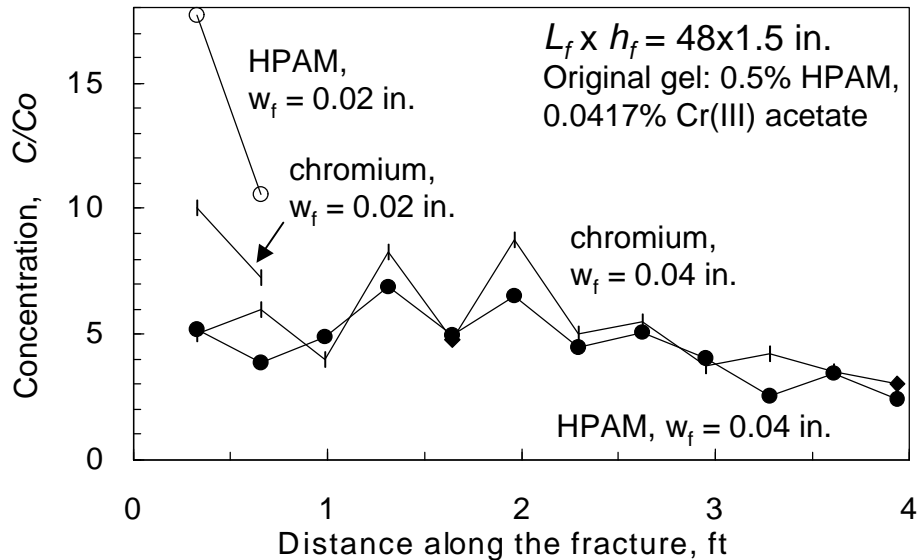


Fig. 61—Gel compositions in fractures after the second dual fracture flood.

Again, we applied Eq. 1 to predict the distance of gel penetration into the 0.02-in.-wide fracture. After gel breakthrough in the 0.04-in.-wide fracture, the average pressure drop across this core was 52.4 psi (i.e., 13.1 psi/ft x 4 ft). This same pressure drop occurred across the 8-in.-long gel bank in the 0.02-in.-wide fracture. Eq. 1 predicts that the pressure gradient for gel extrusion should be around 50 psi/ft in a 0.02-in.-wide fracture. Thus, the predicted distance of penetration was (52.4 psi)/(50 psi/ft) or 1 ft. The actual distance of penetration was 0.7 ft (8 in.). As with the first experiment, considering the data scatter in Fig. 1, the predicted value matched the actual value reasonably well.

The solid circles in Fig. 62 show leakoff data for the 0.02-in.-wide fracture during the experiment. For comparison, the solid line illustrates predictions from Model 2 (Eq. 3). As was noted in the first experiment (Fig. 60), the data points fell below the values predicted by Model 2, and the deviations increased with time.

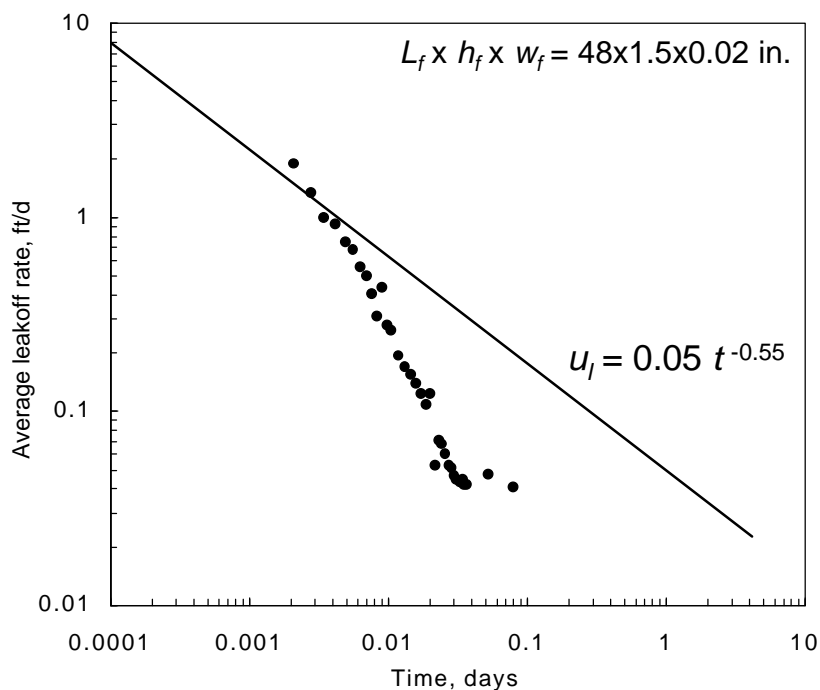


Fig. 62—Leakoff rates from the narrow fracture during the second dual fracture flood.

In summary, in both sets of dual fracture experiments, the distances of gel penetration into the narrow fractures of a given set were reasonably close to the predicted values.

Effect of Temperature—Preliminary Study

Our experiments to date were performed at 41°C. Of course, many reservoirs and field applications exist at other (mostly higher) temperatures. Therefore, a need exists to determine gel extrusion and dehydration properties at other temperatures. This section describes our first experiment in this new direction. In particular, an extrusion experiment was performed at 60°C (140°F). The core, again, was 48x1.5x1.5-in. 650-mD Berea sandstone, and the fracture width was 0.04 in. Pressure taps along the fracture divided the core into five sections of equal length. Effluent from the fracture and matrix were collected separately. We used our standard Cr(III)-acetate-HPAM gel (0.5% Alcoflood 935 HPAM, 0.0417% Cr(III) acetate) that was aged for 24 hours at 41°C before injection. The fractured core was equilibrated at 60°C well before gel injection started. During gel injection, the rate was fixed at 2,000 cm³/hr—translating to a flux in the fracture of 4,130 ft/d. Before entering the fracture, the gel passed through a heat exchanger (53 cm³ holdup volume, 1.8-cm-diameter flow path) to raise the gel temperature to 60°C. Gel temperatures were measured inline both at the fracture inlet and exit to ensure that 60°C was reached and maintained. The heat exchanger and inlet flow lines were filled with gel to the fracture inlet before beginning the experiment. The total gel volume injected was 3.7 liters (80 fracture volumes). At 2,000-cm³/hr, the average time for gel transit through the heat exchanger was 1.6 minutes.

Gel Propagation. Gel arrived at the end of the 4-ft-long fracture after 1.5 fracture volumes (69 cm^3). By monitoring pressures along the fractures, propagation of the gel front could be followed in the five sections of the fracture. The solid circles in Fig. 63 plot the times required for the gel front to reach various positions along the fracture. The solid line shows predictions from Model 2. Except at the early times and distances, Model 2 under-predicted the rates of propagation.

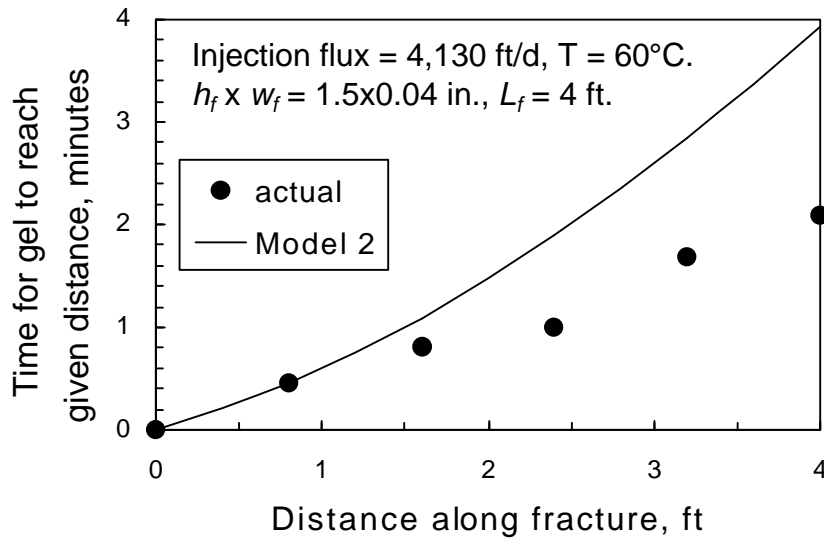


Fig. 63—Gel propagation at 4,130 ft/d in a 48x1.5x0.04-in. fracture at 60°C.

Leakoff. The leakoff results after gel breakthrough are plotted in Fig. 64. The leakoff values generally fell below the predictions from Eq. 3 (solid line in Fig. 64). This result is consistent with Fig. 63 in that lower rates of gel dehydration are tied to more rapid rates of gel propagation. Of course, more work is needed to verify and extend these results—especially at other flow rates, flow times, and temperatures.

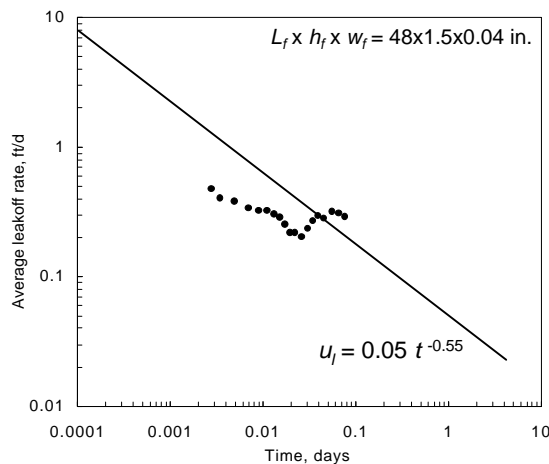


Fig. 64—Leakoff during gel injection at 4,130 ft/d in a 48x1.5x0.04-in. fracture at 60°C.

Pressure Gradients. After gel breakthrough, pressure gradients along the fracture averaged 1.7 psi/ft, with similar values observed in all five sections of the fracture. This value is seven times less than the value from Eq. 1 (and Fig. 1) for 0.04-in.-wide fractures. Thus, results from this first experiment indicate that the pressure gradient for gel extrusion decreases substantially with increased temperature. For comparison, the viscosity of water only decreases by 27% between 41°C and 60°C.

Conclusions

The following conclusions apply to 24-hr-old Cr(III)-acetate-HPAM gels during extrusion through fractured cores at 41°C:

1. Dehydration reduces the rate of gel propagation through fractures.
2. For $w_f=0.04$ -in., $L_f=0.5$ to 16 ft, $h_f=1.5$ to 12 in., and injection fluxes from 129 to 33,100 ft/d, the average rate of gel dehydration and leakoff (u_l , in ft/d or ft³/ft²/d) was described well using: $u_l = 0.05 t^{-0.55}$, where t is time in days.
3. For $w_f=0.08$ -in., $L_f=4$ to 32 ft, $h_f=1.5$ -in., and injection fluxes from 207 to 16,500 ft/d, $u_l \approx 0.05 t^{-0.55}$.
4. For $w_f=0.02$ to 0.16-in., $L_f=4$ ft, $h_f=1.5$ -in., and an injection rate of 16,000 cm³/hr, $u_l \approx 0.05 t^{-0.55}$.
5. For gels with 0.5% of either Alcoflood 935 or Percol 338, $u_l = 0.05 t^{-0.55}$.
6. For conditions examined to date during gel extrusion, dp/dl was insensitive to injection rate (for fractures of a given width).
7. To maximize gel penetration along fractures, the highest practical injection rate should be used.
8. In wide fractures, gel dehydration may be desirable to form rigid gels that are less likely to washout after placement. In these applications, reduced injection rates may be appropriate.
9. In single, wide fractures where short distances of penetration are needed, the gel volume required increases roughly with the distance of penetration.
10. In single fractures with narrow to moderate widths, the required gel volume increases roughly with the distance of penetration raised to the 1.5 power.
11. Increasing HPAM molecular weight by ~2X may reduce the pressure gradient required for gel extrusion.
12. Preliminary results suggest that the pressure gradient for gel extrusion decreases dramatically between 41°C and 60°C. Gel dehydration was generally less at 60°C than at 41°C.

Future Work

Several areas for additional work remain. In particular, we plan to address the following questions during our future work.

1. Why does, $u_l = 0.05 t^{-0.55}$?
2. Why does, $dp/dl = 0.02/(w_f)^2$?
3. How do gel propagation and dehydration vary with gel composition?
4. How do gel propagation and dehydration vary with gel age?
5. How do gel propagation and dehydration vary with temperature?
6. How will gels distribute in naturally fractured reservoirs?
7. How should gel treatments be sized in naturally fractured reservoirs?

3. FIELD APPLICATION OF GEL PROPAGATION RESULTS

In this chapter, we examine the relation between field and laboratory results. Three important points will become evident from this discussion. First, simple calculations can give at least a rudimentary indication of the width of the fracture that causes the excess water production. For the case of vertical fractures or faults that cross horizontal production wells, these calculations can also give an idea of how far the gel should penetrate to provide a beneficial effect. Using laboratory data coupled with field data collected before, during, and after gel injection, the calculations can also give an indication of how far the gel has actually penetrated into the fracture.

Second, this analysis points out areas where additional laboratory work is needed to aid in the design of field applications. In particular, a need exists for determination of gel extrusion properties at higher temperatures—at least up to 100°C. Also, a need exists to determine gel extrusion properties for gels over a range of concentrations, e.g., for polymer concentrations from 0.3% to 1.5%.

Third, our analysis reveals critical measurements that should be made during field applications. In particular, accurate flowing and static downhole pressures should be made at least before and after the gel treatment is applied. Some very useful insights can be gained if downhole pressures are measured during gel injection.

Field Example

In Ref. 6, Lane and Sanders described a gel treatment to reduce water production from a near-horizontal production well that was intersected by a fault. The well was located near the periphery of the field, where total pay thickness of the ~50 – 100-mD sandstone was <50 ft and formation temperature was ~90°C (195°F). Reservoir pressure at the time of the gel treatment was ~3,200 psi. Analyses revealed that water from the underlying Sadlerochit aquifer channeled through the fault to reach the wellbore near 11,338 ft measured depth. The completion was a cased and cemented liner that was nearly horizontal (85°) through the pay zone. The well was terminated at 11,853 ft measured depth (9,009 ft true vertical depth). Table 6 describes oil and water production rates and pressure drawdowns before and at various times after the gel treatment, while Table 7 lists the compositions, wellhead pressures, and volumes during gel injection.

Table 6—Production well data before and after gel treatment (from Refs. 6 and 16)

Time	Oil rate, BOPD	Water rate, BWPD	Pressure drawdown, psi	Oil productivity index, BOPD/psi	Water productivity index, BWPD/psi
Pre-job	466	4,290	1,455	0.32	2.95
Post-job	543	1,700	2,280	0.24	0.74
1 mo	727	1,895	2,430	0.30	0.78
1 yr	665	2,175		-	-
1.5 yr	567	2,410		-	-

Table 7—Compositions, pressures, and volumes of injected gels (from Refs. 6 and 16)

HPAM content, wt %	Cr(III)-acetate content, wt%	Wellhead injection pressure, psi	Volume injected, bbls	Comment
0.30	0	400 – 0	22	preflush
0.30	0.025	0 - 250	2,045	
0.45	0.038	225 - 525	5,500	
0.60	0.050	500 - 675	3,225	
0.90	0.075	725 - 800	740	
0.30	0	800	100	overflush

Pump rate: 2 BPM throughout

Roughly 12,000 bbls of Cr(III)-acetate-HPAM gel were injected using a rate of 2 BPM. For a given pressure listing (third column) in Table 7, the two values indicate the pressures at the beginning and end of a given phase of gel injection. Refs. 6 and 16 describe and analyze the treatment (and others) and reveal that the gel treatment was very successful in reducing water production, while maintaining oil productivity (e.g., see Table 6). Here, we will discuss some simple calculations that may aid future treatment designs.

Fracture Characterization before the Treatment

Using the Darcy equation for radial flow, one can often confirm that a fracture (or fault) is, or is not, the cause of excess water production.² Eq. 27 provides the simplest form of this equation.

$$q/Dp = \Sigma k h / [m \ln (r_e / r_w)] \dots\dots\dots(27)$$

If the actual productivity index (i.e., the left side of Eq. 27) is less than or equal to the right side of Eq. 27, then a fracture or fault may not be the cause of the water problem. However, if the left side of Eq. 27 is significantly greater than the right side, then a linear-flow feature (e.g., a fracture) probably does cause the problem.² When using this equation, several points should be noted. First, the production rate, *q*, should include all significant fluid contributions (i.e., water, oil, and gas). Second, the downhole pressure drop, *Dp*, (the average reservoir pressure in the vicinity of the well minus the pressure in the wellbore) must be accurate and current. Third, the permeability(s) used in Eq. 27 must be from logs, core analyses, or pressure-transient data—not from production data.

In our field example,⁶ before the gel treatment was applied, the total production rate was 4,756 BPD (466 BOPD + 4,290 BWPD), the pressure drawdown, *Dp*, was 1,455 psi (Table 6), and water viscosity, *m* at reservoir temperature was about 0.3 cp. (Since water dominates fluid production, we can neglect the viscosity contribution from oil). Since most of the measured production came from within an 18-ft interval, *h* in Eq. 27 will be given this value. The formation permeability, *k*, was on the order of 100-mD (from core analyses). However, if both water and oil flow radially into the wellbore from the matrix, a high-fractional water flow and water saturation exist (from Table 6). This assumption suggests that the oil saturation was near the irreducible level, so the effective permeability to water may be closer to 10 mD than to 100 mD. Thus, a permeability of 10-mD is used in Eq. 27. The natural log term in Eq. 27 commonly

has a value of 6 or 7. Inputting these values into Eq. 27 (using the appropriate conversion factors) reveals that the actual productivity index, q/Dp , was at least 5 times greater than that calculated from the right side of Eq. 27. This result confirms that a fracture (or more correctly, a fault in this case) caused the problem.

Eq. 27 can also be used to estimate the width and conductivity of the fault. In this case, we assume that all water production flows through the fault, and fracture conductivity, $k_f w_f$, is substituted for Σkh in Eq. 27. Using the parameters from the previous paragraph, fracture conductivity was estimated to be 620 darcy-ft. This conductivity can then be converted to an effective average fracture width using Eq. 28 (taken from Ref. 15).

$$w_f = 5.03 \times 10^{-4} (k_f w_f)^{1/3}, \dots\dots\dots(28)$$

where $k_f w_f$ has units of darcy-ft and w_f has units of ft. Eq. 28 estimates that the fault has a width of 0.051 inches.

How Far into the Fault Should the Gel Penetrate?

If the water production problem is caused by a single fracture or fault that intersects the horizontal wellbore, the distance of gel penetration into the fracture does not need to be particularly large.¹⁷ In this case, the benefit gained varies approximately logarithmically with the distance of gel penetration. This point is illustrated in Fig. 65. The y-axis in this figure plots the productivity of the well relative to the productivity for the case where no fracture or fault is present. In other words, the y-value indicates the excess water contribution from the fault as a function of the radial distance of gel penetration into the fault (x-axis). In this example, if the fault is present and no gel treatment is applied, the well productivity is seven times greater than the case where no fault exists. Unfortunately, the extra well productivity comes only in the form of a large amount of water that channels through the fault from the aquifer. If the gel penetrates 400 ft into the fault, the well productivity is about the same as the case where no fault exists.

Fig. 65 reveals that most of the benefit from the gel treatment is achieved with relatively short distances of penetration. The well’s water productivity is cut in half by only 3 ft of gel penetration and is reduced by about 75% with 20 ft of gel penetration. Thus, large-volume treatments may not be needed in this case. However, we must emphasize that this conclusion is specific to the particular scenario that we describe—i.e., a single fault or fracture intersecting a horizontal well. The conclusion may not be valid for vertical wells or if multiple fractures or faults intersect a horizontal well, or if a natural fracture system is present. Furthermore, even for the case of a single fault or fracture that intersects a horizontal well, some value may be realized by injecting a significant amount of gel to mitigate the possibility of gel washout after the well is returned to production. In the particular field example under discussion, no gel washout was observed.⁶

Was the Injected Material a Gel or a Gelant?

After the gel formulation was mixed and injected at 2 BPM, approximately 2 hours were required for the gelant to travel from the wellhead to the treated zone (225 bbl). Considering the high downhole temperature (~90°C at the start of gel injection) and the gelation times for these

gels (a few hours at low temperatures; around 10 minutes at 90°C), we believe that the formulation existed as a gel (rather than as a fluid gelant solution) at the time it entered the fault.

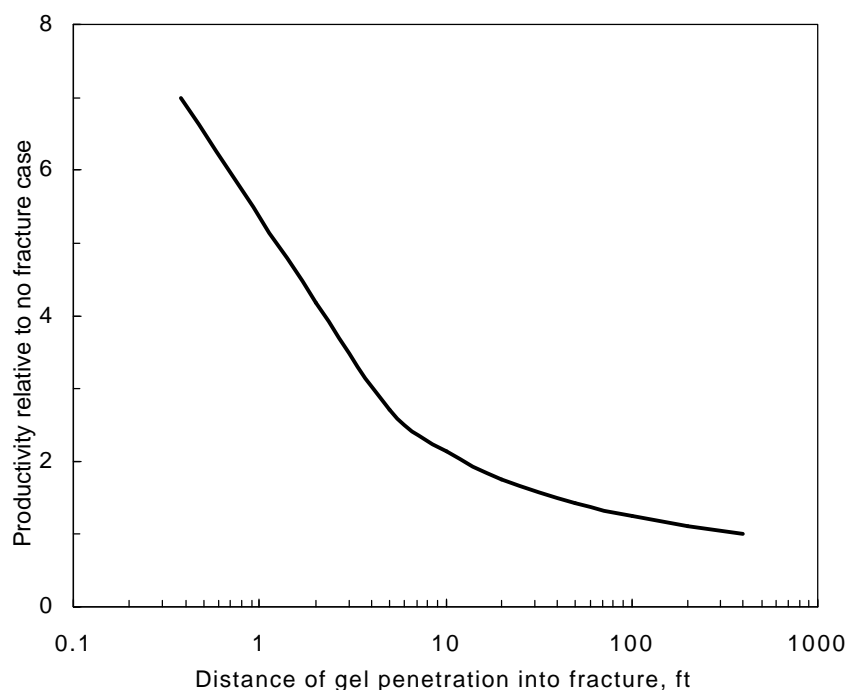


Fig. 65—Effect of gel propagation on fault plugging.¹⁶

How Far Did the Gel Penetrate?

Two methods exist that allow us to estimate how far gel actually penetrated into the fault in the field application. Both methods rely on laboratory and field measurements. As will be seen, our application of these methods reveal a need for accurate measurements of pressure drawdowns in field applications and for laboratory measurement of gel-extrusion properties over a wider range of temperatures and gel compositions.

The first method is based on Fig. 1. This method requires knowledge of the downhole pressure drops during gel injection, the width of the fracture or fault, and the pressure gradient required to extrude the gel through a fracture of the given width. In our field example, we estimated the fault width to be 0.051 inches (discussed above). From Eq. 1, the pressure gradient during gel extrusion should be around 7 psi/ft if the gel contained 0.5% Alcoflood 935 HPAM and 0.0417% Cr(III)-acetate and the fracture temperature was 41°C. In reality, the reservoir temperature was around 90°C and a range of gel compositions were injected—with gels containing from 0.3% to 0.9% HPAM. (See Table 7. The polymer used and the relative Cr(III)-acetate concentrations were similar to those used in the laboratory experiments.) In the absence of gel extrusion data at 90°C and at other compositions, we must use existing data and appreciate the errors that may be introduced.

Assuming that the pressure gradient for gel extrusion is 7 psi/ft, the distance of gel penetration into the fault can be estimated from the downhole pressure drops. At the start of injection of the

0.45%-HPAM gel, the downhole pressure drop was estimated to be 946 psi. This value derives from the measured wellhead pressure of 225 psi (Table 7), a calculated pressure difference from the wellhead to the downhole well location (3,921 psi), and an estimated reservoir pressure of 3,200 psi. By dividing 946 psi by 7 psi/ft, the position of the gel front is estimated at 135 ft from the wellbore. At this time, injection of 2,045 bbl of 0.3%-HPAM gel was just completed, and injection of 5,500 bbl of 0.45%-HPAM gel had just started. One could argue that the extrusion properties of 0.3%-HPAM gel would be more appropriate as input for this calculation. Also, the calculation would be more reliable if a current, accurate downhole pressure drop was available in place of the estimated numbers. Again, these observations emphasize the importance of accurate downhole pressure measurements and of additional laboratory measurement of gel extrusion properties.

At the end of injection of the 0.45%-HPAM gel, the downhole pressure drop was estimated to be 1,246 psi. This value derives from the measured wellhead pressure of 525 psi (Table 7) in the same manner described above. By dividing 1,246 psi by 7 psi/ft, the position of the gel front is estimated at 178 ft from the wellbore. Thus, the method suggests that injecting 5,500 bbl of gel advanced the gel front by 32% (i.e., from 135 to 178 ft from the wellbore).

A second method can be used to estimate gel propagation. This method is based on Figs. 42 and 43. It assumes that gel dehydration dominates the rate of gel propagation so that the volume (V) of gel required to advance the gel front by a given distance is proportional to the 1.5 power of the new fracture area that is contacted by gel. For linear flow (e.g., a vertical well that is cut by a vertical fracture), this relation is given by Eq. 29:

$$V_2 / V_1 = (L_2 / L_1)^{1.5}, \dots\dots\dots(29)$$

Where V_2 represents the total volume of gel injected to reach a distance, L_2 , of gel penetration into the fracture. For radial flow (e.g., a horizontal well that is cut by a vertical fracture or fault), this relation is given by Eq. 30:

$$V_2 / V_1 = [(r_2 / r_1)^2]^{1.5}, \dots\dots\dots(30)$$

where V_2 represents the total volume of gel injected to reach a radius, r_2 , of gel penetration into the fracture. Given values of 2,045 bbl, 7,545 bbl, and 135 ft for the parameters, V_1 , V_2 , and r_1 , respectively, Eq. 30 estimates the radius of gel penetration to be 209 ft after injecting the 0.45%-HPAM gel bank. Thus, this method suggests that injecting 5,500 bbl of gel advanced the gel front by 55%, compared with 32% for the first method. Perhaps, the two methods would have been in closer agreement if more accurate gel extrusion properties and downhole pressures were available.

How Effectively Did Gel Seal the Fault?

Earlier, we used Eq. 27 to estimate the conductivity of the fault before gel injection (620 darcy-ft). The same equation can be used to estimate fault conductivity after the gel treatment. One month after the treatment, the well produced 1,895 BWPD and 727 BOPD with a pressure drawdown of 2,430 psi. Assuming that all 1,895 BWPD were produced from the fault after the treatment, fault conductivity is calculated to be 180 darcy-ft. This result suggests that the fault

conductivity was reduced 71% by the gel treatment—thus the treatment did not completely seal the fault. However, the calculation may be somewhat conservative. Consider the case where before the treatment, none of the oil was produced from the fault; however, some water was produced from portions of the well other than those associated with the fault. To justify this possibility, the spinner tool used to measure flow profiles before the treatment probably could not accurately detect differences less than 10%-15% of the total flow. Thus, the 466 BOPD and an equal volume of water could have entered the well somewhere other than at the fault. In that case, the conductivity of the fault may have been reduced by 80% by the gel treatment. Of course, more accurate profile logs could help resolve this issue.

Table 6 reveals that immediately after the gel treatment, the oil productivity index was reduced from 0.32 to 0.24 BOPD/psi. However, one month after the treatment, the oil productivity index rose to 0.3 BOPD/psi. Thus, the treatment reduced water productivity index much more than that for oil. This fact provides further evidence that the oil was not produced through the fault.

Conclusions

1. Simple calculations can give at least a rudimentary indication of the width of the fracture or fault that causes excess water production. For the case of vertical fractures or faults that cross horizontal production wells, these calculations can also give an idea of how far gel should penetrate to provide a beneficial effect. Using laboratory data coupled with field data collected before, during, and after gel injection, the calculations can also give an indication of how far the gel has actually penetrated into the fracture.
2. Our analyses point out areas where additional laboratory work is needed to aid in the design of field applications. In particular, a need exists for determination of gel extrusion properties at higher temperatures—at least up to 100°C. Also, a need exists to determine gel extrusion properties for gels over a range of concentrations, e.g., for polymer concentrations from 0.3% to 1.5%.
3. Our analyses reveal critical measurements that should be made during field applications. In particular, accurate flowing and static downhole pressures should be made at least before and after the gel treatment is applied. Some very useful insights can also be gained if downhole pressures are measured during gel injection.

4. DISPROPORTIONATE PERMEABILITY REDUCTION

Imaging Experiments Using Synchrotron X-Ray Microtomography

We performed imaging experiments using high-resolution computed microtomography (CMT) to compare the oil and water pathways and fluid distributions before and after gel treatment. The imaging experiments were performed in collaboration with ExxonMobil Research & Engineering Company at the National Synchrotron Light Source (NSLS) at Brookhaven National Laboratory. The objective was to study the disproportionate permeability reduction on a microscopic scale.

Previously, we used NMR imaging to observe disproportionate permeability reduction on a microscopic scale.¹⁸ Results from these experiments revealed that the imaging technique had many limitations that prevented us from obtaining reliable pore-level images. Most importantly, the spatial resolution was on the order of hundreds of micrometers, which was too low to clearly distinguish fluid pathways on the pore level. Recent advancements in computed microtomography using synchrotron X-ray sources provides the ability to obtain three-dimensional pore-level images of rock samples with a spatial resolution on the order of micrometers.¹⁹ This technology has been available at the National Synchrotron Light Source for many years. Recent improvements in data acquisition, transmission, and reconstruction have reduced the time required to produce 3-D pore-level images to a few hours, which is a fraction of the time required for previous scanning methods.

Fig. 66 shows a schematic of the CMT apparatus. To produce an image slice, X-rays transmitted through the sample are recorded on a linear array of detectors. The sample is rotated by a discrete angular interval determined by the linear resolution desired. The procedure is repeated for each angular view until the sample has been rotated by 180° in the X-ray beam. The data collected during the process are then used to reconstruct the horizontal slice. The CCD camera is capable of reconstructing 1,000 horizontal slices simultaneously. Instead of detecting X-ray transmission directly, which limits the spatial resolution to the detector size, a thin high-resolution scintillator placed behind the sample converts each X-ray attenuation map to a visible image, which is then magnified and re-imaged with conventional optics onto the cooled CCD area array.

Imaging Experiments Using a Water-Based Gel. The core (high-permeability Berea sandstone) was 6.5 mm in diameter and 30 mm in length with an intermediate pressure tap 6 mm from the inlet face (Fig. 67). Due to computer memory and time constraints, we focused our scan in a segment of the core that was 6.5 mm in diameter and 3.25 mm in length. To avoid end effects, the scanned segment was located about half way between the inlet and outlet faces (Fig. 67). The gel was our standard Cr(III)-acetate-HPAM (0.5% Alcoflood 935 HPAM, 0.0417% Cr(III) acetate). Hexadecane was the oil phase. To increase the image contrast between the brine and the oil phases, hexadecane was doped with 10% w/w iodohexadecane. All experiments were performed at room temperature. To digitally compare the images before and after gel placement, oil, water, and gelant flooding were performed without ever removing the core from the sample stand. In total, we performed six 3-D scans with an image resolution of 10 μm at different stages of the oil-water experiment. During the imaging experiments, we first scanned the core when it was saturated only with brine. Next, the core was scanned at residual water saturation and residual oil saturation before gelant injection. After gel placement, the core shut in for twelve hours (at ~60°C) and then scanned.

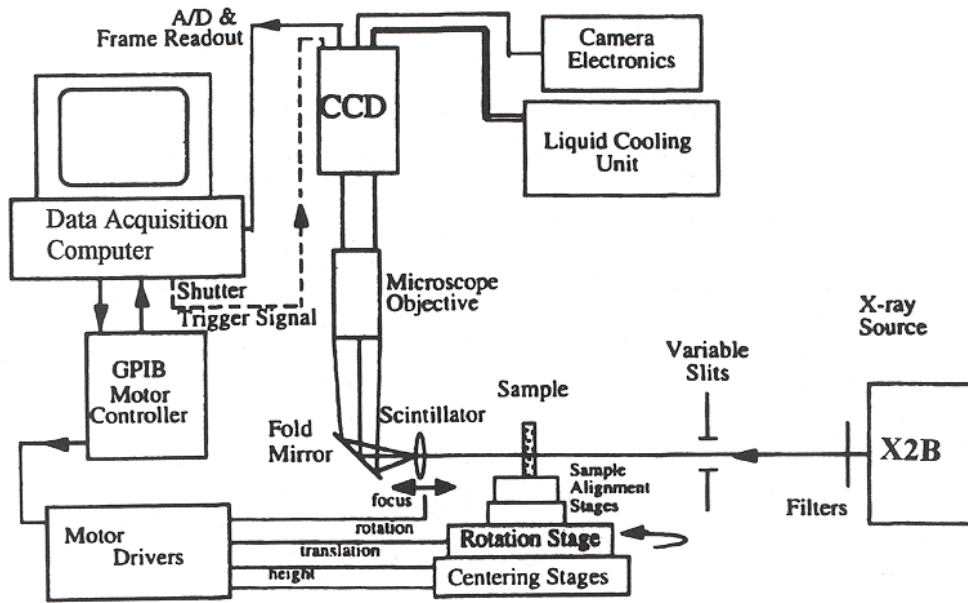


Fig. 66—Schematic of X-ray Synchrotron Microtomography apparatus.

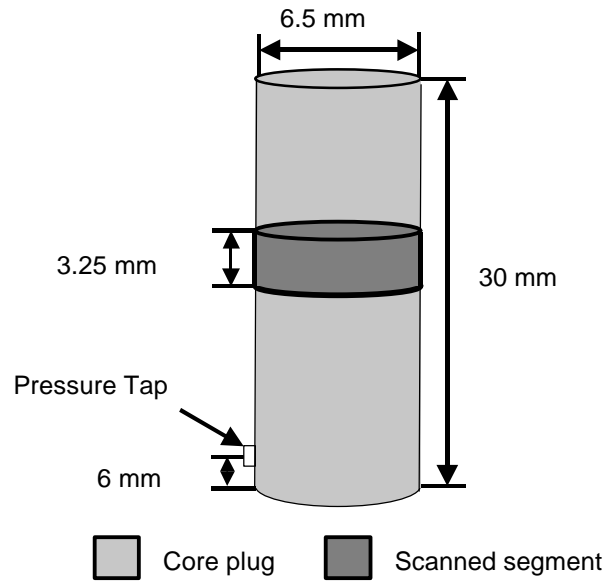


Fig. 67—Berea core plug used in X-ray Synchrotron Microtomography

Next, oil was injected into the core to measure the oil residual resistance factor, F_{rro} . The core was scanned again after oil injection to visualize the oil pathways after gel. Next, brine was injected to measure the water residual resistance factor, F_{rrw} . Finally the core was scanned after brine injection to visualize the water pathways after gel. Table 8 shows that the gel reduced the permeability to water 81 times more than that to oil ($F_{rrw}/F_{rro}=81$).

Table 8—Summary of residual resistance factors: Water-based gel
 Core: strongly water-wet Berea
 Gel: 0.5% HPAM, 0.0417% Cr(III)-acetate, 1% NaCl, 0.1% CaCl₂

k_w , mD	F_{rrw}	F_{rro}	F_{rrw}/F_{rro}
700	1,220	15	81

As shown in Fig. 68, the image was cropped into a rectangular block of 4.6 mm×4.6 mm×3.25 mm to eliminate the artifacts created by a thin layer of epoxy coating on the surface of the core. Fig. 69 is a 3-dimensional view of the rectangular block. As illustrated in Fig. 69, the CMT has high enough resolution to clearly distinguish rock grains from pore space. Also, this technology is non-destructive and therefore can be used to monitor changes in fluid saturation and distribution at different stages of coreflood experiments. Software tools are available to digitally quantify the pore size distribution and fluid saturations from the images generated by the CMT. Also available are software tools that can reconstruct fluid pathways. We will report results from the digital image analysis in the near future.

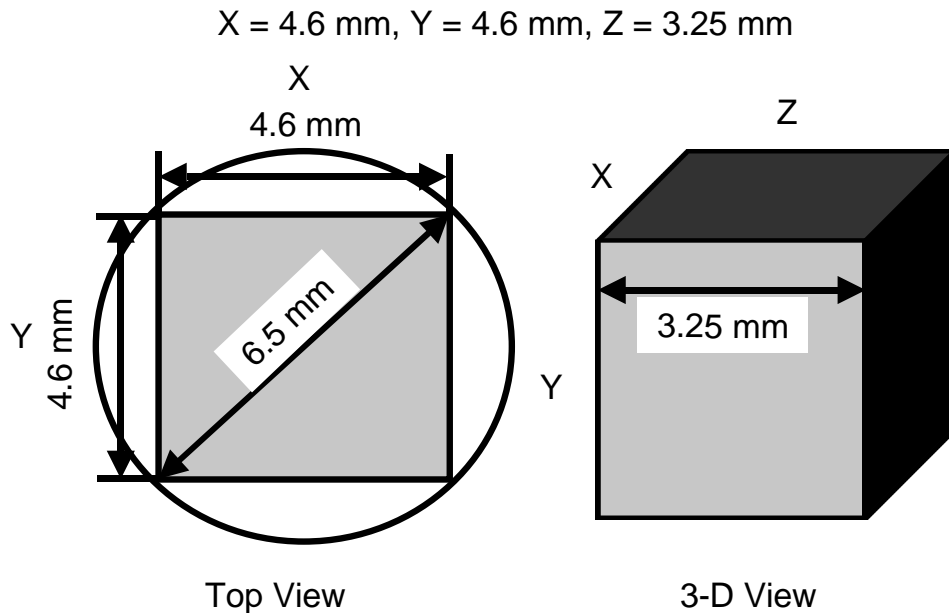


Fig. 68—Dimensions of the cropped image block.

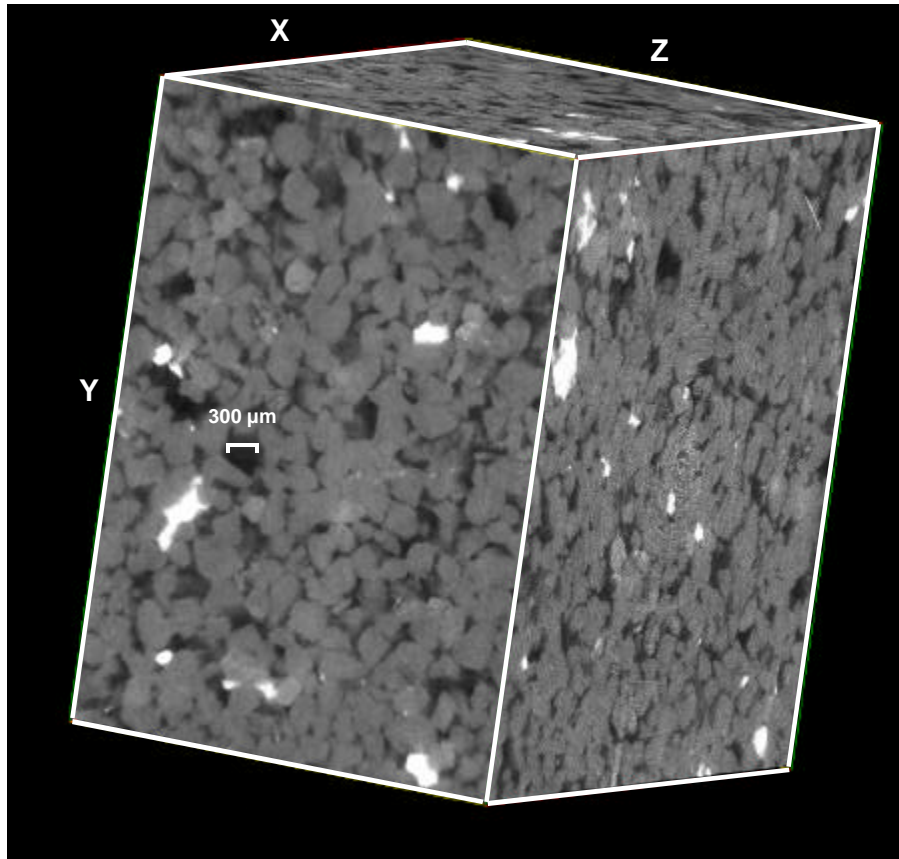


Fig. 69—3-D image of the Berea core plug with an image resolution of 10 μm ($X=4.6\text{ mm}$, $Y=4.6\text{ mm}$, $Z= 3.25\text{mm}$).

Since it is difficult to see through the 3-D structure, we focus on thin slabs that are parallel to the X - Y plane (Fig. 70). The direction of flow during fluid injection is perpendicular to the X - Y plane. There are a total of 512 image slices in the Z direction. The image slab that we focused on consisted of 10 image slices (slices 460-469) with a depth of 63.5 μm . The image in Fig. 71 was taken after the core was first saturated with brine. The gray areas in Fig. 71 show voids that were saturated with brine. The areas in black are rock grains. The shaded gray areas in Fig. 71 show the change in pore shape/size as we move from the surface slice (slice 469) to the bottom slice (slice 460).

Fig. 72 shows the distribution of oil and water after oilflooding the core to residual water saturation (S_{wr}). In Fig. 72, oil is red, water is green, and the rock grains are black. Oil invaded most of the large pores while the residual water remained mostly in small pores and crevices. After oilflooding, we injected water until no more oil was produced (S_{or}). Fig. 73 shows that the residual oil occupied the center of the medium to large size pores while water formed a film around the residual oil. These observations are consistent with expectations in a strongly water-wet medium.

X = 4.6 mm, Y = 4.6 mm, Z = 3.25 mm
Number of Image Slices (Z-direction) = 512

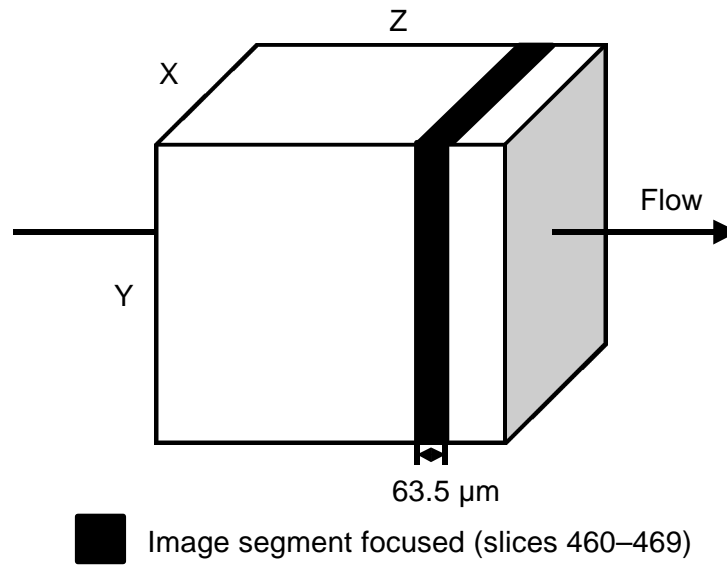


Fig. 70—Dimensions of image slab.

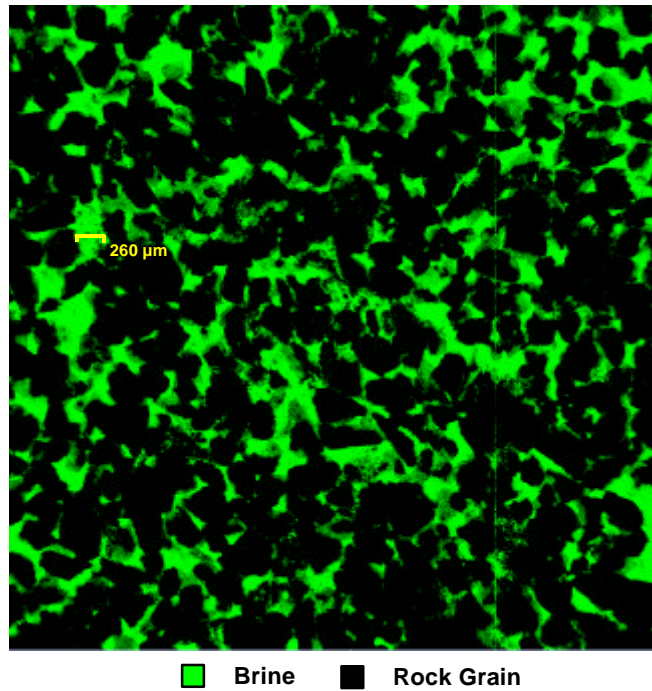


Fig. 71—X-Y plane view of image slab (slices 460-469) at $S_w=1.0$; image resolution=10 μm.

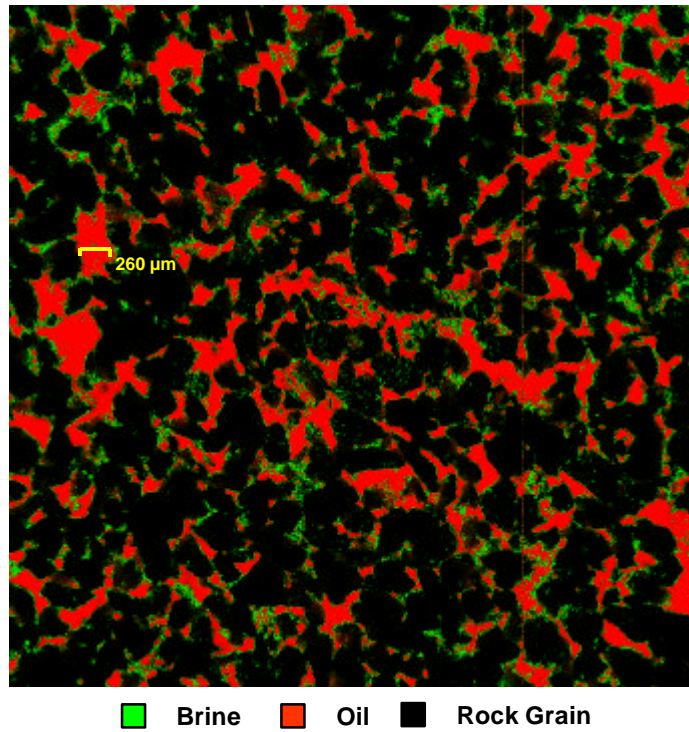


Fig. 72—X-Y plane view of image slab (slices 460-469) at S_{wr} ; image resolution=10 μm.

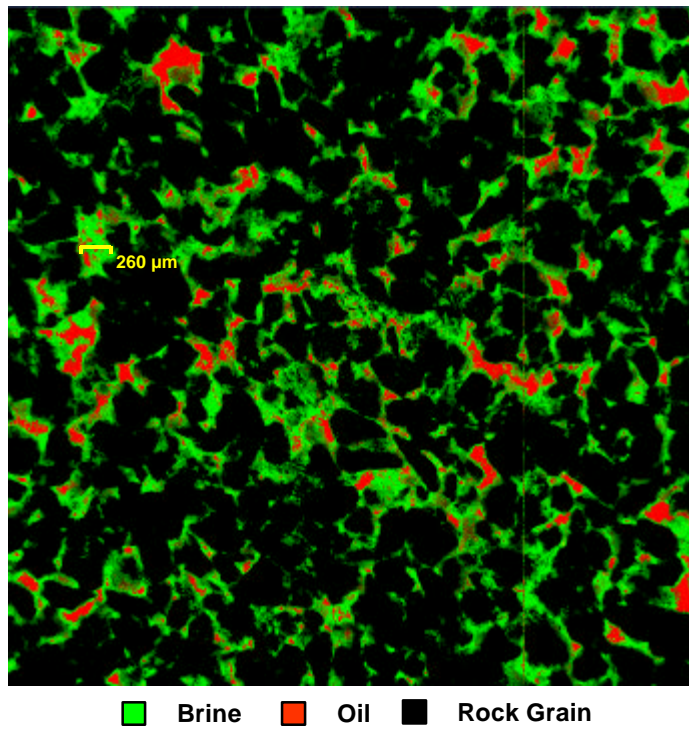


Fig. 73—X-Y plane view of image slab (slices 460-469) at S_{or} ; image resolution=10 μm.

Next, gelant was injected at residual oil saturation. Fig. 74 shows that some of the oil was displaced by the more viscous gelant during gelant injection. After gelant injection, we raised the temperature to around 60°C and shut the core in for 12 hours to allow gelation to occur. Immediately after shut-in, we injected oil to measure F_{rro} . Fig. 75 shows the distribution of oil and water after the F_{rro} measurement. Table 8 shows that the F_{rro} was 15. A comparison of Figs. 72 and 75 indicates that most of the pathways open to oil flow before gel placement remained accessible to oil after the gel treatment. This result suggests that the gel occupied only a small fraction of the pore space. Tracer results from a previous oil/water experiment in a high-permeability Berea core revealed that gel with a F_{rro} value of 20 occupied less than 5% of the pore space.

After the F_{rro} measurement, we injected brine to measure F_{rrw} . Table 8 shows that F_{rrw} was 1,220, which was significantly higher than the F_{rro} value of 15. Fig. 76 shows that water did not have access to most of the pathways opened to oil flow after treatment. A possible explanation is that gel particles strategically positioned at the entrance of the larger pores, changed the aspect ratio of the pores, and rendered the oil immobile during the subsequent water injection. During water injection after gel treatment, the trapped residual oil forced the water to flow around it as a thin film or through other small pores. This resulted in much more constricted pathways for water after gel placement. In contrast, the oil pathways were much less constricted during oil injection after gel treatment because oil could flow through the center of the larger pores. To test this concept, detailed image analyses will be performed to quantify the size distribution of the pores that constitute the oil pathways.

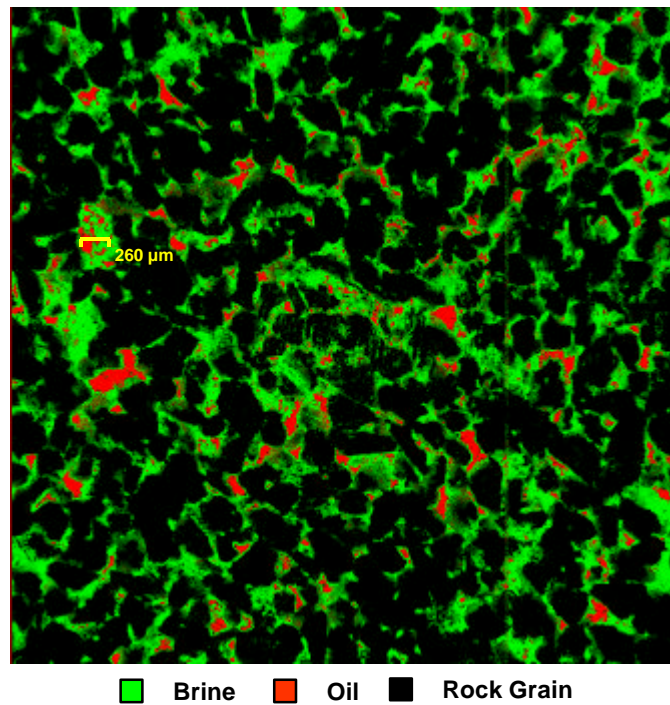


Fig. 74—X-Y plane view of image slab (slices 460-469) at S_{or} after gelant injection image resolution=10 μm.

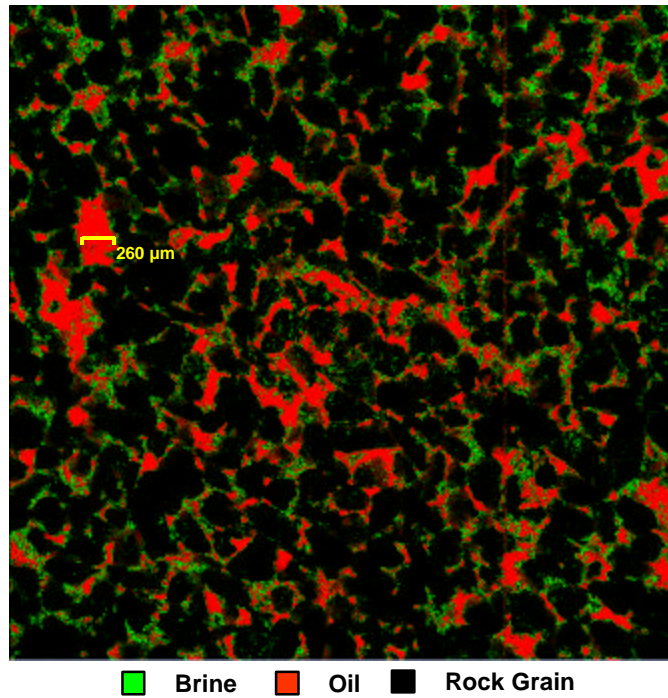


Fig. 75—X-Y plane view of image slab (slices 460-469) after F_{rro} measurement ($F_{rro} = 15$) image resolution= $10 \mu\text{m}$.

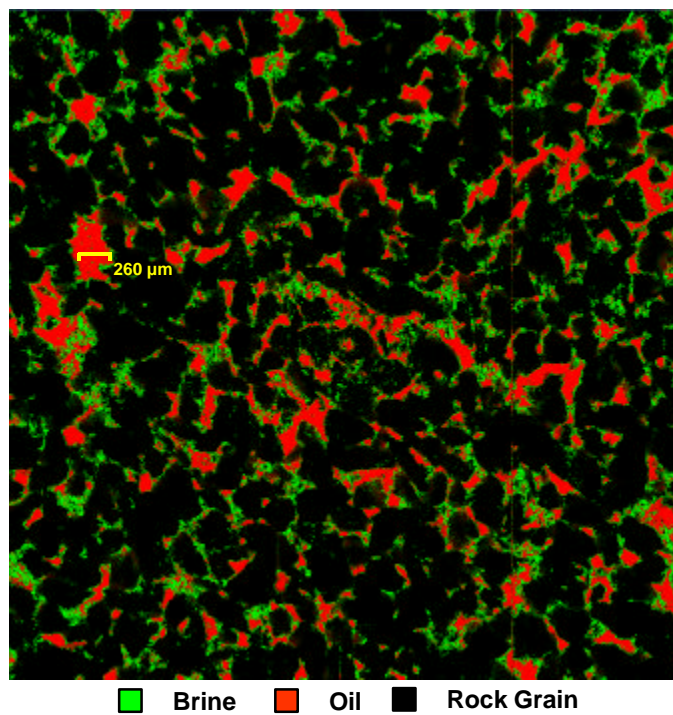


Fig. 76—X-Y plane view of image slab (slices 460-469) after F_{rrw} measurement ($F_{rrw} = 1,220$); image resolution= $10 \mu\text{m}$.

Imaging Experiments Using an Oil-Based Gel. In an earlier study, we observed a reversed disproportionate permeability reduction in water-wet Berea sandstone using an oil-based gel.²⁰ The gel reduced the permeability to oil more than that to water in Berea cores. We performed additional CMT imaging experiments using the oil-based gel in Berea sandstone to visualize this phenomenon on a microscopic scale. The objective is to compare the results with those from our first set of experiments using a water-based gel to improve our understanding of why the disproportionate permeability reduction occurs.

For the imaging experiments, we used a high-permeability Berea core as the porous medium. The core was similar to the one used in the previous imaging experiments with a water-based gel (Fig. 67). The core was 6.5 mm in diameter and 32.5 mm in length with an intermediate pressure tap 4 mm from the inlet face. Due to computer memory and time constraints, we focused our scan in a segment of the core that was 6.5 mm in diameter and 3.25 mm in length. To avoid end effects, the scanned segment was located about half way between the inlet and outlet face.

In the oil/water experiments, hexadecane was the oil phase. To increase the image contrast between the brine and the oil phases, hexadecane was doped with 10% w/w iodohexadecane. The gel contained 18% 12-hydroxysteric acid and hexadecane (doped with 10% w/w iodohexadecane). All experiments except gelant injection were performed at room temperature. To allow us to digitally compare the images before and after gel placement, oil, water, and gelant flooding were performed without ever removing the core from the sample stand. In total, we performed five 3-D scans with an image resolution of 10 μm at different stages of the oil-water experiment. During the imaging experiments, we first scanned the core when it was saturated only with brine. Next, the core was scanned at residual water saturation and residual oil saturation before gelant injection. During gelant injection, the core temperature was raised to $\sim 80^\circ\text{C}$. After gelant injection, the core was cooled to room temperature to allow the gel to form in situ. (The gelant was prepared at 80°C and the gel forms when the temperature drops below 65°C .) Then, water was injected into the core to measure the water residual resistance factor, F_{rrw} . The core was scanned again after water injection to visualize the water pathways after gel. Next, oil was injected to measure the oil residual resistance factor, F_{rro} . Finally the core was scanned after oil injection to visualize the oil pathways after gel. Table 9 shows that the gel reduced the permeability to oil 6.7 times more than that to water ($F_{rro}/F_{rrw}=6.7$).

Table 9—Summary of residual resistance factors: Oil-based gel
Core: strongly water-wet Berea
Gel: 18% w/w 12-hydroxysteric acid, hexadecane, 10% w/w iodohexadecane

k_w , mD	F_{rrw}	F_{rro}	F_{rro}/F_{rrw}
1,000	3	20	6.7

We are now processing and analyzing the data generated during the imaging experiments. We will report the results of our analysis when they become available.

Image analysis Using 3DMA Software

Image analyses are being performed using a software package called 3DMA. (Dr. Brent Lindquist of the Department of Applied Mathematics and Statistics of State University of New York at Stony Brook developed this software package.) This software package is capable of measuring distributions of pore size, pore-body/pore-throat aspect ratio, coordination number, channel length, and tortuosity of a porous rock using the three-dimensional images generated from our x-ray synchrotron experiments. In this section, we show some preliminary results from our image analyses using 3DMA.

Fig. 70 showed that our image block consisted of 512 slices. Due to a computer memory constraint, we divided the image block into eight sub-blocks of 64 slices each. The results shown in this section are from the first image sub-block consisting of slices 2 to 65. Fig. 77 shows the distributions of nodal pore volume and the corresponding effective pore radii. A nodal pore is a pore that is connected to at least two other pores. In other words, it is neither a dead-end pore nor is it an isolated pore. The effective radius of a nodal pore is determined from the measured pore volume assuming that the pore is a perfect sphere. In Figs. 77 and 78, an open circle with two attaching horizontal bars indicates the mean value and standard deviation, respectively. As shown in Fig. 77, the effective pore radii of the Berea sandstone in this image block range from less than 10 microns to 170 microns with a mean pore radius around 50 microns. Fig. 78 shows that the effective throat radii in the same image block range from around 5 microns to 80 microns with a mean throat radius of 18 microns. The relationship between effective pore radii and effective throat radii is illustrated in Fig. 79. From Fig. 79, we estimate that the average aspect ratio of the pore radius to throat radius is around 3. Currently, we are in the process of using this software to identify the pores occupied by oil before and after gel treatment. The objective is to examine the changes in distributions of pore size and aspect ratio of the pores occupied by oil before and after treatment.

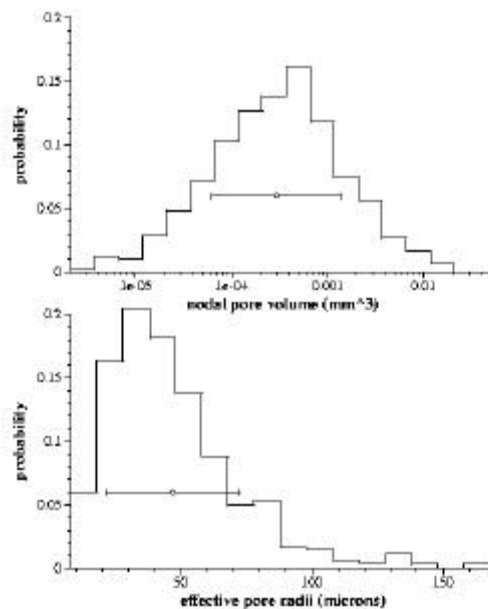


Fig. 77— Distributions of nodal pore volume and the corresponding effective pore radii.

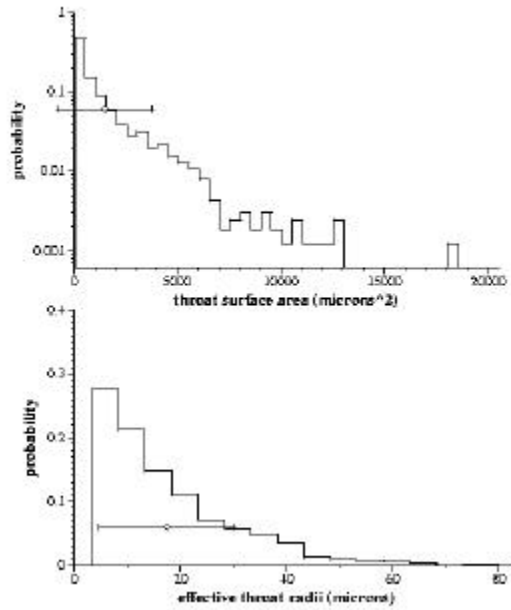


Fig. 78— Distributions of throat surface area and the corresponding effective throat radii.

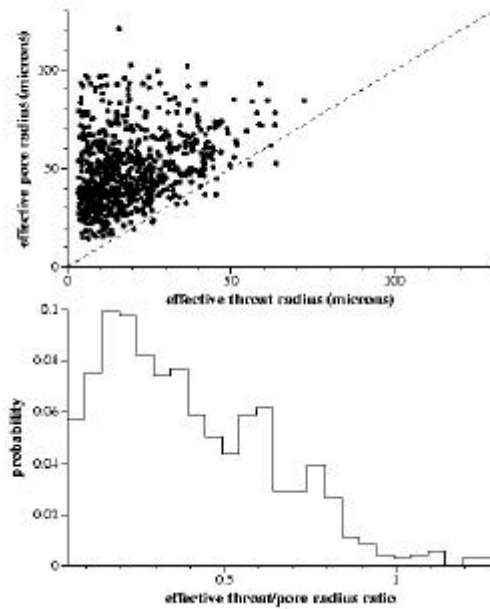


Fig. 79— Relationship between effective pore radii and effective throat radii.

In our future work, we plan to use a network model to simulate the disproportionate permeability reduction in porous rock. The 3DMA software package is also capable of providing the necessary input parameters for network modeling by direct measurements of the 3-D images generated from x-ray synchrotron imaging experiments. As an example, Fig. 80 shows a skeletonized image of the Berea sandstone. The image shown in Fig. 80 consists of 64 image

slices. In this image, the purple areas represent pore throats and the colored lines symbolize the backbones of connected pores that form continuous pathways in the porous rock. The pathways are color-coded in rainbow color scheme with red representing the smallest pores and blue representing the largest pores. The software package can also determine coordination numbers from the skeletonized image. (Please see Ref. 22 for a more detailed description of the software package.)

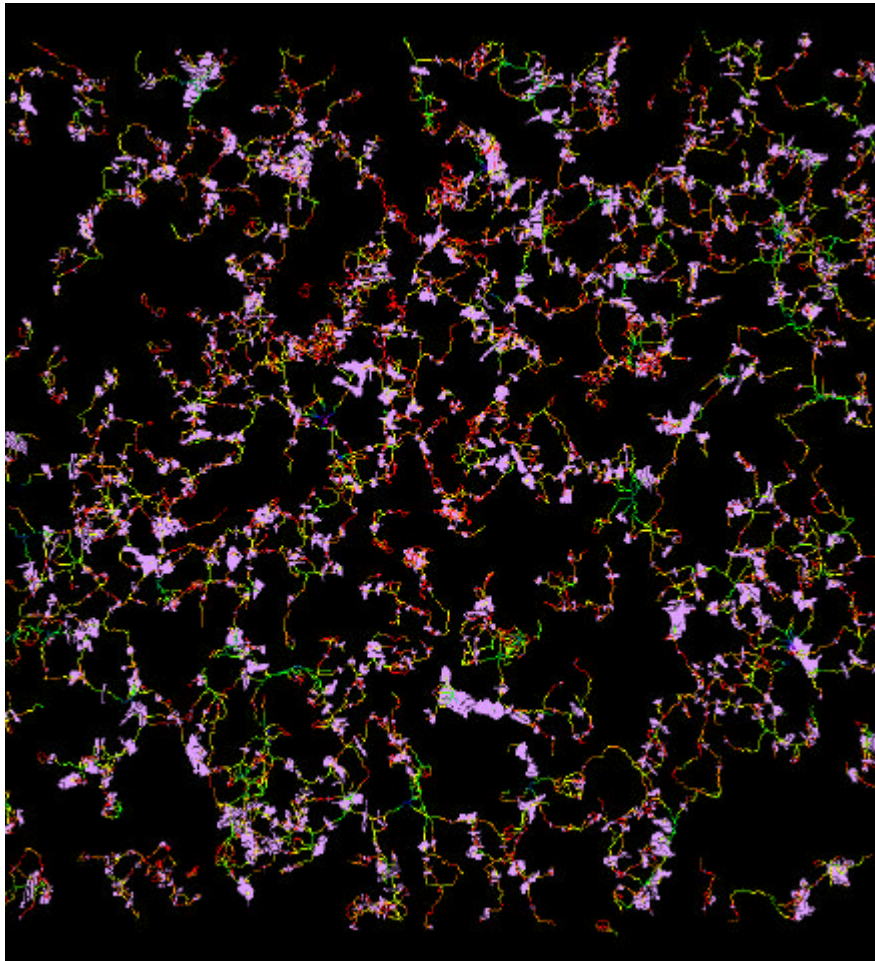


Fig. 80— Skeletonized image of the Berea sandstone (slices 2 to 65).

Modeling Disproportionate Permeability Reduction Using a Capillary-Bundle Model

Based on findings from the imaging experiments, we developed a simple mathematical model to try to quantify the disproportionate permeability reduction. (Dr. Ken Sorbie of Heriot-Watt University played an important role in this work.) For simplicity, we consider capillary tubes of different diameters to simulate the pores in porous rock. Also, we assume that the pores have a uniform size distribution, $f(r)$ (see Fig. 81). (These assumptions will be relaxed in the future as more data from our ongoing image analyses become available.)

Results from our imaging experiments show that the residual water occupies mostly small pores or crevices, while the residual oil resides mainly in medium to large size pores (Figs. 72 and 73). Based on these observations, Figs. 81 and 82 illustrate idealized distributions of fluids in pores (capillary tubes) of a uniform size distribution at residual water and oil saturations, respectively. As shown in Fig. 81, residual water occupies the smallest pores ($R_{MIN} < r < R_A$), where r is the pore radius. Fig. 82 shows that the residual oil occupies the medium to large size pores ($R_B < r < R_{MAX}$).

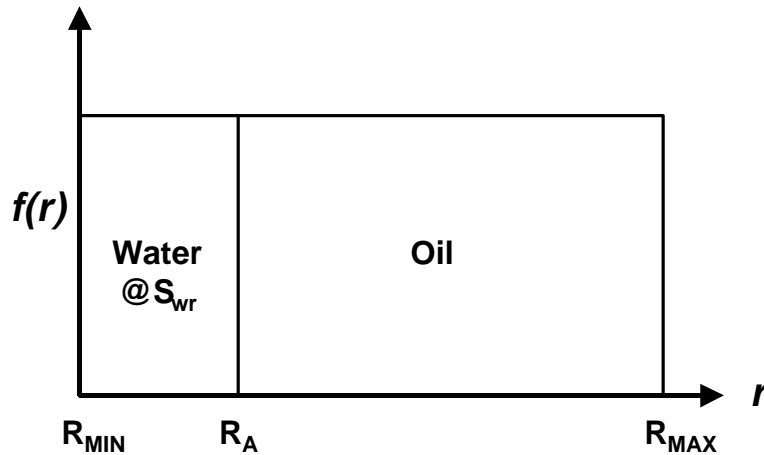


Fig. 81—Fluid distributions at S_{wr} in pores with a uniform size distribution.

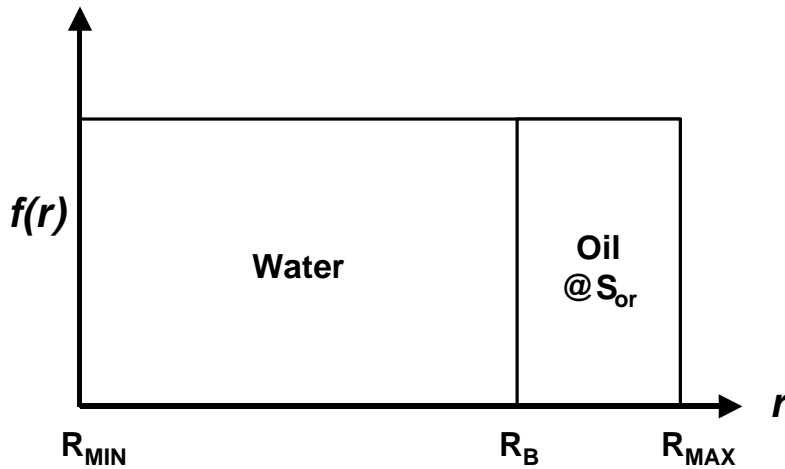


Fig. 82—Fluid distributions at S_{or} in pores with a uniform size distribution.

In this model, for a given pore, i , (or a capillary tube in this case) the flow rate is governed by the following equation:

$$q_i = g(r_i)\Delta p \dots\dots\dots(31)$$

where q is the flow rate, $g(r)$ is the conductivity function and Δp is the pressure drop.

Assume that

$$g(r) = r^I, \dots\dots\dots(32)$$

where I is an exponent (e.g., $I = 4$ for Poiseuille flow).

We now can calculate the endpoint water and oil relative permeabilities using the following equations:

$$k_{rw}^o = \frac{\int_{R_{MIN}}^{R_B} f(r)g(r)dr}{\int_{R_{MIN}}^{R_{MAX}} f(r)g(r)dr} \dots\dots\dots(33)$$

$$k_{ro}^o = \frac{\int_{R_A}^{R_{MAX}} f(r)g(r)dr}{\int_{R_{MIN}}^{R_{MAX}} f(r)g(r)dr} \dots\dots\dots(34)$$

where k_{rw}^o and k_{ro}^o are endpoint water and oil relative permeabilities, respectively. $f(r)$ is the probability density function for the pore size distribution, R_{MAX} and R_{MIN} are the size of the largest and the smallest pores in the porous rock, respectively. R_A is the size of the largest pore occupied by residual water and R_B is the size of the smallest pore size occupied by the residual oil (see Figs. 81 and 82).

During gelant injection, we assume that a water-based gelant invades all the pores accessible to water before treatment. Fig. 83 shows the idealized fluid distribution after gelant injection. In this model, we assume that the gelant does not invade the pores occupied by residual oil ($R_B < r < R_{MAX}$). Consequently, there is no permeability reduction associated with these pores after treatment. Again, this assumption can be relaxed later if necessary.

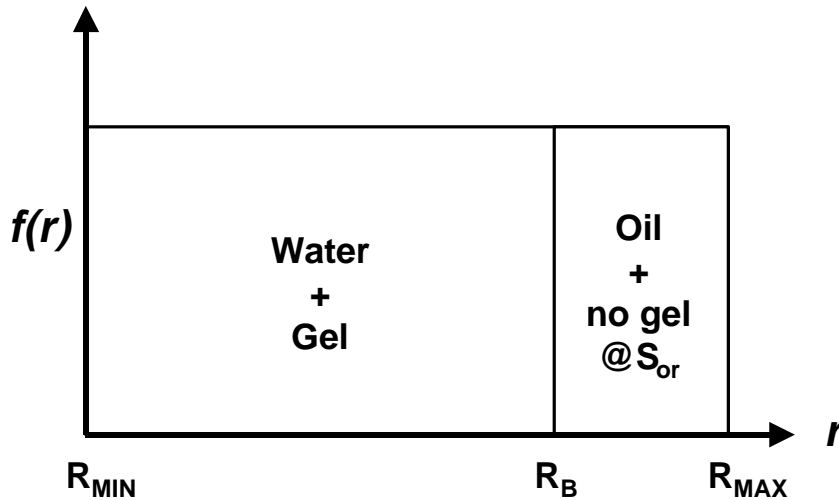


Fig. 83—Fluid distributions after gelant injection in pores with a uniform size distribution.

After gelation, we injected oil to measure the F_{rro} . Figs. 72 and 75 from the imaging experiments show that most of the pores opened to oil flow before treatment remained accessible to oil after treatment. Therefore, in addition to the pores containing residual oil, we assume in this model that oil also has access to gel-invaded pores with sizes between R_A and R_B (Fig. 84). These gel-invaded pores suffer a reduction in conductivity by a factor of \mathbf{a} after treatment. Based on these assumptions, we can calculate the endpoint oil relative permeability after treatment using the following equation:

$$\tilde{k}_{ro} = \frac{\int_{R_A}^{R_B} f(r)g\left(\frac{r}{\mathbf{a}}\right)dr + \int_{R_B}^{R_{MAX}} f(r)g(r)dr}{\int_{R_{MIN}}^{R_{MAX}} f(r)g(r)dr}, \dots\dots\dots(35)$$

where \tilde{k}_{ro} is the endpoint oil relative permeability after treatment and \mathbf{a} is the blocking factor.

After the F_{rro} measurements, we injected water to measure the degree of permeability reduction to water (F_{rrw}). Fig. 76 shows that water did not have access to most of the pores opened to oil flow after treatment. As shown in Fig. 85, we assume that during the F_{rrw} measurements, water has access to pores with sizes between R_{MIN} and R_A . Hence, the endpoint water relative permeability after treatment can be calculated using the following equation:

$$\tilde{k}_{rw} = \frac{\int_{R_{MIN}}^{R_A} f(r)g\left(\frac{r}{\mathbf{a}}\right)dr}{\int_{R_{MIN}}^{R_{MAX}} f(r)g(r)dr} \dots\dots\dots(36)$$

where \tilde{k}_{rw} is the endpoint water relative permeability after treatment.

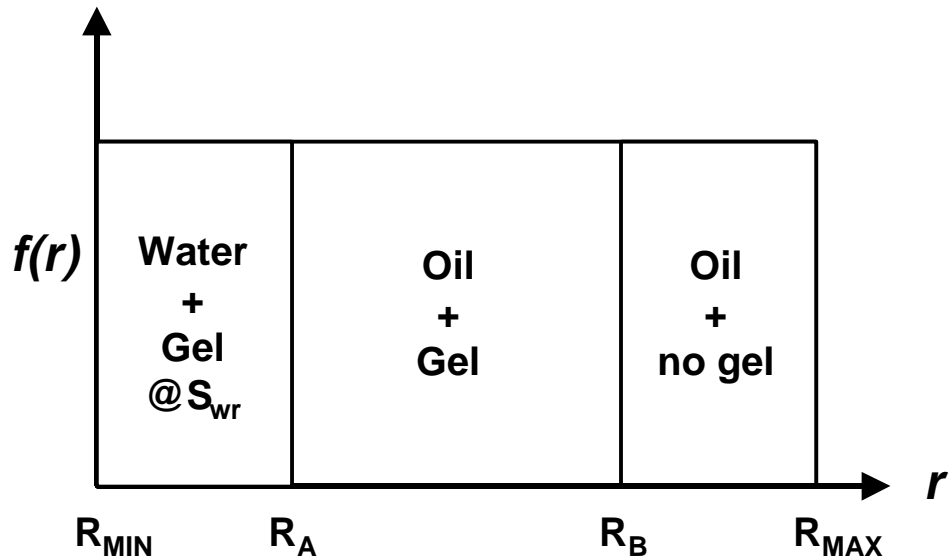


Fig. 84—Fluid distribution after F_{rro} measurements in pores of a uniform size distribution.

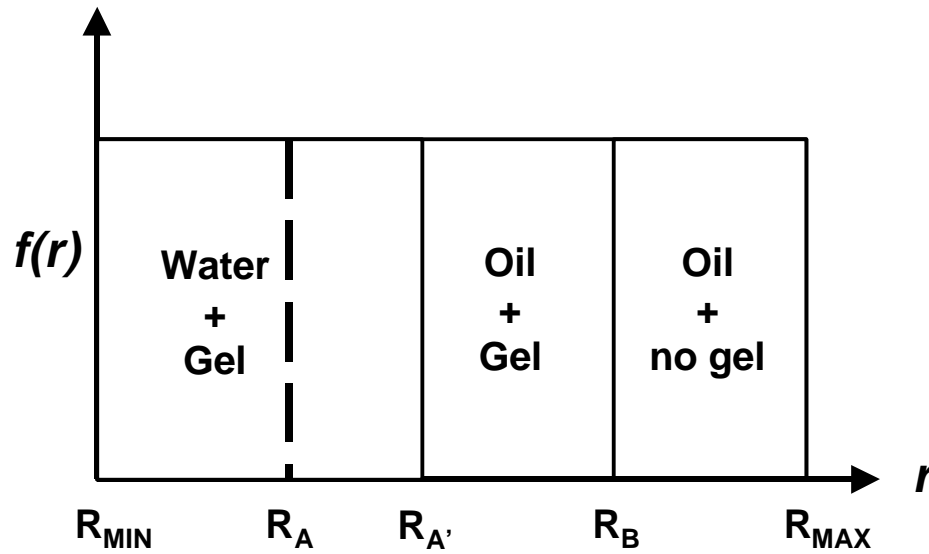


Fig. 85—Fluid distribution after F_{rrw} measurements in pores of a uniform size distribution.

In field applications, however, water is usually the first and only fluid contacting the gel in the treated region of the watered-out zones. Since we assume in this model that water has no access to the pores containing residual oil, water can only flow through the gel-invaded pores ($R_{MIN} < r < R_B$) after treatment (Fig. 83). Based on this assumption, we can use Eq. 37 to calculate the endpoint water relative permeability after treatment.

$$\tilde{k}_{rw}^o = \frac{\int_{R_{MIN}}^{R_B} f(r)g\left(\frac{r}{a}\right)dr}{\int_{R_{MIN}}^{R_{MAX}} f(r)g(r)dr} \dots\dots\dots(37)$$

Combining Eqs. 33 through 37, we can now calculate F_{rrw} and F_{rro} .

$$F_{rrw} = \frac{k_{rw}^o}{\tilde{k}_{rw}^o} \dots\dots\dots(38)$$

$$F_{rro} = \frac{k_{ro}^o}{\tilde{k}_{ro}^o} \dots\dots\dots(39)$$

Example Calculations. In this section, we use a simple example to demonstrate the ability and limitations of this model in predicting disproportionate permeability reduction. In this example, we assume that the reservoir contains two non-communicating layers. The water layer is completely watered-out with a residual oil saturation of 25% and the oil layer is producing no water and has a residual water saturation of 25%. Fig. 86 shows that the porous rock has a uniform pore size distribution with $R_{MIN} = 0$, $R_A = 10$, $R_B = 30$, and $R_{MAX} = 40$.

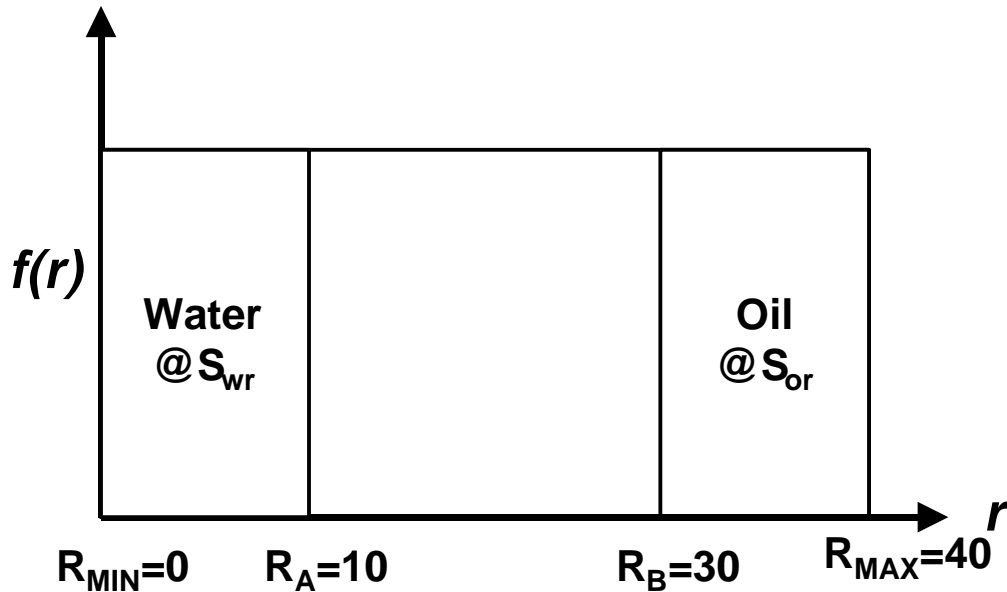


Fig. 86—Fluid distribution for example calculations.

For a uniform size distribution, the probability density function can be calculated by the following equation:

$$f(r) = \frac{1}{R_{MAX} - R_{MIN}} = \frac{1}{40 - 0} = \frac{1}{40}.$$

By assuming that $I = 2$. We can now calculate the endpoint water and oil relative permeabilities using Eqs. 33 and 34.

$$k_{rw}^o = \frac{\int_0^{30} \frac{1}{40} r^2 dr}{\int_0^{40} \frac{1}{40} r^2 dr} = \left(\frac{30}{40} \right)^{2+1} = 0.42$$

$$k_{ro}^o = \frac{\int_{10}^{40} \frac{1}{40} r^2 dr}{\int_0^{40} \frac{1}{40} r^2 dr} = \left(\frac{40^{2+1} - 10^{2+1}}{40^{2+1}} \right) = 0.984$$

For this example, we used a gel that can reduce the permeability to water by a factor of 26,400 ($F_{rrw} = 26,400$) and that to oil by a factor of 525 ($F_{rro} = 525$). Combining Eqs. 33 and 37 and rearranging, Eq. 38 becomes

$$F_{rrw} = \frac{k_{rw}^o}{k_{rw}} = \frac{\int_0^{R_B} f(r)g(r)dr}{\int_0^{R_B} f(r)g\left(\frac{r}{\mathbf{a}}\right)dr} = \mathbf{a}^{I+1} \dots\dots\dots(40)$$

Since we know that $F_{rrw} = 26,400$, we can use Eq. 40 to calculate the blocking factor, \mathbf{a} . Substituting $F_{rrw} = 26,400$ and $I = 2$ into Eq. 40,

$$\mathbf{a}^3 = 26,400 \Rightarrow \mathbf{a} = 29.8.$$

With the blocking factor \mathbf{a} calculated, we now test how well the model predicts F_{rro} . Combining Eqs. 34 and 35 and rearranging, Eq. 39 becomes

$$F_{rro} = \frac{\int_{R_A}^{R_{MAX}} f(r)g(r)dr}{\int_{R_A}^{R_B} f(r)g\left(\frac{r}{\mathbf{a}}\right)dr + \int_{R_B}^{R_{MAX}} f(r)g(r)dr} = \frac{R_{MAX}^{I+1} - R_A^{I+1}}{\left[\left(\frac{R_B}{\mathbf{a}}\right)^{I+1} - \left(\frac{R_A}{\mathbf{a}}\right)^{I+1}\right] + [R_{MAX}^{I+1} - R_B^{I+1}]} \dots\dots\dots(41)$$

From Eq. 41, we can calculate F_{rro} .

$$F_{rro} = \frac{40^{2+1} - 10^{2+1}}{\left[\left(\frac{30}{29.8}\right)^{2+1} - \left(\frac{10}{29.8}\right)^{2+1}\right] + [40^{2+1} - 30^{2+1}]} \approx 2 \dots\dots\dots(42)$$

Instead of an F_{rro} value of 525, the model predicts an F_{rro} value of 2. Obviously, with the current assumptions, this model greatly underestimated the effect of gel on the permeability to oil after treatment. Remember, we assumed in this model that the large pores occupied by residual oil are free of gel after treatment. A careful examination of Eq. 42 reveals that the contribution of the gel-blocked pores ($R_A < r < R_B$) to the permeability reduction to oil after treatment is negligible because of the overwhelming contribution from the large gel-free pores ($R_B < r < R_{MAX}$) to the permeability to oil after treatment. Also, we assume that the blocking factor, \mathbf{a} , is the same for large and small pores. Our previous study²¹ showed that a gel reduced the permeability to both oil and water more in low-permeability cores than in high-permeability cores. The assumption of uniform pore size distribution and using capillary bundles to represent the real pores also contributed to the overestimation of the permeability to oil after treatment. However, as a first approximation, the simplified model did qualitatively predict the disproportionate permeability reduction. Currently, we are using software tools to analyze the 3-D images from our imaging experiments to calculate the pore size distribution of the porous rock and the fluid distributions at different stages of the experiment. When we finish the image analyses, we will use the data to improve the model.

Summary

1. Imaging experiments are in progress using high-resolution computed microtomography (CMT) at Brookhaven National Laboratory to understand why gels reduce permeability to water more than that to oil. The method provides outstanding resolution of rock, water, and oil on a micrometer scale. In water-wet Berea sandstone, the water film around trapped residual oil drops was clearly visible. In our first set of experiments, CMT results indicated that gels increased the residual oil saturation in larger pores during water injection, thus decreasing permeability to water much more than that to oil.
2. In our second set of experiments, we used CMT to visualize why an oil-based gel reduced the permeability to oil more than that to water. The objective is to compare the results with those from our first set of experiments using a water-based gel to improve our understanding of why the disproportionate permeability reduction occurs. We are now analyzing the data generated during the imaging experiments.
3. Image analyses are being performed using a software package called 3DMA. This software package is capable of measuring distributions of pore size, pore-body/pore-throat aspect ratio, coordination number, channel length, and tortuosity of a porous rock using the three-dimensional images generated from our x-ray synchrotron experiments. In this report, we show some preliminary results from our image analyses using 3DMA.
4. Based on the results from our imaging experiments, we developed a simple capillary-bundle model to predict disproportionate permeability reduction. Using a simple example, we demonstrated that the model could qualitatively predict the disproportionate permeability reduction. However, due to the simplified assumptions made in developing the model, more work is needed using data from our image analyses to improve this model.

NOMENCLATURE

- a_c = fractional area associated with concentrated gel
 a_f = fractional area associated with fresh gel
 C = produced concentration, g/m³
 C_o = injected concentration, g/m³
 c_a = constant in Eq. 20, d/ft [s/cm]
 c_b = constant in Eq. 23, darcys/in.² [[$\mu\text{m}^2/\text{cm}^2$]
 c_c = constant in Eq. 8
 F_r = resistance factor
 F_{rro} = oil residual resistance factor
 F_{rrw} = water residual resistance factor
 $f(r)$ = fraction of pores with radius, r
 G' = elastic modulus, psi [Pa]
 $g(r)$ = conductivity function
 h = height, ft [m]
 h_f = fracture height, ft [m]
 k = permeability, darcys [μm^2]
 k_f = fracture permeability, darcys [μm^2]
 k_{gel} = gel permeability to water, darcys [μm^2]
 k_{ro}^o = endpoint relative permeability to oil before gel placement, darcys [μm^2]
 $k_{ro}^{\sim o}$ = endpoint relative permeability to oil after gel placement, darcys [μm^2]
 k_{rw}^o = endpoint relative permeability to water before gel placement, darcys [μm^2]
 $k_{rw}^{\sim o}$ = endpoint relative permeability to water after gel placement, darcys [μm^2]
 k_w = permeability to water, darcys [μm^2]
 L = distance along a fracture, ft [m]
 L_1 = distance of gel penetration at time 1, ft [m]
 L_2 = distance of gel penetration at time 2, ft [m]
 L_f = fracture length, ft [m]
 n = exponent in Eq. 20
 $\mathbf{D}p$ = pressure drop, psi [Pa]
 dp/dl = pressure gradient, psi/ft [Pa/m]
 q = total injection or production rate, BPD [m³/d]
 q_i = flow rate in tube i , BPD [m³/d]
 q_t = total injection rate, BPD [m³/d]
 R_A = minimum pore radius for pores occupied by oil at S_{wr} before gel placement, ft [μm]
 $R_{A'}$ = minimum pore radius for pores occupied by oil at S_{wr} after gel placement, ft [μm]
 R_B = minimum pore radius for pores occupied by oil at S_{or} , ft [μm]
 R_{MAX} = maximum pore radius, ft [μm]
 R_{MIN} = minimum pore radius, ft [μm]
 r = pore radius, ft [μm]
 r_1 = radius of gel front at time 1, ft [m]
 r_2 = radius of gel front at time 2, ft [m]
 r_e = external drainage radius, ft [m]

r_i = radius of tube i , ft [μm]
 r_w = wellbore drainage radius, ft [m]
 S_{or} = residual oil saturation
 S_w = water saturation
 S_{wr} = residual water saturation
 u = leakoff rate, ft/d [cm/s]
 u_c = water leakoff rate associated with concentrated gel, ft/d [cm/s]
 u_f = water leakoff rate associated with fresh gel, ft/d [cm/s]
 u_i = local water leakoff rate, ft/d [cm/s]
 u_l = water leakoff rate, ft/d [cm/s]
 t = time, s
 V_1 = volume injected at time 1, bbl [m^3]
 V_2 = volume injected at time 2, bbl [m^3]
 w_f = fracture width, in. [m]
 X = distance in X -direction, in. [m]
 Y = distance in Y -direction, in. [m]
 Z = distance in Z -direction, in. [m]
 \mathbf{a} = conductivity reduction factor in Eq. 35
 \mathbf{l} = exponent in Eq. 32
 \mathbf{m} = viscosity, cp [mPa-s]
 \mathbf{m}_w = water viscosity, cp [mPa-s]
 \mathbf{t}_y = yield stress, psi [Pa]

REFERENCES

1. Seright, R.S.: "Using Chemicals to Optimize Conformance Control in Fractured Reservoirs," Annual Technical Progress Report (U.S. DOE Report DOE/BC/15110-2), U.S. DOE Contract DE-AC26-98BC15110, (Sept. 1999) 3-52.
2. Seright, R.S. and Liang, J.: "A Survey of Field Applications of Gel Treatments for Water Shutoff," paper SPE 26991 presented at the 1994 SPE III Latin American & Caribbean Petroleum Engineering Conference, Buenos Aires, Argentina, April 27-29.
3. Sydansk, R.D. and Moore, P.E.: "Gel Conformance Treatments Increase Oil Production in Wyoming," *Oil & Gas J.* (Jan. 20, 1992) 40-45.
4. Borling, D.C.: "Injection Conformance Control Case Histories Using Gels at the Wertz Field CO₂ Tertiary Flood in Wyoming, USA," paper SPE 27825 presented at the 1994 SPE/DOE Symposium on Improved Oil Recovery, Tulsa, April 17-20.
5. Hild, G.P. and Wackowski, R.K.: "Reservoir Polymer Gel Treatments To Improve Miscible CO₂ Flood," *SPEE* (April. 1999) 196-204.
6. Lane, R.H. and Sanders, G.S.: "Water Shutoff Through Fullbore Placement of Polymer Gel in Faulted and in Hydraulically Fractured Producers of the Prudhoe Bay Field," paper SPE 29475 presented at the 1995 SPE Production Operations Symposium, Oklahoma City, April 2-4.
7. Seright, R.S.: "Gel Placement in Fractured Systems," *SPEPF* (Nov. 1995), 241-248.
8. Seright, R.S.: "Use of Preformed Gels for Conformance Control in Fractured Systems," *SPEPF* (Feb. 1997) 59-65.
9. Seright, R.S.: "Polymer Gel Dehydration During Extrusion Through Fractures," *SPEPF* (May 1999) 110-116.
10. Seright, R.S.: "Mechanism for Gel Propagation Through Fractures," paper SPE 55628 presented at the 1999 SPE Rocky Mountain Regional Meeting, Gillette, May 15-19.
11. Seright, R.S.: "Improved Methods for Water Shutoff," Final Technical Progress Report (U.S. DOE Report DOE/PC/91008-14), U.S. DOE Contract DE-AC22-94PC91008, BDM-Oklahoma Subcontract G4S60330 (Oct. 1998) 21-54.
12. Seright, R.S.: "Gel Propagation Through Fractures," paper SPE/DOE 59316 presented at the 2000 SPE/DOE Symposium on Improved Oil Recovery, Tulsa, April 2-5.
13. Howard, G.C. and Fast, C.R.: *Hydraulic Fracturing*, SPE Monograph Series, **2**, Society of Petroleum Engineers, Dallas (1970) 33.
14. Liu, Jin, and Seright, R.S.: "Rheology of Gels Used For Conformance Control in Fractures," paper SPE 59318 presented at the 2000 SPE/DOE Improved Oil Recovery Symposium, Tulsa, April 3-5.
15. Seright, R.S. and Lee, R.L.: "Gel Treatments for Reducing Channeling Through Naturally Fractured Reservoirs," *SPEPF* (Nov. 1999) 269-276.
16. Lane, R.H., and Seright, R.S.: "Gel Water Shutoff in Fractured or Faulted Horizontal Wells," paper CIM/SPE 65527 presented at the 2000 SPE/Petroleum Society of CIM International Conference on Horizontal Well Technology held in Calgary, Alberta, Canada, Nov. 6-8.
17. O'Brien, W.J., Stratton, J.J., and Lane, R.H.: "Mechanistic Reservoir Modeling Improves Fissure Treatment Gel Design in Horizontal Injectors, Idd El Shargi North Dome Field, Qatar", Paper SPE 56743 presented at the 1999 SPE Annual Technical Conference and Exhibition, Houston, Oct. 5 – 8.

18. Seright, R.S.: "Improved Techniques for Fluid Diversion In Oil Recovery," final report, DOE/BC/14880-15, U.S. DOE (Jan. 1996) 97-108.
19. Coles, M.E., Hazlett, R.D., Muegge, E.L., Jones, K.W., Andrews, B., Dowd, B., Siddons, P., Peskin, A., Spanne, P., and Soll, W.E.: "Developments in Synchrotron X-Ray Microtomography with Applications to Flow in Porous Media," paper SPE 36531 presented at the 1998 Annual Technical Conference and Exhibition, Denver, Oct. 6-9.
20. Seright, R.S.: "Improved Methods for Water Shutoff," Final Technical Progress Report (U.S. DOE Report DOE/PC/91008-14), U.S. DOE Contract DE-AC22-94PC91008, BDM-Oklahoma Subcontract G4S60330 (Oct. 1998) 59-59.
21. Liang, J. and Seright, R.S.: "Further Investigations of Why Gels Reduce k_w More Than k_o ," *SPEPF* (Nov. 1997).
22. Lindquist, W.B. and Venkatarangan, A.: "Investigating 3D Geometry of Porous Media From High Resolution Images," *Phys. Chem. Earth*, Part A, 25, 1999, 593-599.

APPENDIX A: Technology Transfer

Presentations

On September 21, 2000, we presented the talk, “Mechanism For Gel Propagation Through Fractures,” at the 2000 International Energy Agency Meeting in Edinburgh, Scotland.

On June 27, 2000, we presented the talk, “Using Chemicals to Optimize Conformance in Fractured Reservoirs,” at the 2000 DOE Petroleum Technology Contract Review Meeting in Denver, Colorado.

On April 25, 2000, we presented the talk, “Conformance Issues Relating to Produced Water Re-injection in Layered Reservoirs,” at Marathon Oil in Littleton, Colorado.

On April 5, 2000, we presented the talk, “Wall-Effect/Gel-Droplet Model of Disproportionate Permeability Reduction,” at the 2000 SPE/DOE Improved Oil Recovery Symposium in Tulsa, OK.

On April 4, 2000, we presented the talk, “Gel Propagation Through Fractures,” at the 2000 SPE/DOE Improved Oil Recovery Symposium in Tulsa, OK.

On April 4, 2000, we presented the talk, “Rheology of Gels Used For Conformance Control,” at the 2000 SPE/DOE Improved Oil Recovery Symposium in Tulsa, OK.

On April 2, 2000, we presented the Short Course, “Water Shutoff,” at the 2000 SPE/DOE Improved Oil Recovery Symposium in Tulsa, OK.

On March 30, 2000, we held a project review in Socorro, NM. Nine people attended the review, representing 6 different organizations (not including New Mexico Tech personnel).

From November 16-20, 1999, we presented talks on “Improved Methods for Water Shutoff,” at the Chinese Petroleum Corporation in Maioli, Taiwan.

On September 23, 1999, we presented the talk, “Disproportionate Permeability Reduction by Gels,” at the 1999 IEA Meeting in Paris, France.

On September 13, 1999, we presented the talk, “Gel Propagation Through Fractures,” at Marathon Oil in Littleton, Colorado.

On July 27 and 28, 1999, we held a project review in Socorro, NM. Thirteen people attended the review (not including New Mexico Tech personnel) representing 9 different organizations.

On June 29, 1999, we presented the talk, “Sizing Gelant Treatments in Hydraulically Fractured Production Wells,” at the 1999 DOE Oil and Gas Conference in Dallas, Texas.

On May 17, 1999, we presented SPE paper 55628, “Mechanism for Gel Propagation Through Fractures,” at the 1999 Rocky Mountain Regional Meeting in Gillette, WY.

On April 23, 1999, we presented the talk, “Gel Dehydration During Extrusion Through Fractures,” at Saga Petroleum in Stavanger, Norway.

On April 22, 1999, we presented the talk, “Gel Dehydration During Extrusion Through Fractures,” at Stavanger College in Stavanger, Norway.

On April 22, 1999, we presented the talk, “A Strategy for Attacking Excess Water Production Problems,” at Elf Norge in Stavanger, Norway.

On March 11, 1999, we presented the talk, “A Strategy for Attacking Excess Water Production Problems,” for the Midcontinent SPE Section in Tulsa, OK.

From November 16-20, 1998, we presented talks on “Improved Methods for Water Shutoff,” at the Chinese Petroleum Corporation in Maioli, Taiwan.

On October 6 and 7, 1998, we held a project review in Socorro, NM. Twenty-six people attended the review (not including New Mexico Tech personnel) representing 17 different organizations.

Internet Postings on the Project and Software to Download

A description of our research group can be found at the following New Mexico PRRC web site: <http://baervan.nmt.edu/randy>. This site was recently updated and expanded significantly.

This web site also allows downloading of software, Version 1.07 of “Gel Design,” for sizing gelant treatments in hydraulically fractured production wells.

Papers and Publications

Lane, R.H., and Seright, R.S.: “Gel Water Shutoff in Fractured or Faulted Horizontal Wells,” paper CIM/SPE 65527 presented at the 2000 SPE/Petroleum Society of CIM International Conference on Horizontal Well Technology held in Calgary, Alberta, Canada, Nov. 6-8.

Seright, R.S.: “Mechanism For Gel Propagation Through Fractures,” presented at the 2000 International Energy Agency Meeting in Edinburgh, Scotland, Sept. 20-22.

Liang, J., and Seright, R.S.: “Wall-Effect/Gel Droplet Model of Disproportionate Permeability Reduction,” paper SPE 59344 presented at the 2000 SPE/DOE Improved Oil Recovery Symposium, Tulsa, OK, April 3-5.

Liu, Jin, and Seright, R.S.: “Rheology of Gels Used For Conformance Control in Fractures,” paper SPE 59318 presented at the 2000 SPE/DOE Improved Oil Recovery Symposium, Tulsa, OK, April 3-5.

Seright, R.S.: "Gel Propagation Through Fractures," paper SPE 59316 presented at the 2000 SPE/DOE Improved Oil Recovery Symposium, Tulsa, OK, April 3-5.

Seright, R.S. and Lee, Robert: "Gel Treatments for Reducing Channeling Through Naturally Fractured Reservoirs," *SPE Production & Facilities* (Nov. 1999) 269-276.

Seright, R.S.: "Using Chemicals to Optimize Conformance Control in Fractured Reservoirs," Annual Technical Progress Report (U.S. DOE Report DOE/BC/15110-2), U.S. DOE Contract DE-AC26-98BC15110 (Sept. 1999).

Seright, R.S.: "Mechanism for Gel Propagation Through Fractures," paper SPE 55628 presented at the 1999 Rocky Mountain Regional Meeting, Gillette, WY, May 15-18.

Seright, R.S.: "Polymer Gel Dehydration During Extrusion Through Fractures," *SPE Production & Facilities* (May 1999) 110-116.

Seright, R.S., Liang, J., and Seldal, M.: "Sizing Gelant Treatments in Hydraulically Fractured Production Wells," *SPE Production & Facilities* (Nov. 1998) 223-229.

Seright, R.S.: "Improved Methods for Water Shutoff," Final Technical Progress Report (U.S. DOE Report DOE/PC/91008-14), U.S. DOE Contract DE-AC22-94PC91008, BDM-Oklahoma Subcontract G4S60330 (Oct. 1998).